POLITECNICO
DI TORINO

UNIVERSITÁ
DEGLI STUDI
DI TORINO

Doctoral Dissertation
Doctoral Program in Pure and Applied Mathematics (37th cycle)

Mathematical, Algorithmic and Numerical Solutions to enhance Electrostatic Calculations for Biomolecules in Electrolytic Solutions

Author:
Vincenzo Di Florio

Supervisor:
Prof. Lamberto Rondoni
Dr. Walter Rocchia

Politecnico di Torino - Università di Torino - Istituto Italiano di Tecnologia

June 15, 2025

Declaration of Authorship

I hereby declare that, the contents and organization of this dissertation constitute my own original work and does not compromise in any way the rights of third parties, including those relating to the security of personal data.

Vincenzo DI FLORIO
June 15, 2025

Alla mia famiglia
e a chi mi è stato sempre vicino

Acknowledgements

Abstract

This PhD thesis is divided into two main Parts, corresponding to the two primary research projects undertaken: the study of electrostatic in biomolecules within electrolytic solutions, and the investigation of state relations in oscillator chains. Although these topics may initially appear unrelated, they share a common objective: understanding the behavior of complex systems through the frameworks of mechanics and thermodynamics, supported by rigorous mathematical formulations. In both cases, we aim to construct models that faithfully represent physical phenomena, particularly in situations where standard analytical or numerical techniques may lead to inaccurate results if the fundamental physical and thermodynamic principles are not properly enforced.

The first Part focuses on modeling electrostatic interactions of biomolecules in electrolytic solvents using continuum electrostatic models. We derive the Poisson-Boltzmann equation (PBE), along with its linearized and generalized forms. The PBE is a widely used partial differential equation in biophysics for estimating the electrostatic energy of biomolecular systems in electrolyte solutions. We analyze the linearized PBE, offering new analytical insights and proposing a numerical method to solve it efficiently. This method is implemented in the software package `NextGenPB`. The solver is validated through comparisons with analytical benchmarks and existing computational tools. We further demonstrate its applicability to large-scale biomolecular systems, underscoring its potential for practical applications.

The second Part investigates a previously identified linear relation that connects the average distance between pairs of consecutive particles with their kinetic energy to quite a large set of one-dimensional particle systems known to produce anomalous transport. This relation is microscopic in nature, since the quantities involved are neither averaged over many particles, neither over very large times. Nevertheless, its robustness under variations of the external parameters, and the limited set of quantities it involves qualify it as a state equation, analogously to thermodynamic relations. We provide conditions for which the relation can be violated within a limited range of parameters values, and we find that it can be extended to two dimensional networks of coupled oscillators. The validity of this relation further shows that the states of aggregation of matter in low dimensional systems are often different from standard macroscopic ones.

Contents

Declaration of Authorship iii

Acknowledgements vii

Abstract ix

List of Abbreviations xv

List of Symbols xvii

I Main Part: Electrostatics in Electrolytic Solutions 1

1 Introduction 5

2 Electrostatics in Biomolecular Systems 9
- 2.1 Elementary Electrostatic Interactions 10
- 2.2 The Solvent: Electrolyte Solutions 11
- 2.3 Electrostatic Interactions in Electrolyte Solutions 13
  - 2.3.1 Ion-Ion Interactions 14
  - 2.3.2 Ion-Solvent Interactions 14
  - 2.3.3 Solvent-Solvent Intractions 15
- 2.4 Molecular Volume 16
- 2.5 The Poisson-Boltzmann Model 20
  - 2.5.1 Assumptions underlying the Debye-Hückel Theory 20
  - 2.5.2 Poisson-Boltzmann Equation 22
- 2.6 Thermodynamic Approach: Generalized PBE 26
  - 2.6.1 PBE 33
  - 2.6.2 Size of Ions: Steric Effects 34
  - 2.6.3 Incorporating Ion-Solvation Effects 36

3 Analytical Results for LPBE 39
- 3.1 Total free energy for LPBE 40
- 3.2 Electrostatic Potential via Green's Identities 42
  - 3.2.1 Internal Electrostatic Potential via Green's Identities 42
  - 3.2.2 Partitioning of Internal Electrostatic Potential 46

Coulombic Potential 47
Polarization Potential 47
Ionic Potential: from volume to surface formulation 48
3.2.3 External Electrostatic Potential via Green's Identities 50
3.3 Analytical solutions for LPBE 51
3.3.1 Single Sphere-Kirkwood Model 51
3.3.2 Multi Non-Overlapping Spheres 53
3.4 Boundary conditions 58

4 Numerical Model 61
4.1 Primal–Mixed Finite Elements Discretization of the LPBE 62
4.2 FE Spaces W_h and U_h 65
4.2.1 FE space for scalar functions: W_h 66
4.2.2 FE space for vector functions: U_h 67
4.3 Matrix Formulation 70
4.3.1 Element Matrices 70
4.3.2 Static Condensation 71
4.4 Coefficient Discontinuity: equation discretization across the molecular surface 73
4.4.1 1D Numerical Approach 73
4.4.2 Physics-Based Approach 76
4.5 Weigted Harmonic Average in Primal Mixed FEM 78
4.5.1 Standard FE with WHA of the permittivity 80
4.6 Treatment of Point Sources 81
4.7 Electrostatic energy calculation 83
4.7.1 The polarization contribution 84
4.7.2 Ionic direct contribution calculation 86
4.8 Exploiting de-refinement for more efficient BCs 86
4.9 Software Architecture 88

5 Numerical Results 91
5.1 Accuracy: Analytically Solvable Systems 91
5.1.1 The Kirkwood Sphere 92
5.1.2 Non-Overlapping Spheres 95
5.1.3 Assessment of Boundary Conditions 96
5.2 Real Biomolecular Systems 98
5.2.1 Binding Energy Calculation 99
5.2.2 Application to Large Systems 102

6 Conclusions 111

II Additional work:
Microscopic state equation for oscillator chains 115

7 Microscopic state equation for oscillator chains 119
7.1 Introduction 119
7.2 Models and the microscopic relation 120
7.3 Effect of interaction potentials 124
  7.3.1 Harmonic and harmonic plus hard core 124
  7.3.2 SPC potential 126
  7.3.3 LJ potential 126
7.4 β-FPUT oscillators 128
  7.4.1 Effects of symmetry of potentials 132
  7.4.2 Stochastic baths 136
7.5 2-dimensional lattice 136
7.6 Concluding remarks 138

List of Abbreviations

PART I

BCs	**B**oundary **C**onditions
D-H	**D**ebye-**H**ückel
FEM	**F**inite **E**lement **M**ethod
LPBE	**L**inearized **P**oisson-**B**oltzmann **E**quation
MD	**M**olecular **D**ynamics
MS	**M**olecular **S**urface
PBE	**P**oisson-**B**oltzmann **E**quation
PMFEM	**P**rimal **M**ixed **F**inite **E**lement **M**ethod
QM	**Q**uantum **M**echanic
SAS	**S**olvent **A**ccessible **S**urface
SES	**S**olvent **E**xcluded **S**urface
VdWS	**V**an **d**er **W**aals **S**urface
WHA	**W**eighted **H**armonic **A**verage
WHA-PMFEM	**W**eighted **H**armonic **A**verage **P**rimal **M**ixed **F**inite **E**lement **M**ethod

PART II

FPUT	**F**ermi-**P**asta-**U**lam-**T**singou
LJ	**L**ennard-**J**ones
SPC	**S**oft-**P**oint-**C**hain

List of Symbols

PART I

Physical Symbols

ε_0	Vacuum permittivity
$\varepsilon_{r,m}$	Relative permittivity of the molecule
$\varepsilon_{r,s}$	Relative permittivity of the solvent
ε_m	Permittivity of the molecule
ε_s	Permittivity of the solvent
k_B	Boltzamann constant
T	Absolute temperature
e	Elementary charge
z_j	valence of the j-th ion species
n_j^b	Bulk concentration of the j-th ion species
ϕ	Electrostatic potential
$\mathbf{D}$	Dielectric field displacement
$\mathbf{E}$	Electrostatic field
Ω	Total volume
$\partial\Omega$	Border of the total volume
Ω_s	Solvent volume
Ω_m	Molecular volume
Γ	Molecular surface
ρ	Total free charge density
ρ^f	Fixed charge density
ρ^m	Ionic charge density
N	Number of fixed charge
n_j	Concentration of the j-th ion species
μ_j	Total chemical potential of the j-th ion species
μ_j^{ent}	Chemical potential of the j-th ion species for non-electrostatic contributions
μ_j^e	Chemical potential of the j-th ion species for electrostatic contributions
a_j	Effective volume of the j-th ion species
k_D	Debye factor
l_D	Debye length
Ξ	Grand canonical potential
ξ	Grand canonical potential density
$\Delta\Xi$	Grand potential difference between two states

ΔG	Gibbs free energy difference between two states
Ξ_s	Grand potential of the electrolytic solvent
Ξ_e	Electrostatic energy
Ξ_{fl}	Grand canonical potential of the uncharged solvent
F	Helmholtz free energy
f	Helmholtz free energy density
P	Thermodynamic pressure (Osmotic pressure)
ϕ_{coul}	Coulombic potential
ϕ_{pol}	Polarization potential
ϕ_{ion}	Ionic potential
ΔG_{coul}	Coulombic energy
ΔG_{pol}	Polarization energy
ΔG_{ion}	Ionic energy

Numerical Symbols

W_h	Lagrange space for scalar fields on nodes
$\{w_k\}$	First-order Lagrange basis of W_h
N_v^h	Dimension of W_h
U_h	Nédélec space (first kind, degree 1) for vector fields on edges
$\{\boldsymbol{\sigma}_j\}$	Basis of U_h
N_e^h	Dimension of U_h
$\mathbf{D}_h$	Discrete dielectric displacement field
ϕ_h	Discrete electric potential
$\mathcal{T}_h$	Mesh partition of the computational domain
$\mathbb{P}_{l,m,n}(K)$	Space of polynomials in x, y, and z on K of degree at most l, m, and n respectively
$\tilde{\varepsilon}_{kn}$	Harmonic average of permittivity over nodes k and n
$\bar{\varepsilon}_{kn}$	Weighted harmonic average of permittivity over nodes k and n using MS intersection

PART II

N	Number of interacting oscillators (or particles) of unit mass
x_i	Position of the i-th particle
T_L	Temperature of the left thermostat
T_R	Temperature of the right thermostat
V	Interacting potential
a	Characteristic length
σ	Lennard-Jones distance parameter
r_i	Difference of the coordinates of two particles with consecutive labels ($x_i - x_{i+1}$)
S_i	Time average of r_i
T_i	Time average of the kinetic energy of the particle i
α	Dilation factor
x_i^{eq}	Mechanical equilibrium position of the i-th particle

Part I

Main Part: Electrostatics in Electrolytic Solutions

Part of the work discussed in this Part has also appeared in the publication:

Di Florio, V., Ansalone, P., Siryk, S. V., Decherchi, S., de Falco, C., Rocchia, W. NextGenPB: an analytically-enabled super resolution and local (de)refinement Poisson–Boltzmann Equation solver. arXiv preprint arXiv:2502.09323 (2025). `https://arxiv.org/abs/2502.09323`

Chapter 1

Introduction

Electrostatics plays a fundamental role in physics, explaining how charged particles interact. The history of electrostatics begins with Coulomb's and Gauss's laws and has evolved into modern theories for describing interactions between ions and macromolecules. These systems are generally charged entities, such as colloids, polymers, or biological macromolecules, immersed in a dielectric medium. In such environments, electrostatic forces are often driving structure, function, and stability. To better understand and model these interactions, a variety of theories and computational models were developed throughout the 20th century. Among these, we focuses on the Poisson–Boltzmann equation (PBE), which has become one of the most widely used tools for both conceptual understanding and computational modeling of electrostatics in soft matter and biomolecular systems.[1,2]

This thesis begins with a reflection on the nature and the role of the Poisson–Boltzmann theory. It is well understood as a theoretical and computational framework developed to describe electrostatics in complex systems. The Poisson–Boltzmann theory occupies a unique space: it serves both as a conceptual link between microscopic and macroscopic descriptions and as a practical tool for modeling. At its core, the theory introduces the idea of dividing a system with a dielectric interface (the molecular surface) that separates regions with distinct charge densities. This model is central in many systems of interest in soft matter physics, colloid science, and biophysics.[3,4]

The "Poisson" component of the theory originates from Maxwell's equations:

$$\nabla \cdot \mathbf{D} = \rho,$$

where **D** is the electric displacement field and ρ represents the free charge density. The complexity of the model lies in the nature of the charge density term. In this context, ρ includes both fixed charges, such as those present in the solute, and mobile ions

---

[1] Wei Yang and Walter Rocchia. "Biomolecular Electrostatic Phenomena: An Evergreen Field", 127pp. 3979–3981, 2023.

[2] Elena Besley. "Recent Developments in the Methods and Applications of Electrostatic Theory", 56pp. 2267–2277, 2023.

[3] Luc Belloni. "Colloidal interactions", 12R549, 2000.

[4] Jean-Pierre Hansen and Hartmut Löwen. "Effective interactions between electric double layers", 51pp. 209–242, 2000.

dispersed in the surrounding solvent. The behavior of the mobile ions constitutes the "Boltzmann" component of the theory. In the PB theory, their concentration depends on the local electrostatic potential and it is assumed to follow a Boltzmann distribution. As a result, the charge density becomes a nonlinear function of the electrostatic potential. This nonlinear relationship gives rise to the Poisson–Boltzmann equation, a differential equation that governs the behavior of the electrostatic potential in ionic environments:

$$\nabla \cdot \mathbf{D} = \sum_j e z_j n_j^b \exp\left\{ -\frac{e z_j \phi(\mathbf{r})}{k_B T} \right\}.$$

On the right-hand side, the summation represents the charge density of mobile ions, where e is the elementary charge, z_j is the valence of the j-th ionic species and n_j^b is its bulk concentration.
When the system considered is weakly charged the equation can be simplified by linearizing the Boltzmann term, resulting in the linearized Poisson–Boltzmann equation (LPBE). This approximation allows more analytical development and it is computationally simpler and more efficient. Despite this simplification, the LPBE retains essential insights into screening effects, potential decay, and the influence of surface charge. However, solving the LPBE, particularly in systems with complex geometries, heterogeneous environments, or biologically relevant features, remains a significant challenge. A major difficulty lies in the choice of molecular surface representation, which greatly influences the computed potential and the ability of the model to reflect biologically significant interactions.[5,6]

In general, the systems studied are too complicated for analytical techniques to be applied, for this reason, numerical procedures are invoked. Advances in numerical methods have greatly improved our ability to solve both the PBE and LPBE with increasing precision. Techniques such as finite difference,[7–10] boundary element,[11,12]

---

[5] Sergio Decherchi and Walter Rocchia. "A general and Robust Ray-Casting-Based Algorithm for Triangulating Surfaces at the Nanoscale", 8pp. 1–15, 2013.

[6] Remo Rohs et al. "The role of DNA shape in protein–DNA recognition", 461pp. 1248–1253, 2009.

[7] Lin Li et al. "DelPhi: a comprehensive suite for DelPhi software and associated resources", 5pp. 1–11, 2012.

[8] Nathan A Baker et al. "Electrostatics of nanosystems: application to microtubules and the ribosome", 98pp. 10037–10041, 2001.

[9] Jun Wang and Ray Luo. "Assessment of linear finite-difference Poisson–Boltzmann solvers", 31pp. 1689–1698, 2010.

[10] Robert C Harris, Alexander H Boschitsch, and Marcia O Fenley. "Influence of grid spacing in Poisson-Boltzmann equation binding energy estimation", 9pp. 3677–3685, 2013.

[11] Alexander H Boschitsch, Marcia O Fenley, and Huan-Xiang Zhou. "Fast boundary element method for the linear Poisson- Boltzmann equation", 106pp. 2741–2754, 2002.

[12] Christopher D Cooper, Jaydeep P Bardhan, and Lorena A Barba. "A biomolecular electrostatics solver using Python, GPUs and boundary elements that can handle solvent-filled cavities and Stern layers", 185pp. 720–729, 2014.

and finite element[13–15] methods have been adapted to handle irregular geometries and discontinuous dielectric properties. These advancements have paved the way for groundbreaking studies in areas like protein–ligand binding and understanding ion distribution near charged surfaces. However, challenges persist. For instance, the computational cost of solving the PBE in large, complex systems, such as those derived from Cryo-EM reconstructions, remains high. On top of that, accurately matching experimental observables, like solvation energies and local electric fields, continues to be a tough challenge for even the most sophisticated methods.[16,17]
This thesis introduces several innovations that aim to improve both the accuracy and efficiency of LPBE solvers. By combining insights from both analytical methods and novel numerical techniques, we refine the treatment of molecular surfaces and their surrounding electrostatic fields. Specifically, we:

- Derive, using Green's identities, expressions for potential and energies that are represented as surface integrals. This method bypasses the need for computationally expensive volumetric integrations within the solvent domain, a task that can also introduce inaccuracies depending on the chosen boundary conditions.

- Provide new analytical solutions for the LPBE, enabling the development of novel benchmark tests that can be used to assess the accuracy and robustness of LPBE solvers across different systems.

- Leverage geometric information about the molecular surface to improve the discretization of the PBE. By incorporating both numerical and physics-based enhancements to the model, we increase the accuracy of the solution near the surface, without requiring an increase in resolution at that critical location.

- Introduce a variable-resolution mesh that concentrates computational resources on the most critical regions of the system, thereby improving performance while maintaining or even improving accuracy.

These innovations have been implemented in the `NextGenPB` software package, an open-source, finite element-based Poisson–Boltzmann solver. This package is available for use at `https://github.com/vdiflorio/NextGenPB`, providing a flexible and powerful tool for researchers in the field. We validate our approach against analytical solutions for systems involving multiple non-overlapping dielectric spheres

---

[13] Stephen D Bond et al. "A first-order system least-squares finite element method for the Poisson-Boltzmann equation", 31pp. 1625–1635, 2010.

[14] Michael Holst et al. "Adaptive finite element modeling techniques for the Poisson-Boltzmann equation", 11pp. 179–214, 2012.

[15] Ilkay Sakalli, J Schoberl, and EW Knapp. "mFES: a robust molecular finite element solver for electrostatic energy computations", 10pp. 5095–5112, 2014.

[16] Junji Iwahara, B Montgomery Pettitt, and Binhan Yu. "Direct measurements of biomolecular electrostatics through experiments", 82p. 102680, 2023.

[17] Binhan Yu, Xi Wang, and Junji Iwahara. "Measuring local electrostatic potentials around nucleic acids by paramagnetic NMR spectroscopy", 13pp. 10025–10029, 2022.

in a Debye–Hückel medium and demonstrate its application to biologically relevant molecules such as proteins and nucleic acids.

Road Map: This thesis is organized as follows:

- **Chapter 2** revisits the physical and mathematical foundations of electrostatics, tracing the evolution from Gauss's law to the Poisson–Boltzmann equation. We also examine the role of PB theory as a modeling tool and introduce a thermodynamic perspective that allows for its natural extension.
- **Chapter 3** reformulates the solution to the linearized Poisson–Boltzmann equation using domain partitioning, which aids in both numerical implementation and physical interpretation. Additionally, we provide analytical solutions for simplified geometries, which serve as both pedagogical examples and benchmarks for validation.
- **Chapter 4** details the numerical framework developed in this work, focusing on advanced discretization strategies and surface-aware formulations that are specifically tailored for molecular systems.
- **Chapter 5** showcases computational results for both idealized and biologically relevant systems, demonstrating the accuracy, convergence behavior, and computational efficiency of the proposed method.
- **Chapter 6** concludes with a discussion of the current limitations of the method and outlines future directions, including potential extensions to the nonlinear Poisson–Boltzmann equation and time-dependent formulations.

Chapter 2

Electrostatics in Biomolecular Systems

Electrostatic interactions are the invisible forces that govern the stability, function, and behavior of biomolecular systems. Charged biomolecules, like proteins, nucleic acids, and lipid membranes, exist in a dynamic aqueous environment where their interactions with surrounding ions and solvent molecules dictate structural organization, molecular recognition, and enzymatic activity. These forces underpin essential biological processes such as ligand binding, catalysis, and macromolecular assembly, and they play a crucial role in drug design and the regulation of biochemical pathways at the molecular level.

Understanding electrostatics in biomolecular systems requires a multi-scale approach, as these interactions operate across vastly different spatial and temporal domains.[1,2] At the atomic scale, quantum mechanical (QM) methods[3] offer precise descriptions of electronic structure, capturing phenomena such as charge transfer, polarization, and chemical reactivity. These techniques provide fundamental insights into the nature of molecular interactions but are computationally demanding and typically limited to small systems.

At larger scales, molecular dynamics (MD) simulations[2,4] bridge the gap between atomic precision and biologically relevant timescales. In these simulations, biomolecules are embedded in explicit solvent models, where electrostatics are approximated using fixed or polarizable partial charges assigned to atoms. MD enables the study of biomolecular flexibility, conformational transitions, and the role of electrostatics in folding, binding, and allosteric regulation. Advanced techniques such as enhanced sampling and hybrid QM/MM (quantum mechanics/molecular mechanics)

---

[1] Malcolm E Davis and J Andrew McCammon. "Electrostatics in biomolecular structure and dynamics", 90pp. 509–521, 1990.

[2] G Andrés Cisneros et al. "Classical electrostatics for biomolecular simulations", 114pp. 779–814, 2014.

[3] Curt M Breneman and Kenneth B Wiberg. "Determining atom-centered monopoles from molecular electrostatic potentials. The need for high sampling density in formamide conformational analysis", 11pp. 361–373, 1990.

[4] Mark R Wilson. "Progress in computer simulations of liquid crystals", 24pp. 421–455, 2005.

approaches[2] further refine our ability to model electrostatic effects in complex environments. While these methods offer detailed insights, they become computationally expensive for large systems.

For systems involving macromolecular assemblies, membranes, or cellular environments, continuum electrostatics methods offer a powerful alternative.[5] These approaches describe the solvent as a continuous dielectric medium and model ion distributions through mean-field approximations. In this work, we focus specifically on the Poisson-Boltzmann (PB) framework, which provides an effective way to compute electrostatic potentials in complex biomolecular environments. The PB equation captures the interplay between biomolecular charge distributions and the surrounding ionic atmosphere, enabling the study of electrostatic screening, solvation energetics, and charge regulation effects.

By leveraging the Poisson-Boltzmann approach, we aim to gain a deeper understanding of electrostatic interactions in biological systems, offering insights into biomolecular stability, binding affinities, and the role of electrostatic forces in molecular recognition and self-assembly.

2.1 Elementary Electrostatic Interactions

Electrostatic interactions arise from the presence of electric charges and dipoles and play a fundamental role in stabilizing biomolecular structures and mediating interactions. In this discussion, we will neglect quantum mechanical interactions such as covalent or chemical bonding and focus on interactions that are purely electrostatic in origin. These include charge-charge, charge-dipole, and dipole-dipole interactions, each contributing uniquely to the electrostatic landscape of biomolecules.

The simplest and most direct form of electrostatic interaction is the charge-charge interaction, which is described by Coulomb's law:

$$U(r) = \frac{q_1 q_2}{4\pi\varepsilon_0 r} \tag{2.1.1}$$

where q_1 and q_2 are the interacting charges, r is the distance separating them, and ε_0 is the vacuum permittivity. This interaction is central to understanding the forces between ions and charged groups in biomolecules.

When a charge interacts with a dipole, the resulting interaction is termed a charge-dipole interaction. The potential energy of this interaction is given by:

$$U(r) = -\frac{m|q|\cos\theta}{4\pi\varepsilon_0 r^2} \tag{2.1.2}$$

where m is the dipole moment, q is the charge, and θ is the angle between the dipole moment vector and the line connecting the charge to the dipole. When averaged over all possible orientations at thermal equilibrium, the interaction energy becomes:

---

[5] Barry Honig and Anthony Nicholls. "Classical electrostatics in biology and chemistry", 268pp. 1144–1149, 1995.

$$\langle U(r) \rangle = -\frac{m^2 q^2}{6(4\pi\varepsilon_0)k_B T}\frac{1}{r^4} \tag{2.1.3}$$

which highlights the dependence of the interaction on temperature T and the Boltzmann constant k_B.
Dipole-dipole interactions arise when two dipoles interact with each other. These interactions can be further categorized into several types, depending on the nature of the dipoles involved. Dipole-dipole interactions, such as Keesom forces, describe interactions between two permanent dipoles. The thermally averaged potential energy is:

$$\langle U(r) \rangle = -\frac{m_1^2 m_2^2}{3(4\pi\varepsilon_0)^2 k_B T}\frac{1}{r^6} \tag{2.1.4}$$

where m_1 and m_2 are the dipole moments of the interacting species. This interaction energy decays faster than the previous and for this reason it is considered as short-range interaction.
Other short interactions are induced dipole interactions like Debye interactions (permanent dipole-induced dipole) and London dispersion forces (induced dipole-induced dipole). Both types of interactions contribute to the overall electrostatic stability of molecules and follow a similar distance dependence:

$$\langle U(r) \rangle \propto -\frac{1}{r^6} \tag{2.1.5}$$

These interactions are particularly important in non-polar systems.
Understanding the nature of electrostatic interactions provides the foundation for modeling biomolecular environments. Modeling these interactions in proteins is challenging due to the heterogeneous nature of the surrounding medium. In aqueous solutions, the solvent (water) is highly polar, while the protein interior is predominantly nonpolar, typically characterized by a low dielectric constant. Each charge within the protein interacts with the solvent, and when additional charges are present, they also interact with one another. However, these charge-charge interactions are modulated by the solvent. Both the interactions between charges and the solvent, as well as the solvent's screening effect on charge-charge interactions, play a critical role in determining the electrostatic energies of proteins.

2.2 The Solvent: Electrolyte Solutions

To understand electrostatics in biomolecular environments, we must first understand the solvent. An **electrolyte solution** is a solution which conducts electricity, such as water with dissolved salt that produces ions. The electrostatic interaction between water molecules and ions is not trivial and there are two main approaches to studying electrostatic interactions between ions and solvents: the explicit solvent model[6] and the implicit solvent model.[7,8]

The explicit solvent model represents individual solvent molecules and their interactions with each other, with ions, and with the solute biomolecule, as illustrated in Fig. 2.1a. While this model provides an accurate description of the system, it is computationally expensive because it requires accounting for the degrees of freedom of each solvent molecule. This makes the explicit solvent model computationally expensive for large-scale biomolecular simulations.

In contrast, the implicit solvent model treats the solvent as a continuous, polarizable medium, as shown in Fig. 2.1b. The solvent, typically polar like water, acts as an insulating medium that restricts charge flow. For this reason, it is sometimes referred to as a dielectric because it reduces the field strength, force, and electrostatic potential energy between charges. This effect is quantified by the relative permittivity, $\varepsilon_{r,s}$. Rather than resolving individual solvent molecules, the implicit solvent model captures the average electrostatic effects by representing the solvent as a dielectric continuum. This approach is supported by statistical mechanics,[8] where minimizing the system's free energy leads to an equilibrium state with ions concentrations that is a nonlinear function of the electrostatic potential.

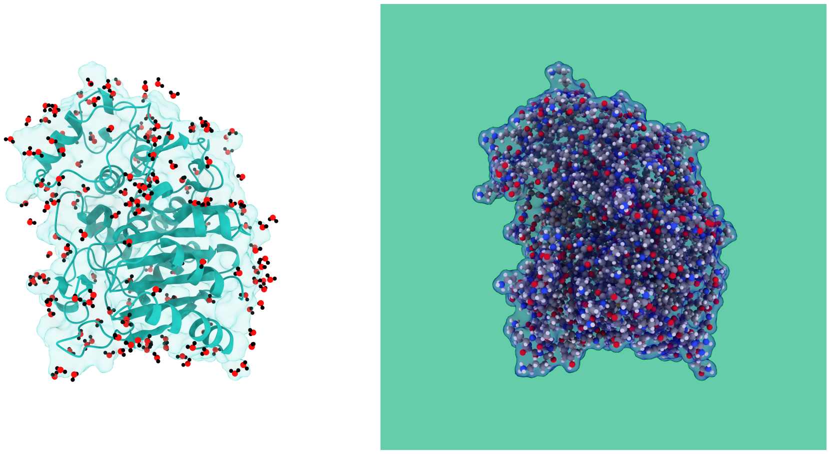

(A) Explicit solvent (B) Implicit solvent

FIGURE 2.1: Explicit and implicit solvent model schemes.

Despite the molecular complexity of ion–solvent interactions, in this study, we will rely on the continuum solvent approximation as a powerful framework for studying electrostatics in aqueous environments. By averaging out water's molecular granularity, it enables efficient computation of electrostatic potentials and forces, which

---

[6] Charles L Brooks III et al. *Proteins: a theoretical perspective of dynamics, structure and thermodynamics*. 1990.

[7] Margaret Robson Wright. *An introduction to aqueous electrolyte solutions*. John Wiley & Sons, 2007.

[8] Benoıt Roux and Thomas Simonson. "Implicit solvent models", 78pp. 1–20, 1999.

is essential for large-scale simulations. However, treating the solvent purely as a bulk medium overlooks its microscopic structure. Studies have shown that molecular details influence ion–solvent interactions, which in turn modify ion–ion and solvent–solvent interactions, significantly impacting electrolyte behavior. While these insights refine electrolyte models, incorporating them into the mathematical framework of continuum models remains a complex challenge, which we will discuss in Sec. 2.6.

2.3 Electrostatic Interactions in Electrolyte Solutions

Electrolyte solutions are mixtures of a solute, typically ions, and a solvent, such as water. In this context, ideality applies only when particle interactions are negligible, as in low-pressure gases. However, in condensed phases like liquids and solids, strong interactions dominate, making ideality an unrealistic assumption.

When studying mixtures, the distinction between ideal and non-ideal behavior is crucial. In a two-component system, composition ranges from pure A to pure B, with ideality occurring only when one component is present in vanishingly small amounts. In electrolyte solutions, this corresponds to infinite dilution, where ion–ion are negligible. As the salt concentration increases, however, these interactions become increasingly more significant, leading to deviations from the ideal behavior. Unlike neutral molecules, ions experience strong electrostatic forces, which affect their interactions with both the solvent and other ions.[7,9,10] These forces drive complex phenomena, from ion pairing to dielectric screening, making the study of electrolyte solutions rich and challenging.

In the following discussion, we explore the key interactions that arise from non-ideal behavior and how they influence the thermodynamics of electrolyte solutions.

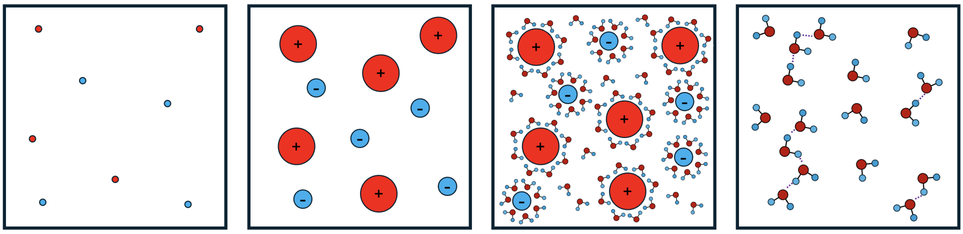

(A) Ideal solution (B) Ion-ion (C) Ion-solvent (D) solvent-solvent

FIGURE 2.2: Schematic representations of different interactions in electrolytic solutions.

---

[9] John O'M Bockris and Amulya KN Reddy. "Ion-ion interactions", pp. 225–360, 1998.

[10] John O'M Bockris and Amulya KN Reddy. "Ion-solvent interactions", pp. 35–224, 1998.

2.3.1 Ion-Ion Interactions

Ion-ion interactions arise from multiple contributions, each playing a crucial role in determining the overall behavior of the system.[9]
At large distances, ions interact primarily through electrostatic forces, which follow Coulomb's law (2.1.1). These interactions play a dominant role in determining the overall structure and stability of ionic systems. For a solution with a low concentration of ions these interactions are dominant as we will see in the Poisson-Boltzmann model.
If the ions are polarizable or are surrounded by polarizable molecules, additional interactions arise due to the induction of dipoles. This leads to an attractive interaction between the ion and the induced dipole, given by (2.1.5). This interaction decays more rapidly than Coulombic interactions, but it becomes relevant in media with high polarizability or for highly charges and small ions.
At shorter distances, additional forces contribute to ion-ion interactions, such as:

- **Van der Waals forces**, arising from fluctuating dipoles, scale as r^{-6} and provide an attractive component.

- **Hydrogen bonding** contributes to specific attractions.

Steric effects, resulting from the finite size of ions, further influence ion packing and solution behavior. Unlike idealized point charges, real ions occupy space, and their hard-core repulsion leads to excluded volume effects, see Fig 2.2b. This is particularly significant in concentrated solutions, where ion crowding alters local structure and thermodynamics. Key consequences include:[7,11,12]

- **Ion packing constraints**: The effective size and hydration shells limit how closely ions can pack together.

- **Reduced configurational entropy**: Steric hindrance confines ions, lowering entropy and modifying the free energy landscape.

- **Screening of Coulombic interactions**: In dense ionic environments, charge distributions are altered not only by solvent effects but also by steric hindrance.

2.3.2 Ion-Solvent Interactions

Ion-solvent interactions play a fundamental role in determining the behavior of ions in solution, influencing solvation structure, ionic mobility, and thermodynamic properties. These interactions depend on several factors, including the ion's charge, size, and polarizability, as well as the solvent's dielectric properties and molecular structure.

---

[11] Spiros Kournopoulos et al. "The contribution of the ion–ion and ion–solvent interactions in a molecular thermodynamic treatment of electrolyte solutions", 126pp. 9821–9839, 2022.

[12] Johan Scheers et al. "Ion–ion and ion–solvent interactions in lithium imidazolide electrolytes studied by Raman spectroscopy and DFT models", 13pp. 11136–11147, 2011.

At the fundamental level, ion-solvent interactions consist of long-range electrostatic forces and short-range effects. The first arise from ion-dipole (2.1.2) direct interactions and from shorter range ion-induced dipole interactions (2.1.3), other short-range effects include hydrogen bonding, steric constraints, and remaining Van der Waals interactions. The combination of these forces results in the formation of structured solvation shells around the ions (see Fig.2.2c). Small and highly charged ions strongly polarize nearby solvent molecules, further enhancing solvation structure and affecting macroscopic properties such as viscosity and dielectric constant.[10,13,14] These interactions also play a crucial role in determining ionic mobility and hydration free energy, which are key for biological and electrochemical systems.

A pioneering mathematical description of ion-solvent interactions was introduced by Born,[15] who formulated an expression for hydration free energy variations. The Born equation approximates the free energy of ion solvation by considering interactions beyond the first solvation shell. In this model, the ion is treated as a rigid sphere with radius a_0 and charge q, while the solvent is approximated as a homogeneous continuum with dielectric permittivity $\varepsilon_{r,s}$. The solvation energy is given by:

$$\Delta G = -\frac{N_A q^2}{8\pi\varepsilon_0 a_0}\left(1 - \frac{1}{\varepsilon_{r,s}}\right), \tag{2.3.1}$$

where N_A is Avogadro's constant. Despite its simplicity, this model provides a useful approximation for more advanced theories of ion solvation.

Beyond the Born model, ion-solvent interactions manifest in diverse ways. In aqueous solutions, ions organize surrounding water molecules into structured hydration shells due to strong electrostatic forces. Additionally, ions influence the electrostatic environment of biomolecules, leading to screening effects that modulate interactions at the molecular scale. Charged biomolecules generate electrostatic fields that attract counterions, forming an ionic atmosphere that reduces the range of Coulomb interactions. This electrostatic screening effect has significant implications for biomolecular stability, binding affinities, and macromolecular assembly, highlighting the profound role of ion-solvent interactions in biological and chemical systems.

2.3.3 Solvent-Solvent Intractions

Solvent molecules interact through both attractive and repulsive forces, shaping the structure and properties of the liquid phase.[7,16]

Attractive forces primarily arise from dipoles. Dipole–dipole interactions (2.1.4) occur between molecules with permanent dipoles, creating an attractive force. Similarly, dipole-induced dipole interactions (2.1.5) emerge when a permanent dipole

---

[13] Yan-Zhen Wei, Ping Chiang, and S Sridhar. "Ion size effects on the dynamic and static dielectric properties of aqueous alkali solutions", 96pp. 4569–4573, 1992.

[14] Xiang Ji and Shenggao Zhou. "Variational approach to concentration dependent dielectrics with the Bruggeman model: Theory and numerics", 17pp. 1949–1974, 2019.

[15] Max Born. "Volumen und hydratationswärme der ionen", 1pp. 45–48, 1920.

[16] Jacob N Israelachvili. *Intermolecular and surface forces*. Academic press, 2011.

induces a dipole in a neighboring molecule, leading to attraction. Even in nonpolar molecules, temporary electron fluctuations generate induced dipoles, resulting in dispersion forces. Additionally, quadrupole interactions, involving charge distributions beyond simple dipoles, further contribute to the complexity of molecular interactions.

Repulsive forces are equally essential in defining solvent behavior. These arise when molecules come too close together, leading to steric hindrance and electron cloud overlap, which generates quantum mechanical repulsion. Additionally, permanent dipoles can experience electrostatic repulsion when like-charged ends are forced into proximity. The balance between these attractive and repulsive forces determines the liquid's stability and structure, while the presence of solutes can further modify this equilibrium.

2.4 Molecular Volume

Defining the solute region begins with determining the molecular surface (MS), which characterizes the spatial extent of biomolecules. Proteins, nucleic acids, and small organic molecules consist of atoms arranged according to specific three-dimensional structures. To each atom are assigned a charge and a radius,[17] where charges influence electrostatic calculations, and radii—such as Van der Waals radii[18]—define the molecular surface, shaping the molecule's representation in simulations.

There are several approaches to compute molecular surfaces,[19–22] but in this section, we focus on the most widely used ones in molecular modeling: the van der Waals surface (VdWS), and two solvent-related surfaces derived from it—the Solvent Accessible Surface (SAS)[23] and the Solvent Excluded Surface (SES).[24]

Van der Waals Surface (VdWS) The VdWS is the simplest representation of a molecular boundary. It assumes that each atom is a sphere centered at position $\mathbf{r}_i \in \mathbb{R}^3$ with radius R_i, and that the molecular region is the union of all such spheres (see Fig. 2.3a.). It neglects the presence of solvent and purely reflects the space occupied by the solute atoms.

---

[17] Kenno Vanommeslaeghe, E Prabhu Raman, and Alexander D MacKerell Jr. "Automation of the CHARMM General Force Field (CGenFF) II: assignment of bonded parameters and partial atomic charges", 52pp. 3155–3168, 2012.

[18] A van Bondi. "van der Waals Volumes and Radii", 68pp. 441–451, 1964.

[19] Sergio Decherchi et al. "Between Algorithm and Model: Different Molecular Surface Definitions for the Poisson-Boltzmann Based Electrostatic Characterization of Biomolecules in Solution", 13pp. 61–89, 2013.

[20] Herbert Edelsbrunner. "Geometry for modeling biomolecules", pp. 265–277, 1998.

[21] Sergio Decherchi and Walter Rocchia. "A general and Robust Ray-Casting-Based Algorithm for Triangulating Surfaces at the Nanoscale", 8pp. 1–15, 2013.

[22] Sergio Decherchi et al. "NanoShaper–VMD interface: computing and visualizing surfaces, pockets and channels in molecular systems", 35pp. 1241–1243, 2018.

[23] Byungkook Lee and Frederic M Richards. "The interpretation of protein structures: estimation of static accessibility", 55379–IN4, 1971.

[24] Michael L Connolly. "Analytical molecular surface calculation", 16pp. 548–558, 1983.

Definition 2.4.1 (Van der Waals model)**.** *The molecular region for the Van der Waals Model is*

$$\Omega_{VdWS} = \{\mathbf{r} \in \mathbb{R}^3 \mid \exists i = 1, \dots, N \ : \| \mathbf{r} - \mathbf{r}_i \| \leq R_i\} \tag{2.4.1}$$

and the Van der Waals surface (VdWS) is

$$\Gamma_{VdW} = \partial\Omega_{VdW} \, . \tag{2.4.2}$$

This surface is fundamental in defining the core physical space occupied by a molecule, and it serves as the starting point for more refined models. It also plays a role in modeling steric interactions and Van der Waals forces between biomolecules.

Solvent Accessible Surface (SAS) The SAS represents the boundary of a molecule that can be accessed by a solvent molecule, such as water. The concept behind the SAS is that a solvent molecule, modeled as a sphere, can only approach the surface of the solute up to a certain distance, determined by the size of the solvent molecule, and by the shape of the solute. The SAS expands the VdWS by considering the space accessible to a spherical solvent probe. This model is critical for studying solvation and hydrophobic/hydrophilic surface properties.

Definition 2.4.2 (Solvent Accessible region)**.** *Let ϱ be the probe radius (e.g., 1.4 Å for water). The molecular region in the solvent accessible model is:*

$$\Omega_{SA} = \bigcup_{i=1}^{N} \{\| \mathbf{r} - \mathbf{r}_i \| \leq R_i + \varrho, \mathbf{r} \in \mathbb{R}^3\} \tag{2.4.3}$$

and the solvent accessible surface is

$$\Gamma_{SAS} = \partial\Omega_{SA} \, . \tag{2.4.4}$$

Geometrically, the SAS is formed by tracing the center of the probe sphere as it rolls over the VdW surface (see Fig. 2.3b). It delineates the regions of the molecule that can interact directly with solvent molecules and plays a key role in estimating solvation energies and binding affinities.

Solvent Excluded Surface (SES) The SES, also known as the Connolly surface,[24] refines the SAS by considering the actual physical exclusion of solvent molecules. While SAS considers where the center of a solvent probe can go, SES traces where the boundary of the probe touches the solute.

Definition 2.4.3 (Solvent Excluded region)**.** *The SES region is defined as the complement of the region where the entire solvent probe sphere can be placed without overlapping the VdW spheres:*

$$\Omega_{SE} = \Omega_{SA} \cap \{\mathbf{r} \in \mathbb{R}^3 \ : \| \mathbf{r} - \tilde{\mathbf{r}} \| > \varrho, \tilde{\mathbf{r}} \in \Gamma_{SAS}\} \tag{2.4.5}$$

and the solvent excluded surface (SES), also called Connolly surface, is:

$$\Gamma_{SES} = \partial\Omega_{SE} \, . \tag{2.4.6}$$

Visually, the SES is formed by tracing the contact surface of a probe sphere as it rolls over the VdW spheres (see Fig. 2.3c). It includes convex regions, toroidal and spherical reentrant surfaces. The SES better reflects the actual space available for interactions, making it essential in molecular docking, cavity detection, and modeling hydrophobic effects.

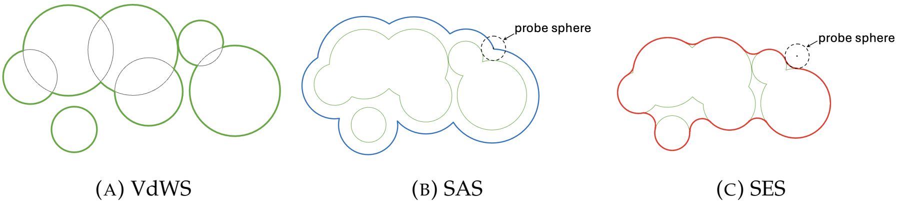

(A) VdWS (B) SAS (C) SES

FIGURE 2.3: Two-dimensional schematic representations of different molecular models.

Each of these surfaces is suited to a specific purpose. The VdWS captures the minimal solute extent, the SAS introduces solvent exposure, and the SES offers a physically grounded boundary relevant to molecular recognition and electrostatic modeling. Understanding these boundaries is foundational in continuum electrostatics, molecular docking, protein folding, and solvent modeling. However, even the most refined molecular surface cannot fully describe the complexity of the solute–solvent interface—particularly the behavior of ions near charged biomolecules.

Beyond a Single Boundary: The Stern Layer and the Electrical Double Layer Electrostatic modeling in ionic solutions requires more than just geometric surfaces. Experimental observations and theoretical considerations suggest that ions in solution do not approach arbitrarily close to the solute surface. This limitation arises due to the finite ion size and hydration shells (see Fig 2.4). Consequently, models introduce a double layer at the interface between solute and solvent. Among the most widely used is the Stern model,[25] which builds on classical double-layer theories such as Helmholtz[26] and Gouy-Chapman.[27,28]
In the Stern model, the interface is divided into:

---

[25] Otto Stern. "Zur theorie der elektrolytischen doppelschicht", 30pp. 508–516, 1924.

[26] H von Helmholtz. "Ueber einige Gesetze der Vertheilung elektrischer Ströme in körperlichen Leitern, mit Anwendung auf die thierisch-elektrischen Versuche (Schluss.)", 165pp. 353–377, 1853.

[27] MJJPTA Gouy. "Sur la constitution de la charge électrique à la surface d'un électrolyte", 9pp. 457–468, 1910.

[28] David Leonard Chapman. "LI. A contribution to the theory of electrocapillarity", 25pp. 475–481, 1913.

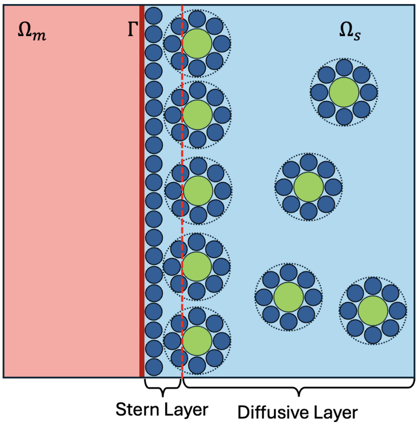

FIGURE 2.4: Two-dimensional schematic representations of electrical double layer. The blue circles are the solvent molecule and the green one are the ions.

- **Stern Layer**: A thin region adjacent to the solute where ions are excluded, or where they can make specific adsorption. This layer accounts for the minimum approach distance due to ion size and hydration. The hydration shell, composed of water molecules that reorganize around the charged ion, increases its effective radius. This prevents direct contact with the solute surface and contributes to the formation and finite thickness of the Stern layer, which typically spans 1–2 Å.

- **Diffuse Layer**: A region farther from the solute where ions distribute according to the electrostatic attraction and thermal motion.

This layered structure prevents the overestimation of screening effects that would occur if ions were allowed to accumulate unrealistically close to the solute.

Definition 2.4.4 (Stern Layer). *Let $d_S > 0$ be the its thickness, the Stern layer region is defined as:*

$$\Omega_{Stern} = \left\{ \mathbf{r} \in \mathbb{R}^3 \mid \mathbf{r} \notin \Omega_{SES} \wedge dist(\mathbf{r}, \Gamma_{SES}) < d_S \right\}. \tag{2.4.7}$$

This region is treated as a mobile ion-free zone, even though it still contains the solvent.

This reflects a more accurate physical scenario and aligns better with empirical data from electrochemistry and biophysics. Its inclusion is crucial in accurately modeling charge screening, solvation free energy, and pKa shifts in biomolecular systems.

2.5 The Poisson-Boltzmann Model

Biological systems, existing in complex aqueous environments, are influenced by solutes ranging from small ions to large biomolecules. These solutes interact with the surrounding medium, triggering solvation phenomena such as hydrogen bonding, solvent reorganization, and electrostatic screening. Water molecules restructure their hydrogen bond network, redistribute ions, and undergo polarization, while biomolecules may adapt through conformational changes and electronic polarization in response to electrostatic interactions. These processes are key to understanding solvation in biological systems.

Models of ion distributions around a charged surface start with the Helmholtz planar model (1879), considering a rigid plane of discrete countercharges, they continue with the introduction of the effects of thermal motion, leading to the concept of a diffuse layer as described by Gouy in 1910[27] and Chapman in 1913.[28] The mathematical formulation of this model is the Poisson-Boltzmann equation (PBE) in its planar form, which can be solved analytically. About 10 years later, the Debye-Hückel (D-H) theory considers an approximate model, valid for low-charged spherical solutes.[29] These theories have been fundamental in computational biophysics and materials science for modeling electrostatic interactions in ionic environments. The PBE provides a mean-field description of electrostatic interactions, representing how the electrostatic potential is distributed in systems where charged particles, such as biomolecules or colloids, are immersed in an electrolytic solvent.

Electrolytic solutions exhibit non-ideal behavior, which increases with concentration. For this reason, a theoretical description of non-ideality is also needed. This non-ideality arises from electrostatic interactions between the charged ions, and it depends on electrolyte concentration. The activity coefficient for each ionic species accounts for these interactions. The PBE offers a theoretical framework to calculate ion-specific activity coefficients and is fundamental for understanding both equilibrium and non-equilibrium properties of electrolyte solutions, such as diffusion and conductance. For these reasons, the PBE is central to the study of electrolyte solutions.

The simple D-H model focuses on screened Coulombic interactions as the primary source of non-ideality. Its goal is to calculate the mean activity coefficient of an electrolyte arising from electrostatic interactions between ions. However, this model does not account for other interactions that contribute to non-ideality, which must be included to refine the model and better match experimental results, as shown in Sec. 2.6.

2.5.1 Assumptions underlying the Debye-Hückel Theory

The simple D-H model introduces an asymmetry between the solute, that in the original formulation is an ion modeled as a hard sphere with a point charge in its center, and the counterions deriving from the electrolytic dissociation of a neutral substance. It relies on several key assumptions:[7]

---

[29] Von P Debye. "Zur theorie der electrolyte", pp. 185–206, 1923.

- It considers that the solution contains **strong electrolytes**, meaning substances that completely dissolve in water into their constituent ions. Examples include Sodium Chloride salt (NaCl), hydrochloric acid (HCl), and sodium hydroxide (NaOH).
- **Non-ideality** arises only from electrostatic interactions between counterions, which obey Coulomb's inverse square law (2.1.1). Electrostatics influences their movement and imposes some order on their random thermal motion.
- **Counterions are modeled as non-polarizable spheres of fixed charge and size**. 'Non-polarizable' means their does not change in response to external electric fields or nearby ions.
- **The aqueous solvent is modeled as a uniform medium** characterized solely by its high relative permittivity $\varepsilon_{r,s}$, with no consideration for specific interactions between ions and solvent molecules, or among solvent molecules, direct dipole interaction, or dielectric saturation or dependence on temperature.
- **No electrostriction** is allowed, meaning the solvent's density remains unchanged regardless of electric fields or ions, so there is no compression or contraction around charged particles.
- The solute ion is surrounded by an ionic atmosphere, created by the counterions in the solution. This atmosphere is **overall electrically neutral** and consists of a **continuous charge distribution**, modeled as a diffuse charge cloud. **Counterion concentration is so low to avoid interaction types other than electrostatic one.** Therefore, counterions' size is not relevant to the model and it does not appear in energy or force relationships.
- **The electrostatic potential satisfies the usual rules of electrostatics in continuum media** (i.e., Poisson equation). The sources of the field are the fixed charges on the solute and the ionic response screened by the solvent.

These assumptions allow for the simplification of the underlying problem, although they also introduce limitations, particularly in the description of short-range interactions and the detailed structure of the solvent. In Sec. 2.6, we will provide a more generic derivation of the PBE which allows us to incorporate more interaction and features of the solvent and ions.

The original D-H and Gouy-Chapman models have evolved in more advanced ones, where the solute is no longer limited to planar or spherical symmetries.[30] For instance, they now allow to describe a macromolecule (solute) as a collection of fixed charges located at atomic sites. In biomolecular electrostatics, molecules are typically modeled as a combination of overlapping spherical dielectric regions representing atoms. The volume of the protein is bounded by its molecular surface, which, in most cases, corresponds to the solvent-accessible surface (SAS) or the solvent-excluded surface (SES).

---

[30] John G Kirkwood. "Theory of solutions of molecules containing widely separated charges with special application to zwitterions", 2pp. 351–361, 1934.

2.5.2 Poisson-Boltzmann Equation

In this section, we derive the Poisson-Boltzmann equation based on the approximation discussed in Sec. 2.5.1. We define an open bounded domain $\Omega = \Omega_m \cup \Omega_s \cup \Gamma$, where Ω_m represents the region of space occupied by the solute (typically a molecule), Ω_s denotes the solvent region, and Γ is the closed surface separating them. In the context of biomolecular electrostatics, the solute is a low-dielectric medium embedded in a high-dielectric solvent containing mobile ions. The relative dielectric constant of the solute, $\varepsilon_{r,m}$, typically ranges between 2 and 4, reflecting the electronic polarization of the molecule. The solute contains all the explicitly assigned partial charges centered on the atoms. In contrast, the relative dielectric constant of the solvent, $\varepsilon_{r,s}$, is significantly higher, nearly 80, accounting for the presence of mobile ions that respond to the local electrostatic potential.

From a physical standpoint, both atomic charges and mobile ions contribute to the free charge in the system. However, there is a significant modeling distinction between them: atomic charges are prescribed as input to the equation, while ionic densities result from the calculation, as the model prescribes a relationship between the ionic response and the local electric field.

In this framework, the polarization response is described by a piecewise constant dielectric function:

$$\varepsilon(\mathbf{r}) = \begin{cases} \varepsilon_m = \varepsilon_0 \varepsilon_{r,m} & \text{if } \mathbf{r} \in \Omega_m \\ \varepsilon_s = \varepsilon_0 \varepsilon_{r,s} & \text{if } \mathbf{r} \in \Omega_s \end{cases} , \tag{2.5.1}$$

where ε_m and ε_s are the permittivities of molecule and solvent, respectively.
Gauss's law can describe the electrostatics of this system for the electric displacement in differential form:

$$\nabla \cdot (\varepsilon(\mathbf{r}) \nabla \phi) = -\rho = -\rho^f - \rho^m \quad \mathbf{r} \in \Omega \, , \tag{2.5.2}$$

where ρ^f is the fixed charge density present only inside the molecule, and ρ^m is the ionic charge present only in the solvent. The fixed charge density, composed of point charges, is defined as:

$$\rho^f(\mathbf{r}) = \sum_{i=1}^{N} q_i \delta(\mathbf{r} - \mathbf{r}_i) \, , \tag{2.5.3}$$

where $\mathbf{r}_i \in \Omega_m$ denotes the position of the i–th charge.
For the ionic charge ρ^m, we assume the density of each ion species is continuous. The total charge density is:

$$\rho^m = \sum_{j=1}^{J} e z_j n_j \, , \tag{2.5.4}$$

where J is the number of ionic species, n_j and z_j are the local concentration and the valence of the j-th species, and, e is the elementary charge.

Regarding the concentrations n_j of different ionic species in the solvent, it is important to note that the study of intermolecular forces between molecules or particles in a liquid medium reveals several effects that are absent in free space. These effects arise because interactions in a medium inherently involve multiple solvent molecules, making them many-body interactions. These collective influences are commonly referred to as solvent effects or medium effects.[7,16] The energy needed to move an individual molecule from vacuum to a solvent, denoted as μ, represents the sum of its interactions with the new surrounding environment. This quantity also accounts for any modifications in the solvent's energy induced by the presence of the solute molecule and it is often called **chemical potential**. However, determining μ in a liquid solely based on a pair potential function is highly complex, as the mean number of neighboring molecules interacting with a given molecule is not known a priori.

To build up toward the PB framework, we begin with an idealized case: a system of uncharged particles. In this scenario, there are no electrostatic interactions, and if the solution is sufficiently dilute, even short-range, non-electrostatic interactions can be neglected. Under these assumptions, and assuming equilibrium at constant temperature and pressure, the chemical potentials of each particle species is:[31]

$$\mu_j = k_B T \log a_j n_j = \text{uniform} \quad \forall j = 1, \ldots, J \, , \tag{2.5.5}$$

where a_j represents the volume occupied by a single hydrated ion of species j. The product $a_j n_j$ corresponds to the volume fraction of the species j, denoted by θ_j, i.e., the fraction of the solution volume occupied by ions of type j. This can be interpreted as the ratio between the number of ions N_j and the maximum number of such ions that could fit in the volume V, denoted N_j^{max}. Indeed,

$$\theta_j = a_j n_j = N_j \frac{a_j}{V} = \frac{N_j}{N_j^{max}} \, . \tag{2.5.6}$$

By definition, the volume fractions satisfy $0 \leq \theta_j \leq 1$ for all j. This quantity will play a fundamental role when explicitly accounting for the finite volume of ions in the PB theory; see Sec. 2.6.

As we move away from the ideal case, deviations due to inter-particle interactions become significant. These non-idealities can be introduced via an activity coefficient γ_j, specific to each species, which modifies the chemical potential to:[31,32]

$$\mu_j = k_B T \log a_j n_j + k_B T \log \gamma_j \quad \forall j = 1, \ldots, J \, . \tag{2.5.7}$$

---

[31] Peter William Atkins, Julio De Paula, and James Keeler. *Atkins' physical chemistry*. Oxford university press, 2023.

[32] Terrell L Hill. *An introduction to statistical thermodynamics*. Courier Corporation, 1986.

The additional term $k_BT \log \gamma_j$ quantifies the isothermal reversible work needed to insert a particle of species j into the system, accounting for interactions with its environment. In the PB theory, we consider solutions dilute enough that deviations from ideality arise solely from long-range Coulombic interactions, while short-range (e.g., hard-sphere) effects are neglected. Within this framework, the considered particles are ions and the activity coefficient becomes purely electrostatic in nature, leading to the relation:

$$k_BT \log \gamma_j = ez_j\phi(\mathbf{r}) \,, \tag{2.5.8}$$

where $\phi(\mathbf{r})$ is the electrostatic potential at position $\mathbf{r}$. Substituting into the expression Eq. (2.5.7), we obtain the chemical potential used in the D–H model:

$$\mu_j = k_BT \log a_j n_j + ez_j\phi(\mathbf{r}) \quad \forall j = 1, \dots, J \tag{2.5.9}$$

Although it is possible to modify the term $k_BT \log \gamma_j$ to account for additional non-ideal effects,[32] these will be addressed using a different formalism in Sec. 2.6. At equilibrium, the chemical potential (2.5.7) is spatially uniform. This implies that, in the presence of an electric potential, the ion densities are not uniform but instead redistribute according to the electrostatic potential, ensuring that μ_j remains constant throughout the system.

From Eq. (2.5.9), at equilibrium, the local concentration of each ionic species follows a Boltzmann-weighted distribution relative to its bulk concentration n_j^b:

$$\rho^m(\mathbf{r}) = \sum_{j=1}^{J} ez_j n_j^b \exp\left[-\frac{ez_j\phi(\mathbf{r})}{k_BT}\right]\chi_{\Omega_s}(\mathbf{r}) \tag{2.5.10}$$

where χ_{Ω_s} is the characteristic function that equals 1 when $\mathbf{r} \in \Omega_s$ and 0 otherwise. The bulk concentration is the concentration of the ions in absence of any external potential, and it is given by:

$$n_j^b = \frac{1}{a_j} \exp\left(\frac{\mu_j}{k_BT}\right) \,.$$

and it is such that the ion densities satisfy the overall electroneutrality condition:

$$\sum_{j=1}^{J} z_j e n_j^b = 0 \,. \tag{2.5.11}$$

All these assumptions yield to the Poisson-Boltzmann equation:

$$\nabla \cdot (\varepsilon(\mathbf{r})\nabla\phi) = -\sum_{i=1}^{N} q_i\delta(\mathbf{r}-\mathbf{r}_i) - \sum_{j=1}^{J}\left[ez_j n_j^b \exp\left\{-\frac{ez_j\phi(\mathbf{r})}{k_B T}\right\}\right]\chi_{\Omega_s}(\mathbf{r}) \qquad (2.5.12)$$

When the Stern layer model is applied, it is assumed that the ion distribution does not extend into the Stern layer, effectively excluding it from the solvent region. In this case, $\chi_{\Omega_s}(\mathbf{r}) = 0$ inside the Stern layer, and the ionic contributions are excluded from this region. This ensures that the electrostatic potential is influenced only by ions in the solvent region and excludes any effects from ions in the Stern layer.

For low-charged systems, the resulting potential in solution may satisfy the following relationship: $|\frac{ez_j\phi(\mathbf{r})}{k_B T}| \ll 1$. Under this condition and assuming electroneutrality, the local concentration of ions can be approximated as a linear function of the potential:

$$\rho^m(\mathbf{r}) \approx -\varepsilon_s k_D^2 \chi_{\Omega_s}(\mathbf{r})\phi(\mathbf{r}) = -c(\mathbf{r})\phi(\mathbf{r})\,, \qquad (2.5.13)$$

where k_D is the Debye factor of the solution, the reciprocal of the Debye screening length:

$$\frac{1}{k_D} = l_D = \sqrt{\frac{\varepsilon_0 k_B T}{e^2\sum_{j=1}^{J} z_j^2 n_j^b}}\,. \qquad (2.5.14)$$

The Debye length l_D characterizes the distance over which electrostatic interactions remain significant in an electrolyte solution.

This approximation leads to the D-H, or linear Poisson-Boltzmann equation (LPBE):

$$\nabla \cdot (\varepsilon(\mathbf{r})\nabla\phi) = -\sum_{i=1}^{N} q_i\delta(\mathbf{r}-\mathbf{r}_i) + c(\mathbf{r})\phi(\mathbf{r}) \qquad \mathbf{r}\in\Omega\,. \qquad (2.5.15)$$

Equation (2.5.15) is a linear, elliptic partial differential equation that is more manageable both numerically and analytically than its nonlinear counterpart, making it the most commonly used equation for studying biomolecular electrostatics. It is particularly suitable for describing dilute solutions, where the ionic strength, $I = \frac{1}{2}\sum_{j=1}^{J} z_j^2 n_j^b$, is relatively low. In these cases, the linearized model effectively captures the non-ideal behavior of the solution without the added complexity introduced by the nonlinear nature of the full PBE. In high-ionic-strength environments, strong screening effects lead to a rapid decay of electrostatic potentials requiring the inclusion of nonlinear terms. Similarly, in systems with highly charged surfaces or solutes, the electrostatic potential becomes sufficiently large that linear approximations break down, and the full nonlinear PB equation must be employed.

2.6 Thermodynamic Approach: Generalized PBE

The PBE is a foundational tool in modeling electrostatic interactions in soft matter and biological systems. Despite its widespread use, the PBE has well-recognized limitations arising from the assumptions embedded in its derivation. In the previous section, we derived the PBE under a set of simplifying assumptions regarding ion-ion, ion-solvent and solvent-solvent interactions. These effects become significant in various physical and biological contexts, necessitating refinements of the PBE framework. To address these limitations, a range of extended models have been developed. Some incorporate explicit ion-solvent interactions by modifying the free energy functional,[14,33,34] while others adopt hybrid schemes that couple continuum electrostatics with particle-based methods such as molecular dynamics.[35,36] In this section, we present a thermodynamic framework for such extensions, deriving a generalized form of the PBE from a functional of a thermodynamic potential.[34,37,38]

We consider a system composed of a solute with fixed charges immersed in an electrolyte solution. In this context, the solute acts as a static source of the electrostatic potential, while the solvent is treated as a continuous thermodynamic medium. To describe the equilibrium distribution of mobile ions in this setting, it is necessary to adopt a statistical mechanical ensemble that naturally accounts for the exchange of particles with the surroundings. This is particularly important for systems in contact with a bulk reservoir, such as biological cells or electrochemical devices, where the ion concentrations are not fixed but determined by thermodynamic equilibrium with the environment. The grand canonical potential is particularly well-suited to this task. In this ensemble, the system is described in terms of the temperature T, volume V, and the set of chemical potentials $\{\mu_j\}_{j=1}^{J}$associated with each ionic species. This contrasts with the canonical ensemble, where the number of particles $\{N_j\}_{j=1}^{J}$ is held fixed. The use of chemical potentials as control parameters offers several physical and mathematical advantages:

- **Chemical Potential as a Driving Force**: The chemical potential μ_j quantifies the free energy cost of adding a particle of species j to the system. At equilibrium, μ_j must be spatially uniform, ensuring that there is no net flux of particles. This condition directly determines the steady-state ion distributions in the electrolyte.

---

[33] Itamar Borukhov, David Andelman, and Henri Orland. "Steric effects in electrolytes: A modified Poisson-Boltzmann equation", 79p. 435, 1997.

[34] AC Maggs and R Podgornik. "General theory of asymmetric steric interactions in electrostatic double layers", 12pp. 1219–1229, 2016.

[35] EG Flekkøy, G Wagner, and J Feder. "Hybrid model for combined particle and continuum dynamics", 52p. 271, 2000.

[36] Khaled M Mohamed and AA Mohamad. "A review of the development of hybrid atomistic–continuum methods for dense fluids", 8pp. 283–302, 2010.

[37] Yan Levin and Michael E Fisher. "Criticality in the hard-sphere ionic fluid", 225pp. 164–220, 1996.

[38] Ralf Blossey. In: "The Poisson-Boltzmann Equation". Pp. 1–25. Cham: Springer International Publishing, 2023. DOI: `10.1007/978-3-031-24782-8`.

- **Connection to Experimental Conditions**: In many practical scenarios, such as systems in contact with a particle reservoir (e.g., a bulk electrolyte solution), the chemical potentials $\{\mu_j\}_{j=1}^{J}$ are fixed by external conditions. By working in the grand canonical ensemble, we directly incorporate these experimental constraints into our theoretical framework, allowing us to describe systems where ion concentrations are determined by their equilibrium with a reservoir.

- **Mathematical Convenience**: The grand canonical potential automatically accounts for fluctuations in particle numbers and simplifies the derivation of equilibrium conditions, especially in spatially varying systems such as those influenced by electrostatic fields.

Let us define solvent as the mixture of J ionic species dissolved in a uniform medium (made of "implicit" water), at constant temperature T and volume V. The solvent grand canonical potential $\Xi_s\ (T, V, \{\mu_j\}_{j=1}^{J})$ can be defined as the Legendre transform of the Helmholtz free energy $F\ (T, V, \{N_j\}_{j=1}^{J})$:

$$\begin{aligned}\Xi_s(T, V, \{\mu_j\}) &= \min_{\{N_j\}} \left(F(T, V, \{N_j\}) - \sum_{j=1}^{J} \mu_j N_j \right) \\ &= \left[F(T, V, \{N_j\}) - \sum_{j=1}^{J} \mu_j N_j \right]_{\{N_j\}=\{N_j^*\}}\end{aligned} \tag{2.6.1}$$

where N_j^* is such that:

$$\mu_j = \left(\frac{\partial F}{\partial N_j} \right)_{T,V,N_{i\neq j}} (N_j^*)\ . \tag{2.6.2}$$

The chemical potential μ_j governs how energetically favorable it is to add or remove particles of species j. The higher it is, the more favorable it is to have more $j-$particles. Just as the Boltzmann factor $e^{-\beta E}$ weights energy states in the canonical ensemble, the grand canonical ensemble weights configurations by $e^{-\beta(E-\sum_j \mu_j N_j)}$, accounting for both energetic and compositional fluctuations due to particle exchange with a reservoir.

The chemical potential of each species, μ_j, can be decomposed into the following contributions:

$$\mu_j = \mu_j^{ent} + \mu_j^{ne} + \mu_j^{e} \tag{2.6.3}$$

where μ_j^{ent} represents the entropic contribution, typically arising from the ideal mixing of indistinguishable particles. It captures the entropy of mixing and translational

motion, reflecting the configurational degeneracy — the number of microscopic arrangements consistent with a given macroscopic state. The term μ_j^{ne} accounts for all non-electrostatic contributions (e.g., steric, Van der Waals, in case they are fully considered apart from electrostatics, as often done), and μ_j^{e} represents the purely electrostatic contribution, arising from interactions with the mean electrostatic potential generated by the charge distribution in the system. This linear decomposition assumes that the corresponding energy contributions are additive and that there is no cross-coupling between electrostatic and non-electrostatic interactions.
The differential form of the grand potential reads:

$$\mathrm{d}\Xi_s = -S\mathrm{d}T - P\mathrm{d}V - \sum_{j=1}^{J} N_j \mathrm{d}\mu_j \,, \tag{2.6.4}$$

from which the standard thermodynamic quantities can be derived:

$$S = -\left(\frac{\partial \Xi_s}{\partial T}\right)_{V,\{\mu_j\}_{j=1}^J} \,, \quad P = -\left(\frac{\partial \Xi_s}{\partial V}\right)_{T,\{\mu_j\}_{j=1}^J} \,, \quad N_j = -\left(\frac{\partial \Xi_s}{\partial \mu_j}\right)_{T,V,\{\mu_k\}_{k\neq j}} \,. \tag{2.6.5}$$

Since Ξ_s is a thermodynamic potential, it is an extensive variable, scaling proportionally with the system size. This is formally captured by the concept of a homogeneous function:

Definition 2.6.1 (Homogeneous function of degree p)**.** *A function $z(X_1, X_2, \ldots, X_n)$ is said to be homogeneous of degree p if, for any scalar $\lambda > 0$, it satisfies the scaling property:*

$$z(\lambda X_1, \lambda X_2, \ldots, \lambda X_n) = \lambda^p z(X_1, X_2, \ldots, X_n) \,. \tag{2.6.6}$$

In this framework, the grand potential is homogeneous of degree 1 in the volume:

$$\Xi_s(T, \lambda V, \{\mu_j\}_{j=1}^J) = \lambda \Xi_s(T, V, \{\mu_j\}_{j=1}^J) \quad \forall \lambda > 0 \,.$$

Applying Euler's homogeneous function theorem, we can express Ξ_s in the following way:

$$\Xi_s(T, V, \{\mu_j\}_{j=1}^J) = V \left(\frac{\partial \Xi_s}{\partial V}\right)_{T,\{\mu_j\}_{j=1}^J} = -PV \tag{2.6.7}$$

To transition from a global to a local description, we assume the system is locally in thermodynamic equilibrium (i.e., we invoke the local thermodynamic approximation). In simple terms, we divide the region Ω_s occupied by the solvent into *"physical infinitesimals"* volume elements, that is, regions small enough from the perspective of a macroscopic observer for the limiting process to be valid and for all physical observables to be considered uniform within them, yet still large enough to contain enough particles to permit meaningful thermodynamic averaging.

This allows us to define a *grand potential spatial density* ξ_s at each location $\mathbf{r}$ pointing at any of such infinitesimals in the region Ω_s:

$$\xi_s(T, \{\mu_j(\mathbf{r})\}) = f(\mathbf{r}) - \sum_{j=1}^{J} \mu_j(\mathbf{r}) n_j(\mathbf{r}) = -P(T, \{\mu_j(\mathbf{r})\}) \quad \forall \mathbf{r} \in \Omega_s \tag{2.6.8}$$

where f is the Helmholtz free energy density, $n_j(\mathbf{r})$ and $\mu_j(\mathbf{r})$ are the local number density and the local chemical potential of species j, respectively. Integrating this density over the solvent domain yields back the grand potential:

$$\Xi_s(T, V, \{\mu_j\}) = \int_{\mathbb{R}^3} \chi_{\Omega_s}(\mathbf{r}) \xi_s(T, \{\mu_j(\mathbf{r})\}) \, \mathrm{d}\mathbf{r} \,, \tag{2.6.9}$$

where $V = \int_{\mathbb{R}^3} \chi_{\Omega_s}(\mathbf{r}) \, \mathrm{d}\mathbf{r}$ is the total volume of Ω_s, χ_{Ω_s} is the characteristic function of the solvent region. The global chemical potentials μ_j can be obtained as volume-weighted averages:

$$\mu_j = \frac{1}{V} \int_{\mathbb{R}^3} \chi_{\Omega_s}(\mathbf{r}) \, \mu_j(\mathbf{r}) \, \mathrm{d}\mathbf{r} \quad \forall j = 1, \ldots, J \,.$$

Interestingly, this formalism also provides a framework to treat situations slightly out of equilibrium, such as local variations in concentration or chemical potential.

To describe the full system, which includes the solute and the solvent, we must add the energy of the fixed charge distribution, denoted E^{fix}. Combining this with the expression for Ξ_s, the total grand potential becomes:

$$\begin{aligned} \Xi &= E^{fix} + \Xi_s \\ &= E^{fix} - \int_{\Omega} \chi_{\Omega_s} \mu_j^e n_j \mathrm{d}r + \int_{\Omega} \chi_{\Omega_s} \left[f(T, \{n_j\}_{j=1}^{J}) - \sum_{j=1}^{J} (\mu_j^{ent} + \mu_j^{ne}) n_j \right] \, \mathrm{d}\mathbf{r} \\ &= \Xi_e + \Xi_{fl} \,. \end{aligned} \tag{2.6.10}$$

Here, Ξ_e is the energy contribution due to the electrostatic interactions and Ξ_{fl} represents the grand potential of an uncharged fluid mixture of J species. This decomposition forms the thermodynamic basis for a variational derivation of generalized Poisson–Boltzmann-type equations, where each contribution can be modeled or approximated depending on the physical regime of interest.[34,38]

The electrostatic energy of the system is given by:

$$\Xi_e = \frac{1}{2} \int_{\Omega} \rho \phi \, \mathrm{d}\mathbf{r} \tag{2.6.11}$$

where ρ is the total charge density, and ϕ is the electrostatic potential. According to Gauss's law:

$$\nabla \cdot \mathbf{D}(\mathbf{r}) = \rho(\mathbf{r}) = \rho^f(\mathbf{r}) + \rho^m(\mathbf{r}) = \rho^f(\mathbf{r}) + e \sum_{j=1}^{J} z_j n_j(\mathbf{r}) \,, \tag{2.6.12}$$

where ρ^f corresponds to the distribution of fixed charges within the molecular solute (see Eq.(2.5.3)), and ρ^m denotes the contribution from mobile ions in solution (see Eq.(2.5.4)).

By substituting Eq.(2.6.12) into Eq.(2.6.11), the electrostatic energy becomes:

$$\begin{aligned}
\Xi_e &= \frac{1}{2} \int_\Omega \rho(\mathbf{r})\phi(\mathbf{r}) \mathrm{d}\mathbf{r} \\
&= \frac{1}{2} \int_\Omega \left(2\rho(\mathbf{r}) - \nabla \cdot \mathbf{D}\right) \phi(\mathbf{r}) \mathrm{d}\mathbf{r} \\
&= \int_\Omega \left[(\rho^f + \chi_{\Omega_s} e \sum_{j=1}^{J} z_j n_j)\phi - \frac{1}{2}\mathbf{D} \cdot \mathbf{E} \right] \mathrm{d}\mathbf{r} - \oint_{\partial\Omega} \varepsilon\phi \mathbf{E} \cdot \mathbf{n}(\mathbf{r}) \mathrm{d}S \\
&= \int_\Omega \left[\rho^f \phi - \frac{1}{2}\mathbf{D} \cdot \mathbf{E} \right] \mathrm{d}\mathbf{r} - \int_\Omega \chi_{\Omega_s} \sum_{j=1}^{J} \mu_j^e n_j - \oint_{\partial\Omega} \varepsilon\phi \mathbf{E} \cdot \mathbf{n}(\mathbf{r}) \mathrm{d}S \,,
\end{aligned} \tag{2.6.13}$$

where the electrostatic part of the chemical potential is:

$$\mu_j^e(\mathbf{r}) = -e z_j \phi(\mathbf{r}) \,. \tag{2.6.14}$$

If Ω extends to infinity or if Dirichlet boundary conditions $\phi|_{\partial\Omega} = 0$ are imposed, the surface integral in Eq. (2.6.13) vanishes.

Combining the fluid and electrostatic contributions, the total free energy of the system becomes:

$$\begin{aligned}
\Xi = &\int_\Omega \chi_{\Omega_s} \left[f(T, \{n_j\}_{j=1}^{J}) - \sum_{j=1}^{J} \mu_j n_j \right] \\
&+ \int_\Omega \left[\rho^f \phi - \frac{1}{2}\mathbf{D} \cdot \mathbf{E} \right] \mathrm{d}\mathbf{r} - \oint_{\partial\Omega} \varepsilon\phi \mathbf{E} \cdot \mathbf{n}(\mathbf{r}) \mathrm{d}S \,.
\end{aligned} \tag{2.6.15}$$

The total chemical potential of each ion species in the presence of electrostatic interaction is:

$$\mu_j = \mu_j^{ent}(\mathbf{r}) + \mu_j^{ne}(\mathbf{r}) - e z_j \phi(\mathbf{r}) = \text{uniform} \,. \tag{2.6.16}$$

The presence of the electrostatic field renders μ_j^{ent} non-uniform, but at thermodynamic equilibrium, it varies so that the total chemical potential remains spatially constant. As a result, the fluid pressure (or osmotic pressure) is also influenced by the electrostatic field:

$$-P(\mathbf{r}) = f(\mathbf{r}) - \sum_{j=1}^{N} \mu_j n_j(\mathbf{r}) = f - \sum_{j=1}^{N} [\mu_j^{ent}(\mathbf{r}) + \mu_j^{ne}(\mathbf{r}) - ez_j\phi(\mathbf{r})] n_j(\mathbf{r}) \tag{2.6.17}$$

The free energy Ξ is a state function, meaning its value depends only on the current state of the system and not on the path taken to reach that state. This property allows us to focus on the change in free energy $\Delta\Xi = \Xi - \Xi_0$ rather than its absolute value (Ξ_0 is a reference state typically chosen such that $\Delta\Xi = 0$ when $\phi = 0$). Since $\Delta\Xi$ represents the difference between the final and initial states, it is the key quantity for determining whether a process occurs spontaneously, without requiring knowledge of the intermediate steps. This feature is also practically important: in experiments, we do not measure absolute energies, but rather energy differences between states. If the total number of ions and the system volume remain constant between these states, then $\Delta\Xi$ is equal to the change in Gibbs free energy ΔG:

$$\Delta G = \Delta\Xi + \mu\Delta N + P\Delta V = \Delta\Xi \,. \tag{2.6.18}$$

This equivalence is particularly useful, as most experimental setups involve solutions in equilibrium with the ambient pressure, into which a fixed amount of salt is dissolved. In such conditions, the number of ions remains constant and volume changes are generally negligible. Therefore, even when computing the grand potential difference numerically or analytically, the results can be directly compared with experimental measurements. In the following chapters, we will adopt the notation ΔG, which is more commonly used in the literature.

At fixed thermodynamic variables $(T, V, \{\mu_j\}_{j=1}^{J})$, the free energy Ξ becomes a functional of of the electrostatic potential and the ion densities:

$$\Xi[\phi, \{n_j\}_{j=1}^{J}] = \int_{\Omega} \xi(\mathbf{r}; \phi, \nabla\phi(\mathbf{r}); \{n_j(\mathbf{r})\}) \mathrm{d}\mathbf{r} \tag{2.6.19}$$

where

$$\xi = \rho^f \phi - \frac{\varepsilon}{2}(\nabla\phi)^2 - P(T, \{n_j\}_{j=1}^{J}) \,. \tag{2.6.20}$$

To find equilibrium, we look for stationary points (minima or saddle points) of the functional Ξ. This means taking functional derivatives with respect to ϕ and n_j, and setting them to zero. The electrostatic potential $\phi(\mathbf{r})$ is a stationary point for the energy functional (2.6.19) if and only if it satisfies the Euler–Lagrange equation:

$$\frac{\partial \xi}{\partial \phi} - \nabla \frac{\partial \xi}{\partial (\nabla \phi)} = 0 \tag{2.6.21}$$

Neglecting the boundary term, Eq (2.6.21) simplifies to:

$$\nabla \cdot (\varepsilon \nabla \phi) - \frac{\partial P(T, \{\mu_j\}_{j=1}^{J})}{\partial \phi} + \rho^f = 0 \ . \tag{2.6.22}$$

This is the generalized Poisson–Boltzmann equation, which connects the potential ϕ to the pressure function P. Using the the relation in Eq. (2.6.17), we find:

$$-\frac{\partial P}{\partial \phi} = \sum_{j=1}^{J} e z_j n_j = \rho^m \ , \tag{2.6.23}$$

which leads to the Poisson equation:

$$-\nabla \cdot (\varepsilon \nabla \phi) = \rho^f + \rho^m \ . \tag{2.6.24}$$

Since the ξ does not depend on the derivative of n_j, the functional derivative simplifies to an ordinary derivative:

$$\frac{\partial \xi}{\partial n_j} = 0 \qquad \forall j = 1, \ldots, J \ . \tag{2.6.25}$$

This condition provides the equilibrium relation between ion densities and the local electrostatic potential, determined by the equation of state of the fluid. It's the generalized version of the Boltzmann distribution.

Together, the stationary conditions: the generalized Poisson equation for ϕ (Eq. (2.6.22)), and the equilibrium condition for each n_j (Eq. (2.6.25)), form a generalized Poisson–Boltzmann framework. This is very flexible: by choosing different pressure functions P (or free energy densities f), one can derive models that incorporate excluded volume effects, correlations, steric effects, or more realistic equations of state beyond the ideal gas. The primary challenge lies in constructing $f(T, \{n_j\}_{j=1}^{J})$ approximately as a sum of terms each embodying contributions from specific physical mechanisms and degrees of freedom. In the following, we will provide some examples, deriving the classical PBE and two of its modifications, illustrating how different interactions can be incorporated into this generalized framework.

2.6.1 PBE

If the free energy density of the fluid, $f(T,\{n_j\}_{j=1}^{J})$, is known, we can express the total free energy of the system. Furthermore, if the equilibrium densities of the ions can be explicitly determined, we can derive the osmotic pressure of the system. For instance, following the assumptions outlined in Sec. 2.5.1, we can model the ions as a mixture of ideal gases. In this case, the free energy density is given by:

$$f(T,\{n_j\}_{j=1}^{J}) = k_B T \sum_{j=1}^{J} n_j \left[\log a_j n_j - 1\right] \;, \tag{2.6.26}$$

where a_j represents the effective volume of the j-th species of hydrated ions.
Substituting f into the total free energy expression (2.6.15) and neglecting the surface contribution, we obtain:

$$\begin{aligned}\Xi = &\int_{\Omega} \chi_{\Omega_s} k_B T \sum_{j=1}^{J} n_j \left[(\log a_j n_j - 1) - \mu_j^{ent} + e z_j \phi\right] \\ &+ \int_{\Omega} \left[\rho^f \phi - \frac{1}{2}\mathbf{D}\cdot\mathbf{E}\right] \mathrm{d}\mathbf{r}\end{aligned} \tag{2.6.27}$$

Using Eq. (2.6.25), the equilibrium density of the ions can be expressed as:

$$n_j = \frac{1}{a_j}\exp\left\{\frac{\mu_j}{k_B T}\right\} = \frac{1}{a_j}\exp\left\{\frac{\mu_j^{ent}}{k_B T}\right\}\exp\left\{\frac{-e z_j \phi}{k_B T}\right\} = n_j^b \exp\left\{\frac{-e z_j \phi}{k_B T}\right\}, \tag{2.6.28}$$

where n_j^b is the bulk density of j-th ion species in the absence of electrostatic forces. This expression corresponds to the Poisson-Boltzmann density (2.5.10), which describes the distribution of ions in the presence of an electrostatic potential.
The osmotic pressure of the system can then be derived as:

$$P(T,\{n_j\}_{j=1}^{J}) = \sum_{j=1}^{J} \mu_j n_j - f(T,\{n_j\}_{j=1}^{J}) = k_B T \sum_{j=1}^{J} n_j \,. \tag{2.6.29}$$

For a monovalent salt consisting of two ionic species with a $(Z : Z)$ charge ratio, where $z_1 = -z_2 = Z$, the pressure simplifies to:

$$P = 2 k_B T n^b \cosh \frac{q\phi}{k_B T} \;, \tag{2.6.30}$$

where $q = eZ$. Substituting this result into the total free energy expression, we obtain:

$$\Xi = \int_V \left[\rho^f \phi - \frac{\varepsilon}{2} (\nabla \phi)^2 - \chi_{\Omega_s} \, 2 k_B T n^b \cosh \frac{q\phi}{k_B T} \right] \mathrm{d}\mathbf{r} \,. \tag{2.6.31}$$

Since the energy is defined up to a constant, we impose that $\Delta G = 0$ when $\phi = 0$, leading to:[39]

$$\Delta \Xi = \int_V \left[\rho^f \phi - \frac{\varepsilon}{2} (\nabla \phi)^2 - \chi_{\Omega_s} \, 2 k_B T n^b \left(\cosh \frac{q\phi}{k_B T} - 1 \right) \right] \mathrm{d}\mathbf{r} \,. \tag{2.6.32}$$

The corresponding Euler-Lagrange equation for the electrostatic potential ϕ is:

$$\nabla \cdot (\varepsilon(\mathbf{r}) \nabla \phi) = - \sum_{i=1}^{N} q_i \delta(\mathbf{r} - \mathbf{r}_i) + \chi_{\Omega_s} \, 2 k_B T n^b \sinh \frac{q\phi}{k_B T} \,. \tag{2.6.33}$$

For weakly charged systems, under the electroneutrality condition, this equation can be approximated by the LPBE for a monovalent salt:

$$\nabla \cdot (\varepsilon(\mathbf{r}) \nabla \phi) = - \sum_{i=1}^{N} q_i \delta(\mathbf{r} - \mathbf{r}_i) + c(\mathbf{r}) \phi(\mathbf{r}) \,, \tag{2.6.34}$$

where $c(\mathbf{r}) = \chi_{\Omega_s}(\mathbf{r}) \, 2 \dfrac{e^2 n_b}{k_B T}$.

2.6.2 Size of Ions: Steric Effects

In electrolyte solutions with high ion concentrations, steric effects become significant. These effects arise from the finite size of ions, which restricts their spatial distribution and lead to the saturation of ion density near charged surfaces. As a result, the standard PBE must be modified to incorporate these constraints.[34,40–44]

To begin, consider a solution containing J ion species. As previously defined, the volume fraction of species j is given by $\theta_j = a_j n_j$, where a_j is the effective volume occupied by a hydrated ion. For simplicity, in what follows, we assume that all ions

---

[39] Kim A Sharp and Barry Honig. "Calculating total electrostatic energies with the nonlinear Poisson-Boltzmann equation", 94pp. 7684–7692, 1990.

[40] Dan Ben-Yaakov, David Andelman, and Rudi Podgornik. "Dielectric decrement as a source of ion-specific effects", 134, 2011.

[41] Dan Ben-Yaakov et al. "Beyond standard Poisson–Boltzmann theory: ion-specific interactions in aqueoussolutions", 21p. 424106, 2009.

[42] Itamar Borukhov, David Andelman, and Henri Orland. "Adsorption of large ions from an electrolyte solution: a modified Poisson–Boltzmann equation", 46pp. 221–229, 2000.

[43] Guillaume Tresset. "Generalized Poisson-Fermi formalism for investigating size correlation effects with multiple ions", 78p. 061506, 2008.

[44] Bo Li. "Minimization of electrostatic free energy and the Poisson–Boltzmann equation for molecular solvation with implicit solvent", 40pp. 2536–2566, 2009.

have the same finite size, characterized by a uniform parameter a, so that$\theta_j = an_j$ for all j.

A useful framework for incorporating steric effects is the lattice gas model,[43] where ions occupy discrete cells of volume a. The corresponding free-energy functional, which accounts for entropy of mixing, takes the form:[33,43]

$$f(T, \{n_j\}_{j=1}^{J}) = \frac{k_B T}{a} \left(1 - a \sum_{j=1}^{J} n_j\right) \log \left(1 - a \sum_{j=1}^{J} n_j\right) + k_B T \sum_{j=1}^{J} n_j \log a n_j. \quad (2.6.35)$$

Here, the quantity $\theta_{FS} = 1 - a \sum_{j=1}^{J} n_j$ represents the volume fraction of free space, which can also be interpreted as the volume fraction of solvent. Since water molecules are not explicitly modeled, θ_{FS} effectively measures the void space available in the system. The entropy associated with this free volume is given by:

$$\frac{k_B T}{a} \left(1 - a \sum_{j=1}^{J} n_j\right) \log \left(1 - a \sum_{j=1}^{J} n_j\right) ,$$

a term that highlights how steric constraints, due to the finite size of ions, reduce the total entropic contribution to the free energy. As ionic concentration increases, crowding effects limit the spatial freedom of each species, leading to non-trivial deviations from ideal behavior. Thermodynamically, this contribution can be viewed as an implicit correction to the activity coefficients, accounting for excluded volume effects that cause deviations from ideal mixture behavior.[45] In this framework, the entropic part of the chemical potential μ_j^{ent} must now include the effect of finite volume exclusion:

$$\mu_j^{\text{ent}} = k_B T \log \left(\frac{a n_j}{\theta_{\text{FS}}}\right) .$$

In the dilute limit—specifically, when a $\sum_{j=1}^{J} n_j \ll 1$—the steric contribution becomes negligible, and the model recovers the classical ideal mixture formulation.

It is also worth noting that in the standard treatment of an ideal Coulomb gas, the entropic part of the free energy typically includes a term proportional to the ionic concentrations: $-k_B T \sum_j n_j$, as shown in Eq. (2.6.26). However, within the present framework, this ideal entropy term is effectively canceled by an opposing contribution from the excess free energy, allowing us to neglect it in the final expression.

Incorporating both steric effects and electrostatic interactions, the total chemical potential in this model becomes:

$$\mu_j = k_B T \log \left(\frac{a n_j}{\theta_{\text{FS}}}\right) - e z_j \phi ,$$

---

[45] Alan D McNaught, Andrew Wilkinson, et al. *Compendium of chemical terminology*. Vol. 1669. Blackwell Science Oxford, 1997.

and the total free energy of the system is given by

$$\begin{aligned}\Xi = \int_\Omega \chi_{\Omega_s} \frac{k_B T}{a} \theta_{FS} \log \theta_{FS} + \; k_B T \sum_{j=1}^{J} n_j \log a n_j \\ - \int_\Omega \chi_{\Omega_s} \sum_{j=1}^{J} \mu_j n_j + \int_\Omega \left[\rho^f \phi - \frac{\varepsilon}{2} (\nabla \phi)^2 \right] \mathbf{dr} \,. \end{aligned} \tag{2.6.36}$$

At equilibrium, the stationary condition for the free energy variation w.r.t n_j leads to:

$$-\mu_j^{ent} + e z_i \phi + k_B T \log \left(\frac{a n_j}{\theta_{FS}} \right) = 0 \quad \forall j \tag{2.6.37}$$

This yields the equilibrium ion density distribution:[44]

$$n_j = \frac{n_j^b e^{-\dfrac{e z_j \phi}{k_B T}}}{1 + a \sum_{i=1}^{J} n_i^b e^{-\frac{e z_i \phi}{k_B T}}} = \frac{1}{a} \frac{e^{\dfrac{\mu_j}{k_B T}}}{1 + \sum_{i=1}^{J} e^{\frac{\mu_i}{k_B T}}} \,. \tag{2.6.38}$$

Finally, the osmotic pressure in the presence of steric effects is given by:[41,46]

$$P = - \frac{k_B T}{a} \log \left(1 - \sum_{j=1}^{J} a n_j \right) \,. \tag{2.6.39}$$

These expressions illustrate a fundamental departure from ideal-gas-like behavior: as ion concentration increases, steric effects lead to saturation, preventing indefinite accumulation near charged surfaces. Properly accounting for these effects is essential for accurately modeling highly concentrated electrolyte solutions and biological systems where ion crowding plays a crucial role. Notably, in the low-concentration regime where $\sum_j \theta_j \ll 1$, Eqs.(2.6.38) and(2.6.39) reduce to the density and pressure predicted by the classical PBE.

2.6.3 Incorporating Ion-Solvation Effects

A key advantage of this generalized framework is its flexibility in incorporating additional interactions one by one. In the previous section, we considered steric effects, a form of ion-ion interaction. However, another crucial factor in electrolyte solutions is ion solvation: water molecules surrounding ions affect the solvent's polarizability in response to an external electric field generated by fixed molecular charges,

---

[46] Dan Ben-Yaakov et al. "Ion-specific hydration effects: Extending the Poisson-Boltzmann theory", 16pp. 542–550, 2011.

as schematically illustrated in Fig. 2.2c. Experimental studies confirm that ion concentration influences the dielectric constant of the solvent.[47,48] Various modeling approaches have been proposed to account for this dependence,[40,49] among which the Bruggeman equation is a well-established method for estimating the effective dielectric properties of heterogeneous media.[14,43]

To extend our free energy formulation and incorporate these effects, we recall the definition of the ion volume fraction from (2.5.6), but in this case we relax the assumption that all ions have the same size. Notably, the solvent can be treated as an additional species with zero valence:

$$\theta_w(\mathbf{r}) = 1 - \sum_{j=1}^{J} \theta_j \quad \text{and} \quad n_w = \frac{1}{a_w}\left(1 - \sum_{j=1}^{J} a_j n_j\right) \tag{2.6.40}$$

where θ_w and a_w denote the volume fraction and effective volume of water molecules, respectively. Using this formulation, the local dielectric constant $\varepsilon(\mathbf{r})$ follows the Bruggeman equation:

$$\theta_w(\mathbf{r})\frac{\varepsilon_w - \varepsilon(\mathbf{r})}{\varepsilon_w + (d-1)\varepsilon(\mathbf{r})} + \sum_{j=1}^{J} \theta_j \frac{\varepsilon_j - \varepsilon(\mathbf{r})}{\varepsilon_j + (d-1)\varepsilon(\mathbf{r})} = 0\ . \tag{2.6.41}$$

Here, ε_j is the dielectric coefficient of the j-th ion species in the solvent, and d is the system's dimensionality, which is $d = 3$ in our case.
As a result, the free energy density becomes:

$$\begin{aligned} f(T, \{n_j\}_{j=1}^{J}) &= k_B T n_w \left(\log a_w n_w - 1\right) + k_B T \sum_{j=1}^{J} n_j \left[\log a_j n_j - 1\right] \\ &= \frac{k_B T}{a_w}\theta_w \left[\log \theta_w - 1\right] + \ k_B T \sum_{j=1}^{J} n_j \left[\log \theta_j - 1\right]\ . \end{aligned} \tag{2.6.42}$$

From this, the total free energy of the system is:

---

[47] Yan-Zhen Wei and S Sridhar. "Dielectric spectroscopy up to 20 GHz of LiCl/H2O solutions", 92pp. 923–928, 1990.

[48] Richard Buchner, Glenn T Hefter, and Josef Barthel. "Dielectric relaxation of aqueous NaF and KF solutions", 90pp. 2475–2479, 1994.

[49] Nir Gavish and Keith Promislow. "Dependence of the dielectric constant of electrolyte solutions on ionic concentration: A microfield approach", 94p. 012611, 2016.

$$
\begin{aligned}
\Xi = &\int_\Omega \chi_{\Omega_s} \frac{k_B T}{a_w} \theta_w \left[\log \theta_w - 1\right] \\
&+ \int_\Omega \chi_{\Omega_s} \left[k_B T \sum_{j=1}^{J} n_j \left(\log \theta_j - 1 - \mu_j^{ent} + e z_j \phi \right) \right] \\
&+ \int_\Omega \left[\rho^f \phi - \frac{\varepsilon}{2} (\nabla \phi)^2 \right] \mathrm{d}\mathbf{r}
\end{aligned}
\tag{2.6.43}
$$

Minimizing the total free energy w.r.t. n_j gives the equilibrium condition for ion densities:

$$
0 = k_B T \left[\log \theta_j - \frac{a_j}{a_w} \log \theta_w \right] - \mu_j^{ent} + e z_j \phi - \frac{1}{2} \frac{\partial \varepsilon}{\partial n_j} (\nabla \phi)^2 \qquad \forall j \tag{2.6.44}
$$

Unlike in the previous models, for this problem we cannot express the equilibrium density explicitly. Instead, the governing equations for electrostatic potential and ion concentrations at equilibrium are:

$$
\begin{cases}
-\nabla \cdot (\varepsilon(\{n_i\}) \nabla \phi) = \rho^f + \sum_{j=1}^{J} e z_j n_j \\
k_B T \left[\log \theta_j - \dfrac{a_j}{a_w} \log \theta_w \right] - \mu_j^{ent} + e z_j \phi - \dfrac{1}{2} \dfrac{\partial \varepsilon}{\partial n_j} (\nabla \phi)^2 = 0 \quad \forall j \\
\theta_w(\mathbf{r}) \dfrac{\varepsilon_w - \varepsilon(\mathbf{r})}{\varepsilon_w + (d-1)\varepsilon(\mathbf{r})} + \sum_{j=1}^{J} \theta_j \dfrac{\varepsilon_j - \varepsilon(\mathbf{r})}{\varepsilon_j + (d-1)\varepsilon(\mathbf{r})} = 0
\end{cases} . \tag{2.6.45}
$$

This formulation self-consistently captures how ion concentration variations alter the solvent's dielectric properties, integrating both electrostatic and thermodynamic effects. While this approach enhances the physical realism of electrolyte models, solving these equations for realistic conditions remains computationally challenging.[14]

Chapter 3

Analytical Results for LPBE

In this chapter, we focus on the linearized Poisson-Boltzmann equation (LPBE), a fundamental approximation of the full non-linear Poisson-Boltzmann equation (PBE). Consider an open bounded domain $\Omega = \Omega_m \cup \Omega_s \cup \Gamma$, where Ω_m represents the region of space occupied by the solute (typically a molecule), Ω_s denotes the solvent region, and Γ is the closed surface separating them, as in the schematic representation in Fig. 3.1. As derived in Sec. 2.5, the LPBE is:

$$\nabla \cdot (\varepsilon(\mathbf{r}) \nabla \phi) = -\sum_{i=1}^{N} q_i \delta(\mathbf{r} - \mathbf{r}_i) + c(\mathbf{r}) \phi(\mathbf{r}) \qquad \mathbf{r} \in \Omega \,, \tag{3.0.1}$$

where $c(\mathbf{r}) = \varepsilon_s k_D^2 \chi \Omega_s(\mathbf{r})$, $\chi_{\Omega_s}(\mathbf{r})$ is the characteristic function of the solvent volume, and $\varepsilon(\mathbf{r})$ is the piecewise constant dielectric function where $\varepsilon(\mathbf{r}) = \varepsilon_m$ if $\mathbf{r} \in \Omega_m$ and $\varepsilon(\mathbf{r}) = \varepsilon_s$ if $\mathbf{r} \in \Omega_s$.

The LPBE arises in electrostatics when considering weak potential fields, allowing for significant analytical simplifications while retaining essential physical insights. It admits analytical solutions in specific symmetrical scenarios.[1–6] One such case is the problem of a charged sphere in an electrolyte,[1] which serves as a well-established benchmark in electrostatic modeling. By exploiting the spherical symmetry, the governing equations can be reduced to ordinary differential equations, permitting exact solutions under appropriate boundary conditions.

In the following sections, we reformulate the solution of the LPBE in a way that allows the electrostatic potential, and consequently, the total energy, to be naturally

---

[1] John G Kirkwood. "Theory of solutions of molecules containing widely separated charges with special application to zwitterions", 2pp. 351–361, 1934.

[2] Huan-Xiang Zhou and Xiaodong Pang. "Electrostatic interactions in protein structure, folding, binding, and condensation", 118pp. 1691–1741, 2018.

[3] Michael E Fisher, Yan Levin, and Xiaojun Li. "The interaction of ions in an ionic medium", 101pp. 2273–2282, 1994.

[4] OI Obolensky, TP Doerr, and Yi-Kuo Yu. "Rigorous treatment of pairwise and many-body electrostatic interactions among dielectric spheres at the Debye–Hückel level", 44pp. 1–18, 2021.

[5] S. V. Siryk et al. "Charged dielectric spheres interacting in electrolytic solution: a linearized Poisson-Boltzmann equation model", 155p. 114114, 2021.

[6] S. Siryk and W. Rocchia. "Arbitrary-Shape Dielectric Particles Interacting in the Linearized Poisson-Boltzmann Framework: An Analytical Treatment", 126pp. 10400–10426, 2022.

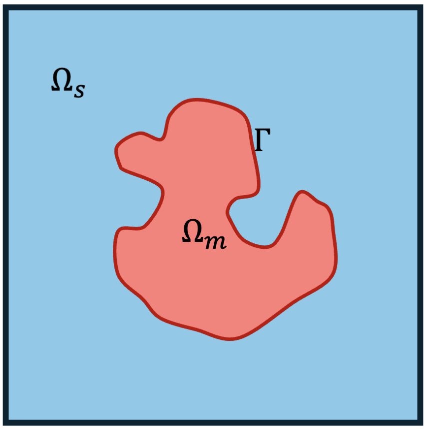

FIGURE 3.1: Two-dimensional schematic representation of the system.

partitioned into three physically meaningful contributions. This formulation also has a practical advantage: it avoids the explicit calculation of self-energies and the volumetric contribution of ions to the energy, which are often computationally demanding. We then derive the analytical solution for the classic one-sphere problem and extend it to the case of multiple non-overlapping spheres. The latter is particularly interesting because it breaks spherical symmetry, making it not only an analytical result but also a valuable non-symmetric benchmark for testing LPBE solvers. These comparisons serve as essential references for assessing the accuracy and performance of computational approaches in electrostatic modeling.

3.1 Total free energy for LPBE

The total free energy of a molecule in an electrolytic solvent, denoted as ΔG, is given in Eq. (2.6.15):

$$\Delta G = \int_\Omega \left[\chi_{\Omega_s} P + \rho^f \phi - \frac{1}{2} \mathbf{D} \cdot \mathbf{E} \right] \mathrm{d}\mathbf{r} - G_0 \,, \tag{3.1.1}$$

where we neglect the surface term, and G_0 is the reference energy corresponding to the potential $\phi = 0$.

For the LPBE, this energy can be written in a more compact form.[7] From Maxwell's equations, we have:

$$\frac{1}{2} \int_\Omega \mathbf{D} \cdot \mathbf{E} \mathrm{d}\mathbf{r} = \frac{1}{2} \int_\Omega \rho(\mathbf{r}) \phi(\mathbf{r}) \mathrm{d}\mathbf{r} \,, \tag{3.1.2}$$

---

[7] Kim A Sharp and Barry Honig. "Calculating total electrostatic energies with the nonlinear Poisson-Boltzmann equation", 94pp. 7684–7692, 1990.

which leads to the expression:

$$\Delta G = \int_{\Omega} \left[\frac{1}{2}\rho^f \phi - \frac{1}{2}\rho^s \phi - \chi_{\Omega_s} P \right] \mathrm{d}\mathbf{r} - G_0 \,. \tag{3.1.3}$$

As discussed in Sec. 2.6.1, for the full PBE, the pressure term takes the form $P = k_B T \sum_{j=1}^{J} n_j^b \exp\left(-\frac{z_j e \phi}{k_B T}\right)$, and the reference energy is $G_0 = k_B T \sum_{j=1}^{J} n_j^b$. In the case of weakly charged systems, and under the assumption of electroneutrality, the free energy can be approximated as:

$$\begin{aligned} \Delta G &= \int_{\Omega} \left[\frac{1}{2}\rho^f \phi - \frac{1}{2}\rho^s \phi - \chi_{\Omega_s} k_B T \sum_{j=1}^{J} n_j^b \left[\exp\left\{ -\frac{z_j e \phi}{k_B T} \right\} - 1 \right] \right] \mathrm{d}\mathbf{r} \\ &\approx \int_{\Omega} \left[\frac{1}{2}\rho^f \phi - \frac{1}{2}\rho^s \phi - \chi_{\Omega_s} k_B T \sum_{j=1}^{J} n_j^b \left(\frac{z_j e \phi}{k_B T} \right)^2 \right] \mathrm{d}\mathbf{r} \\ &= \int_{\Omega} \left[\frac{1}{2}\rho^f \phi - \frac{1}{2}\rho^s \phi - c(\mathbf{r})\phi^2 \right] \mathrm{d}\mathbf{r} \end{aligned} \tag{3.1.4}$$

Using Eq. (2.5.13), the total free energy for the LPBE becomes:

$$\Delta G = \frac{1}{2} \int_{\Omega} \rho^f(\mathbf{r}) \phi(\mathbf{r}) \mathrm{d}\mathbf{r} = \frac{1}{2} \sum_{i=1}^{N} q_i \phi(\mathbf{r}_i) \,, \tag{3.1.5}$$

where $\phi(\mathbf{r})$ is the total electrostatic potential evaluated at the position of each fixed charge q_i, excluding the singular self-interaction. For the LPBE, the total free energy corresponds to the electrostatic energy of placing N fixed charges in the potential ϕ, which includes contributions from both the fixed charges and the mobile ions.
Equation (3.1.5) can be further decomposed into three distinct contributions:[8]

- **Coulombic potential** ϕ_{coul}, which is analytically computable.
- **Polarization potential** ϕ_{pol}, arising from dielectric discontinuities at the MS.
- **Ionic potential** ϕ_{ion}, induced by mobile counterions in the solvent.

Both ϕ_{coul} and ϕ_{ion} account for the screening due to the continuum medium in which their sources are located.
This decomposition leads to the following partitioned energy expression:

$$\Delta G = \frac{1}{2} \sum_{i=1}^{N} q_i \left(\phi_{coul}(\mathbf{r}_i) + \phi_{pol}(\mathbf{r}_i) + \phi_{ion}(\mathbf{r}_i) \right) \,. \tag{3.1.6}$$

---

[8] Walter Rocchia, Emil Alexov, and Barry Honig. "Extending the applicability of the nonlinear Poisson-Boltzmann equation: multiple dielectric constants and multivalent ions", 105pp. 6507–6514, 2001.

This partitioning provides a practical advantage: the Coulombic term can be evaluated analytically while avoiding the self-energy contribution, and the polarization term can be computed separately.[8]

Regarding the ionic term, its source is the local ionic imbalance, which extends throughout the solvent until the potential vanishes. Since directly integrating this term over the entire volume is computationally prohibitive, it is often circumvented. Instead, the ionic energy contribution is typically estimated by computing the difference in the so-called grid energy between two successive runs—one at zero ionic strength and the other at the actual ionic strength. The grid energy is defined as half the sum of the fixed charges mapped onto the grid points times the numerical potential at those points.

In the following sections, we develop an analytical method to compute the ionic potential using only information from the molecular surface (MS), thereby eliminating the need for volume integrations over the solvent or grid energy subtractions.

3.2 Electrostatic Potential via Green's Identities

The electrostatic potential in biomolecular systems is naturally divided into distinct regions, the solute and the surrounding solvent, each governed by different physical properties. A rigorous and insightful way to achieve the partitioning in Eq. (3.1.6) is through Green's identities, which provide two complementary expressions: one tailored for evaluating the potential within the solute and another for computing it in the solvent.

This approach is not merely a theoretical convenience; it plays a crucial role in practical energy calculations, where accurate partitioning is essential for obtaining reliable solvation energies and interaction forces. Moreover, it offers a powerful means of assessing the fidelity of various boundary conditions commonly employed in numerical solvers. By decomposing the potential in this manner, we can systematically examine how different approximations influence the accuracy of electrostatic models and refine them accordingly.

In the following discussion, we delve into these formulations, exploring their derivation, significance, and implications for computational electrostatics.

3.2.1 Internal Electrostatic Potential via Green's Identities

We consider the potential evaluated at a point $\mathbf{r}$ belonging to a volume region Ω_m enclosed in a surface Γ. This region, that in the PB case represents the solute, is surrounded by the electrolytic solution, and contains the free charge distribution ρ^f. We begin by expressing the LPBE (2.5.15) in operator form:

$$L[\phi] = \rho^f \ , \tag{3.2.1}$$

where the linear operator L is defined as:

$$L = -\nabla \cdot (\varepsilon(\mathbf{r})\nabla(\cdot)) + c(\mathbf{r})(\cdot) \qquad \mathbf{r} \in D\,. \tag{3.2.2}$$

A natural strategy to analyze this equation is to employ the second Green's identity, which has been instrumental in deriving integral representations of solutions in electrostatics. However, a direct application is hindered by the discontinuity of the dielectric function $\varepsilon(\mathbf{r})$ at the MS Γ. Since $\varepsilon(\mathbf{r})$ is piecewise constant, its gradient is ill-defined in the classical sense but can be meaningfully treated in a distributional framework.

To formalize this, we introduce an approximant function $\varepsilon_d(\mathbf{r})$, which smoothly transitions between the internal (ε_m) and external (ε_s) dielectric values over a narrow layer of thickness d. This function converges to a step function with the discontinuity located on Γ, as a limit for $d \to 0^+$, using an error function representation:

$$\varepsilon_d(\mathbf{r}) = \frac{\varepsilon_s - \varepsilon_m}{2}\left[\operatorname{erf}\left(\frac{u(\mathbf{r})}{d}\right) + 1\right] + \varepsilon_m\,. \tag{3.2.3}$$

For the definition of u, we consider for each $\mathbf{r}$ near the surface, its orthogonal projection on Γ, namely $\mathbf{r}_\Gamma \in \Gamma$, and its direction $\mathbf{n}(\mathbf{r}_\Gamma)$. We define u as the oriented distance from the surface itself:

$$u(\mathbf{r}) = (\mathbf{r} - \mathbf{r}_\Gamma) \cdot \mathbf{n}(\mathbf{r}_\Gamma)\,. \tag{3.2.4}$$

In this approximation, the midpoint value at the transition layer, corresponding to $u = 0$, is given by the arithmetic mean:

$$\varepsilon_d(u = 0) = \bar{\varepsilon} = \frac{\varepsilon_m + \varepsilon_s}{2}\,. \tag{3.2.5}$$

A schematic representation of this transition is shown in Fig. 3.2.

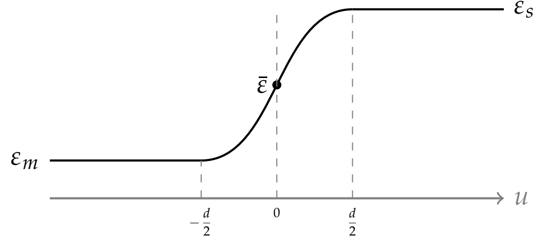

FIGURE 3.2: Schematic representation of the approximated variation of ε.

It is interesting to note that numerical FEM-BEM-coupled modelling with MS represented as a continuous interface (similarly to (3.2.3) with non-zero d) and the corresponding impact of such diffused interfaces on solvation and binding energy, were very recently treated in Ref. [9]. In addition to the error function erf, the work [9] has benchmarked other sigmoidal functions (like tanh) to couple the internal and external regions.

Since ε_d varies smoothly across the interface, we can compute its gradient, which is aligned with the normal at the surface and takes the following form:

$$\nabla \varepsilon_d(\mathbf{r}) = \frac{\mathrm{d}\varepsilon_d(u)}{\mathrm{d}u} \nabla u = (\varepsilon_s - \varepsilon_m) \mathcal{N}(0, \frac{d^2}{2}) \mathbf{n}(\mathbf{r}_\Gamma) \tag{3.2.6}$$

(here the symbol $\mathcal{N}(0, d^2/2)$ indicates the normal distribution density function with zero mean and variance $d^2/2$).
In the sharp-interface limit $d \to 0$, this expression converges to:

$$\nabla \varepsilon(\mathbf{r}) = (\varepsilon_s - \varepsilon_m) \delta((\mathbf{r} - \mathbf{r}_\Gamma) \cdot \mathbf{n}(\mathbf{r}_\Gamma)) \mathbf{n}(\mathbf{r}_\Gamma) \qquad \mathbf{r}_\Gamma \in \Gamma\,, \tag{3.2.7}$$

where $\delta(\cdot)$ is the Dirac delta distribution, enforcing localization at the interface. This reformulation allows us to proceed with a modified Green's identity approach, assuming the interchange of limits and integral operations holds.

Similarly to what is done in the case of the second Green's identity, we consider the following identity:

$$\int_\Omega \{L[v]w - L[w]v\} \, \mathrm{d}V = \int_\Omega \nabla \cdot [\varepsilon(\mathbf{r}) \, (v \nabla w - w \nabla v)] \, \mathrm{d}V \,. \tag{3.2.8}$$

where w and v are suitable test functions, and $\tilde{\mathbf{r}}$ is the integration variable.
Let us now instantiate Eq. (3.2.8) by choosing $\Omega = \Omega_m$ (the molecular region) and select the functions:

- $w(\tilde{\mathbf{r}}) = \phi(\tilde{\mathbf{r}})$ as the solution of Eq. (3.2.1),
- $v(\tilde{\mathbf{r}}) = \dfrac{q}{4\pi\varepsilon_m \|\tilde{\mathbf{r}} - \mathbf{r}\|}$, the fundamental solution of Laplace's equation centered at $\mathbf{r} \in \Omega_m$ in a homogeneous medium with permittivity ε_m.

Substituting these into Eq. (3.2.8) yields:

---

[9] Mauricio Guerrero-Montero, Michał Bosy, and Christopher D Cooper. "Some Challenges of Diffused Interfaces in Implicit-Solvent Models". *Journal of Computational Chemistry* 46, e70036, 2025..

$$
\begin{aligned}
&\int_{\Omega_m} \{L[v(\tilde{\mathbf{r}})]\phi(\tilde{\mathbf{r}}) - L[\phi(\tilde{\mathbf{r}})]v(\tilde{\mathbf{r}})\}\, \mathrm{d}V = \\
&\quad = \int_{\Omega_m} q\phi(\tilde{\mathbf{r}}) \left[\frac{c(\tilde{\mathbf{r}})}{4\pi\varepsilon_m \|\tilde{\mathbf{r}} - \mathbf{r}\|} + \frac{\varepsilon(\tilde{\mathbf{r}})}{\varepsilon_m} \delta(\tilde{\mathbf{r}} - \mathbf{r}) + \frac{\nabla(\varepsilon(\tilde{\mathbf{r}})) \cdot (\tilde{\mathbf{r}} - \mathbf{r})}{4\pi\varepsilon_m \|\tilde{\mathbf{r}} - \mathbf{r}\|^3} \right] \mathrm{d}V + \\
&\quad - \int_{\Omega_m} \frac{\rho^f q}{4\pi\varepsilon_m \|\tilde{\mathbf{r}} - \mathbf{r}\|} \mathrm{d}V \, .
\end{aligned} \tag{3.2.9}
$$

In Ω_m, we have $c(\tilde{\mathbf{r}}) = 0$ and uniform permittivity $\varepsilon(\mathbf{r}) = \varepsilon_m$. Under these conditions, Eq. (3.2.9) simplifies to:

$$
\begin{aligned}
&\int_{\Omega_m} \{L[v(\tilde{\mathbf{r}})]\phi(\tilde{\mathbf{r}}) - L[\phi(\tilde{\mathbf{r}})]v(\tilde{\mathbf{r}})\} \mathrm{d}V = \\
&\quad = q\phi(\mathbf{r}) + \frac{q}{4\pi\varepsilon_m} \int_{\Omega_m} \phi(\tilde{\mathbf{r}}) \frac{\nabla(\varepsilon(\tilde{\mathbf{r}})) \cdot (\tilde{\mathbf{r}} - \mathbf{r})}{\|\tilde{\mathbf{r}} - \mathbf{r}\|^3} \mathrm{d}V - \frac{q}{4\pi\varepsilon_m} \int_{\Omega_m} \frac{\rho^f}{\|\tilde{\mathbf{r}} - \mathbf{r}\|} \mathrm{d}V \\
&\quad = q\phi(\mathbf{r}) + \frac{q}{4\pi\varepsilon_m} \int_{\Omega_m} \phi(\tilde{\mathbf{r}}) (\varepsilon_s - \varepsilon_m) \frac{\delta((\mathbf{r} - \mathbf{r}_\Gamma) \cdot \mathbf{n}(\mathbf{r}_\Gamma)) \mathbf{n}(\mathbf{r}_\Gamma) \cdot (\tilde{\mathbf{r}} - \mathbf{r})}{\|\tilde{\mathbf{r}} - \mathbf{r}\|^3} \mathrm{d}V + \\
&\qquad - \frac{q}{4\pi\varepsilon_m} \int_{\Omega_m} \frac{\rho^f}{\|\tilde{\mathbf{r}} - \mathbf{r}\|} \mathrm{d}V \, .
\end{aligned} \tag{3.2.10}
$$

A key step in simplifying this expression relies on the *single-layer* property of the Dirac delta function. Moreover, along the limit for $d \to 0$ process, the integral is evaluated only on the internal half of the layer enclosing the surface where ε_d is changing. As a result, we can transform the volume integral into a surface integral:

$$
\begin{aligned}
&\int_{\Omega_m} \phi(\tilde{\mathbf{r}}) (\varepsilon_s - \varepsilon_m) \frac{\delta((\mathbf{r} - \mathbf{r}_\Gamma) \cdot \mathbf{n}(\mathbf{r}_\Gamma)) \mathbf{n}(\mathbf{r}_\Gamma) \cdot (\tilde{\mathbf{r}} - \mathbf{r})}{\|\tilde{\mathbf{r}} - \mathbf{r}\|^3} \mathrm{d}V = \\
&\qquad = \frac{\varepsilon_s - \varepsilon_m}{2} \int_{\partial\Omega_m} \phi(\tilde{\mathbf{r}}) \frac{(\tilde{\mathbf{r}} - \mathbf{r}) \cdot \mathbf{n}(\tilde{\mathbf{r}})}{\|\tilde{\mathbf{r}} - \mathbf{r}\|^3} \mathrm{d}S \, .
\end{aligned} \tag{3.2.11}
$$

In the present case, $\partial\Omega_m \equiv \Gamma$ and $\mathbf{n}$ denotes the unit vector orthogonal to Γ and oriented in the outward direction.

Next, we turn our attention to the right-hand side (RHS) of Eq. (3.2.8) for our specific setting. This part of the derivation involves applying the divergence theorem to transform volume integrals into surface integrals, a step that is central to connecting the behavior of the potential within Ω_m to its boundary conditions on Γ. The RHS of Eq. (3.2.8) can be written as:

$$\begin{aligned}
&\int_{\Omega_m} \nabla\cdot[\varepsilon(\tilde{\mathbf{r}})v(\tilde{\mathbf{r}})\nabla\phi(\tilde{\mathbf{r}}) - \varepsilon(\tilde{\mathbf{r}})\phi(\tilde{\mathbf{r}})\nabla v(\tilde{\mathbf{r}})]\mathrm{d}V = \\
&\qquad = -\int_{\Omega_m} \nabla\cdot[v(\tilde{\mathbf{r}})\mathbf{D}(\tilde{\mathbf{r}})]\mathrm{d}V + \int_{\Omega_m} \nabla\cdot[\varepsilon(\tilde{\mathbf{r}})\phi(\tilde{\mathbf{r}})\frac{q(\tilde{\mathbf{r}}-\mathbf{r})}{4\pi\varepsilon_m\|\tilde{\mathbf{r}}-\mathbf{r}\|^3}]\mathrm{d}V \\
&\qquad = -q\int_{\Gamma} \frac{\mathbf{D}(\tilde{\mathbf{r}})\cdot\mathbf{n}(\tilde{\mathbf{r}})}{4\pi\varepsilon_m\|\tilde{\mathbf{r}}-\mathbf{r}\|}\mathrm{d}S + q\int_{\Gamma} \bar{\varepsilon}\phi(\tilde{\mathbf{r}})\frac{(\tilde{\mathbf{r}}-\mathbf{r})\cdot\mathbf{n}(\tilde{\mathbf{r}})}{4\pi\varepsilon_m\|\tilde{\mathbf{r}}-\mathbf{r}\|^3}\mathrm{d}S\,.
\end{aligned}\tag{3.2.12}$$

Here, $\mathbf{D}$ is the electric displacement vector field, and $(\nabla\cdot)_n = \nabla(\cdot)\cdot\mathbf{n}$ denotes the normal component of the divergence. The application of the divergence theorem is particularly straightforward in the first integral involving $\mathbf{D}$, as its normal component is continuous across the interface, while the contribution to the integral given by the discontinuous tangential component is nullified by the scalar product with $\mathbf{n}$. In contrast, the second integral requires careful handling of the dielectric function ε_d, particularly in the limit as the transition layer thickness $d \to 0^+$. This step underscores the importance of the distributional framework introduced earlier, which allows us to rigorously treat the discontinuity in Γ.
By combining the results from (3.2.10) and (3.2.12), we can express the electrostatic potential in any point of Ω_m as follows:

$$\begin{aligned}
\phi(\mathbf{r}) = \int_{\Omega_m} \frac{\rho^f}{4\pi\varepsilon_m\|\tilde{\mathbf{r}}-\mathbf{r}\|}\mathrm{d}V - \frac{\varepsilon_s-\varepsilon_m}{2}\int_{\Gamma}\phi(\tilde{\mathbf{r}})\frac{(\tilde{\mathbf{r}}-\mathbf{r})\cdot\mathbf{n}(\tilde{\mathbf{r}})}{4\pi\varepsilon_m\|\tilde{\mathbf{r}}-\mathbf{r}\|^3}\mathrm{d}S+ \\
-\int_{\Gamma}\frac{\mathbf{D}(\tilde{\mathbf{r}})\cdot\mathbf{n}(\tilde{\mathbf{r}})}{4\pi\varepsilon_m\|\tilde{\mathbf{r}}-\mathbf{r}\|}\mathrm{d}S + \int_{\Gamma}\bar{\varepsilon}\phi(\tilde{\mathbf{r}})\frac{(\tilde{\mathbf{r}}-\mathbf{r})\cdot\mathbf{n}(\tilde{\mathbf{r}})}{4\pi\varepsilon_m\|\tilde{\mathbf{r}}-\mathbf{r}\|^3}\mathrm{d}S
\end{aligned}$$

which yields:

$$\phi(\mathbf{r}) = \int_{\Omega_m} \frac{\rho^f}{4\pi\varepsilon_m\|\tilde{\mathbf{r}}-\mathbf{r}\|}\mathrm{d}V - \int_{\Gamma}\frac{\mathbf{D}(\tilde{\mathbf{r}})\cdot\mathbf{n}(\tilde{\mathbf{r}})}{4\pi\varepsilon_m\|\tilde{\mathbf{r}}-\mathbf{r}\|}\mathrm{d}S + \int_{\Gamma}\phi(\tilde{\mathbf{r}})\frac{(\tilde{\mathbf{r}}-\mathbf{r})\cdot\mathbf{n}(\tilde{\mathbf{r}})}{4\pi\|\tilde{\mathbf{r}}-\mathbf{r}\|^3}\mathrm{d}S \quad \forall\mathbf{r}\in\Omega_m\,. \tag{3.2.13}$$

Eq (3.2.13) provides a complete description of the electrostatic potential within the solute, accounting for both internal charge distributions and mobile ion density.

3.2.2 Partitioning of Internal Electrostatic Potential

Having derived an expression for the electrostatic potential inside the molecule, we now turn our attention to the physical interpretation of its components. Eq. (3.2.13) provides a natural partitioning of the potential into distinct contributions, each with a clear physical meaning. This partitioning aligns with the energy decomposition outlined in Eq. (3.1.6), offering deeper insight into the electrostatic interactions within the system.

Coulombic Potential

The first term on the RHS of Eq. (3.2.13) represents the electrostatic potential generated by the fixed charge distribution ρ^f in a homogeneous medium with permittivity ε_m. This is the familiar Coulombic potential, ϕ_{coul}, which describes the direct contribution of the free charges to the electrostatic field within the solute. Mathematically, it is given by:

$$\phi_{coul} = \int_{\Omega_m} \frac{\rho^f}{4\pi\varepsilon_m \|\tilde{\mathbf{r}} - \mathbf{r}\|} \mathrm{d}V \ . \tag{3.2.14}$$

This term is the simplest and most intuitive component of the potential, capturing the classical electrostatic interaction between charges in a uniform dielectric environment.

What makes this term particularly appealing is its computational tractability. Unlike more complex contributions to the potential, ϕ_{coul} can be calculated analytically, bypassing the need for numerical approximations. Furthermore, this formulation inherently avoids the singularities associated with self-energy contributions, which arise when evaluating the potential at the location of a point charge, making it both physically meaningful and computationally robust.

Polarization Potential

In the continuum electrostatic model, the polarization of the dielectric medium at the interface Γ gives rise to a surface polarization charge. This charge distribution, denoted $\sigma_{pol}(\mathbf{r})$, arises from the discontinuity in the polarization vector across the boundary between the solute and the solvent. Mathematically, it is expressed as:

$$\sigma_{pol}(\mathbf{r}) = -(\mathbf{P}_2(\mathbf{r}) - \mathbf{P}_1(\mathbf{r})) \cdot \mathbf{n}_{21}(\mathbf{r}) \quad \mathbf{r} \in \Gamma \ , \tag{3.2.15}$$

where $\mathbf{n}_{21}$ is the unit normal pointing from the molecule (region 1) to the solvent (region 2), and $\mathbf{P}_1(\mathbf{r})$ and $\mathbf{P}_2(\mathbf{r})$ are the polarization vectors in the molecule and in the solvent respectively, evaluated at $\mathbf{r} \in \Gamma$. For our system, the surface polarization charge can be rewritten in terms of the electric displacement field $\mathbf{D}$ and the dielectric constants ε_m and ε_s:

$$\sigma_{pol}(\mathbf{r}) = \varepsilon_0 \left(\frac{1}{\varepsilon_s} - \frac{1}{\varepsilon_m} \right) \mathbf{D}(\mathbf{r}) \cdot \mathbf{n}(\mathbf{r}) \qquad \mathbf{r} \in \Gamma \ , \tag{3.2.16}$$

where $\mathbf{n}$ is the outward unit normal from the molecule. This expression highlights how the polarization charge depends on the dielectric contrast between the solute and solvent. The term $\left(\frac{1}{\varepsilon_s} - \frac{1}{\varepsilon_m}\right)$ quantifies the dielectric mismatch, which drives the accumulation of polarization charge at the interface.

The potential generated by this surface polarization charge, denoted ϕ_{pol}, is given by:

$$\begin{aligned}\phi_{pol}(\mathbf{r}) &= \int_\Gamma \frac{\sigma_{pol}(\tilde{\mathbf{r}})}{4\pi\varepsilon_0\|\tilde{\mathbf{r}} - \mathbf{r}\|} \mathrm{d}S = \\ &= \left(\frac{1}{\varepsilon_s} - \frac{1}{\varepsilon_m}\right) \int_\Gamma \frac{\mathbf{D}(\tilde{\mathbf{r}}) \cdot \mathbf{n}(\tilde{\mathbf{r}})}{4\pi\|\tilde{\mathbf{r}} - \mathbf{r}\|} \mathrm{d}S \;.\end{aligned} \tag{3.2.17}$$

This term represents the contribution of the polarization charge to the electrostatic potential within the solute. It captures the effect of the dielectric boundary on the potential, reflecting how the discontinuity in polarization at the interface modifies the electric field.

Considering this term, we can rewrite the potential in Eq.(3.2.13) to make the polarization term more explicit:

$$\begin{aligned}\phi(\mathbf{r}) &= \phi_{coul}(\mathbf{r}) + \left(\frac{1}{\varepsilon_s} - \frac{1}{\varepsilon_m}\right) \int_\Gamma \frac{\mathbf{D}(\tilde{\mathbf{r}}) \cdot \mathbf{n}(\tilde{\mathbf{r}})}{4\pi\|\tilde{\mathbf{r}} - \mathbf{r}\|} \mathrm{d}S + \\ &\quad + \int_\Gamma \phi(\tilde{\mathbf{r}}) \frac{(\tilde{\mathbf{r}} - \mathbf{r}) \cdot \mathbf{n}(\tilde{\mathbf{r}})}{4\pi\|\tilde{\mathbf{r}} - \mathbf{r}\|^3} \mathrm{d}S - \frac{1}{\varepsilon_s} \int_\Gamma \frac{\mathbf{D}(\tilde{\mathbf{r}}) \cdot \mathbf{n}(\tilde{\mathbf{r}})}{4\pi\|\tilde{\mathbf{r}} - \mathbf{r}\|} \mathrm{d}S \\ &= \phi_{coul}(\mathbf{r}) + \phi_{pol}(\mathbf{r}) + \int_\Gamma \phi(\tilde{\mathbf{r}}) \frac{(\tilde{\mathbf{r}} - \mathbf{r}) \cdot \mathbf{n}(\tilde{\mathbf{r}})}{4\pi\|\tilde{\mathbf{r}} - \mathbf{r}\|^3} \mathrm{d}S - \frac{1}{\varepsilon_s} \int_\Gamma \frac{\mathbf{D}(\tilde{\mathbf{r}}) \cdot \mathbf{n}(\tilde{\mathbf{r}})}{4\pi\|\tilde{\mathbf{r}} - \mathbf{r}\|} \mathrm{d}S\end{aligned} \tag{3.2.18}$$

for all $\mathbf{r} \in \Omega_m$.

Ionic Potential: from volume to surface formulation

When comparing Eq. (3.2.18) with Eq. (3.1.6), it becomes clear that the sum of the last two terms corresponds to the potential due to the ionic charge density in the solution. Here, we explicitly derive this term, transforming a volumetric integral over the solvent domain into a more tractable surface integral. This transformation not only simplifies the computational effort but also provides deeper insight into the role of the ionic charge distribution in shaping the electrostatic potential.

Let us revisit the previous derivation of the potential, this time under the assumption that the domain of interest is restricted to $\Omega = \Omega_s$. In this region, the free charge density vanishes, i.e., $\rho^f(\tilde{\mathbf{r}}) = 0$, while the ionic concentration $c(\tilde{\mathbf{r}})$ remains nonzero (except possibly in the Stern layer). In this case, we choose as a test function

$$v(\tilde{\mathbf{r}}) = \frac{q}{4\pi\varepsilon_s\|\tilde{\mathbf{r}} - \mathbf{r}\|} \;, \tag{3.2.19}$$

where $\mathbf{r} \in \Omega_m$. This choice is particularly insightful, as it mirrors the electrostatic potential of a point charge in a medium with permittivity ε_s. Applying Green's second identity to the governing equation, we arrive at an expression for the LHS of Eq. (3.2.8):

$$\begin{aligned}\int_{\Omega_s} \{L[v(\tilde{\mathbf{r}})]\phi(\tilde{\mathbf{r}}) - L[\phi(\tilde{\mathbf{r}})]v(\tilde{\mathbf{r}})\}\,\mathrm{d}V &= \\ = \int_{\Omega_s} \frac{q\phi(\tilde{\mathbf{r}})}{4\pi\varepsilon_s}\left[\frac{c(\tilde{\mathbf{r}})}{\|\tilde{\mathbf{r}}-\mathbf{r}\|} + \frac{\nabla\varepsilon(\tilde{\mathbf{r}})\cdot(\tilde{\mathbf{r}}-\mathbf{r})}{\|\tilde{\mathbf{r}}-\mathbf{r}\|^3}\right]\mathrm{d}V\,. \end{aligned} \tag{3.2.20}$$

With this choice of the test function v, the RHS of Eq (3.2.8) becomes:

$$\begin{aligned}\int_{\Omega_s} \nabla\cdot[\varepsilon(\tilde{\mathbf{r}})v(\tilde{\mathbf{r}})\nabla\phi(\tilde{\mathbf{r}}) - \varepsilon(\tilde{\mathbf{r}})\phi(\tilde{\mathbf{r}})\nabla v(\tilde{\mathbf{r}})]\mathrm{d}V &= \\ = -q\int_{\Gamma\cup\Sigma} \frac{\mathbf{D}(\tilde{\mathbf{r}})\cdot\mathbf{m}(\tilde{\mathbf{r}})}{4\pi\varepsilon_s\|\tilde{\mathbf{r}}-\mathbf{r}\|}\mathrm{d}S + q\int_{\Gamma\cup\Sigma} \bar{\varepsilon}'\phi(\tilde{\mathbf{r}})\frac{(\tilde{\mathbf{r}}-\mathbf{r})\cdot\mathbf{m}(\tilde{\mathbf{r}})}{4\pi\varepsilon_s\|\tilde{\mathbf{r}}-\mathbf{r}\|^3}\mathrm{d}S\,, \end{aligned} \tag{3.2.21}$$

where $\bar{\varepsilon}' = \bar{\varepsilon}$ on Γ and $\bar{\varepsilon}' = \varepsilon_s$ on Σ, and $\mathbf{m}$ is the outward normal from Ω_s. The surfaces Γ and Σ play distinct roles: Γ separates Ω_s from Ω_m, and Σ is the external surface enclosing Ω_s. A common simplification arises when the solvent region extends to infinity, in which case the surface integrals over Σ vanish. Under this assumption, the normal vector $\mathbf{m}$ on Γ coincides with $-\mathbf{n}$.
By equating Eqs. (3.2.20) and (3.2.21), and recalling that $\rho^s(\tilde{\mathbf{r}}) = -c(\tilde{\mathbf{r}})\phi(\tilde{\mathbf{r}})$, we arrive at:

$$\int_{\Omega_s} \frac{\rho^s(\tilde{\mathbf{r}})}{4\pi\varepsilon_s\|\tilde{\mathbf{r}}-\mathbf{r}\|}\mathrm{d}V = -\int_{\Gamma} \frac{\mathbf{D}(\tilde{\mathbf{r}})\cdot\mathbf{n}(\tilde{\mathbf{r}})}{4\pi\varepsilon_s\|\tilde{\mathbf{r}}-\mathbf{r}\|}\mathrm{d}S + \int_{\Gamma} \phi(\tilde{\mathbf{r}})\frac{(\tilde{\mathbf{r}}-\mathbf{r})\cdot\mathbf{n}(\tilde{\mathbf{r}})}{4\pi\|\tilde{\mathbf{r}}-\mathbf{r}\|^3}\mathrm{d}S\,. \tag{3.2.22}$$

It is interesting to note that the LHS of the latter equation represents the potential generated by the ions in solution, screened by the polarizable solvent, evaluated at a point $\mathbf{r}$ inside the molecule. This is the exact definition of the *reaction potential* coming from the ions in solution, which we denote as ϕ_{ion} (see Eqs (3.2.18) and (3.1.6)). Here, we have derived this result directly, providing a rigorous foundation for the last two terms of Eq. (3.2.18).
This expression is particularly significant because it converts a volumetric term, that extend over a potentially vast domain, into a much more localized surface term. This equivalence is not only mathematically elegant but also computationally advantageous. It allows us to calculate the ionic direct energy term in a single solving process, in contrast to the more cumbersome approaches described in Sec. 3.1. We will explore this further in Sec. 4.7.2, where the practical implications of this transformation will be demonstrated.

3.2.3 External Electrostatic Potential via Green's Identities

In this section, we present a third application of the Green's identity-based procedure outlined in the previous discussions, offering further insights into the electrostatic potential in the solvent region. In this case, we again assume $\Omega = \Omega_s$, where the free charge density vanishes $\rho^f(\tilde{\mathbf{r}}) = 0$ but the ionic concentration remains nonzero $c(\tilde{\mathbf{r}}) \neq 0$ (except that in the Stern layer, if any). The key difference here lies in our choice of the test function: we adopt the D-H solution for a single charge in solution, with the observer location $\mathbf{r} \in \Omega_s$:

$$v(\tilde{\mathbf{r}}) = \frac{q e^{-k_D \|\tilde{\mathbf{r}}-\mathbf{r}\|}}{4\pi\varepsilon_s \|\tilde{\mathbf{r}}-\mathbf{r}\|} \; . \tag{3.2.23}$$

To simplify the derivation, we assume that the distance of $\mathbf{r}$ from the surface Γ is larger than any d considered in the limiting process for ε_d (see 3.2.1). This ensures that $\varepsilon(\mathbf{r}) = \varepsilon_s$ throughout the region of interest.
Applying this test function, the LHS of Eq. (3.2.8) becomes:

$$\begin{aligned} \int_{\Omega_s} \{L[v(\tilde{\mathbf{r}})]\phi(\tilde{\mathbf{r}}) - L[\phi(\tilde{\mathbf{r}})]v(\tilde{\mathbf{r}})\}\, \mathrm{d}V = -q \int_{Stern\ layer} \phi(\tilde{\mathbf{r}}) \frac{k_D^2 e^{-k_D\|\tilde{\mathbf{r}}-\mathbf{r}\|}}{4\pi \|\tilde{\mathbf{r}}-\mathbf{r}\|} \mathrm{d}V + \\ + q \int_{\Omega_s} \phi(\tilde{\mathbf{r}}) \frac{\nabla\varepsilon(\tilde{\mathbf{r}}) \cdot (\tilde{\mathbf{r}}-\mathbf{r}) e^{-k_D\|\tilde{\mathbf{r}}-\mathbf{r}\|}(1 + k_D\|\tilde{\mathbf{r}}-\mathbf{r}\|)}{4\pi\varepsilon_s \|\tilde{\mathbf{r}}-\mathbf{r}\|^3} \mathrm{d}V + q\phi(\mathbf{r}) \; . \end{aligned} \tag{3.2.24}$$

Here, the term $q\phi(\mathbf{r})$ results from the convolution of $\phi(\tilde{\mathbf{r}})$ with the Dirac delta arising from the PB operator.
Meanwhile, the RHS of Eq. (3.2.8) evaluates to:

$$\begin{aligned} \int_{\Omega_s} \nabla\cdot[\varepsilon(\tilde{\mathbf{r}})v(\tilde{\mathbf{r}})\nabla\phi(\tilde{\mathbf{r}}) - \varepsilon(\tilde{\mathbf{r}})\phi(\tilde{\mathbf{r}})\nabla v(\tilde{\mathbf{r}})]\mathrm{d}V = -q \int_{\Gamma\cup\Sigma} \frac{e^{-k_D\|\tilde{\mathbf{r}}-\mathbf{r}\|}\mathbf{D}(\tilde{\mathbf{r}}) \cdot \mathbf{m}(\tilde{\mathbf{r}})}{4\pi\varepsilon_s \|\tilde{\mathbf{r}}-\mathbf{r}\|} \mathrm{d}S + \\ + q \int_{\Gamma\cup\Sigma} \bar{\varepsilon}' \phi(\tilde{\mathbf{r}}) \frac{e^{-k_D\|\tilde{\mathbf{r}}-\mathbf{r}\|}(1 + k_D\|\tilde{\mathbf{r}}-\mathbf{r}\|)(\tilde{\mathbf{r}}-\mathbf{r}) \cdot \mathbf{m}(\tilde{\mathbf{r}})}{4\pi\varepsilon_s \|\tilde{\mathbf{r}}-\mathbf{r}\|^3} \mathrm{d}S \; , \end{aligned} \tag{3.2.25}$$

where $\bar{\varepsilon}' = \bar{\varepsilon}$ on Γ and $\bar{\varepsilon}' = \varepsilon_s$ on Σ, $\mathbf{m}$ is the outward normal from Ω_s, Γ is the surface separating Ω_s from Ω_m and Σ is the external surface enclosing Ω_s. If, as it is commonly assumed, the solvent region extends to infinity, it can be shown that the surface integrals over Σ vanish. Consistently, the normal vector $\mathbf{m}$ on Γ coincides with $-\mathbf{n}$.
If we now equate Eqs. (3.2.24) and (3.2.25) and rearranging terms, we obtain the following expression for the electrostatic potential outside the molecule:

$$\begin{aligned}\phi(\mathbf{r}) = &\int_{Stern\ layer} \phi(\tilde{\mathbf{r}}) \frac{k_D^2 e^{-k_D\|\tilde{\mathbf{r}}-\mathbf{r}\|}}{4\pi\|\tilde{\mathbf{r}}-\mathbf{r}\|} \mathrm{d}V + \int_\Gamma \frac{e^{-k_D\|\tilde{\mathbf{r}}-\mathbf{r}\|}\mathbf{D}(\tilde{\mathbf{r}})\cdot\mathbf{n}(\tilde{\mathbf{r}})}{4\pi\varepsilon_s\|\tilde{\mathbf{r}}-\mathbf{r}\|}\mathrm{d}S + \\ &- \int_\Gamma \phi(\tilde{\mathbf{r}}) \frac{e^{-k_D\|\tilde{\mathbf{r}}-\mathbf{r}\|}(1+k_D\|\tilde{\mathbf{r}}-\mathbf{r}\|)(\tilde{\mathbf{r}}-\mathbf{r})\cdot\mathbf{n}(\tilde{\mathbf{r}})}{4\pi\|\tilde{\mathbf{r}}-\mathbf{r}\|^3}\mathrm{d}S \ . \end{aligned} \qquad \forall \mathbf{r}\in\Omega_s \ . \tag{3.2.26}$$

As customary in continuum electrostatics, this can be interpreted as the sum of the potential generated by a surface charge distributed on the MS, of that generated by a layer of ideal dipoles located also on the MS, plus a contribution spread over the Stern layer. The electrolytic solution screens both sources of potential. This expression will be used in Sec. 3.4 to evaluate the quality of existing boundary conditions.

3.3 Analytical solutions for LPBE

The LPBE admits analytical solutions only in a limited number of simple cases.[1–6] One of the most well-known examples is the single-sphere model, or Kirkwood model,[1] which provides fundamental insights into how dielectric contrast and ionic screening shape electrostatic potentials. This classic model serves as a cornerstone in electrostatic theory, offering a clear and analytically tractable case for studying charged systems in an electrolyte.

Building on this foundation, we extend our analysis to a more complex yet physically relevant scenario: multiple non-overlapping spheres, each carrying a central point charge. This multi-sphere model introduces asymmetry and breaks the simplicity of the single-sphere case, making it a more rigorous benchmark for testing LPB solvers. By deriving its analytical solution, we offer a valuable tool for assessing the accuracy and limitations of numerical methods used in electrostatic modeling.

3.3.1 Single Sphere-Kirkwood Model

Here, we consider a dielectric sphere of radius R and dielectric constant ε_m, containing a central point charge q, immersed in an electrolyte medium with dielectric constant ε_s and Debye screening parameter k_D. The goal is to determine the electrostatic potential inside and outside the sphere and calculate each term of the energy, as outlined in Eq. (3.1.6).

The system consists of two distinct regions with different dielectric properties, leading to different governing equations for the electrostatic potential $\phi(\mathbf{r})$. Inside the sphere (Ω_m), where the medium is a dielectric with permittivity ε_m and no free ions, the electrostatic potential satisfies Laplace's equation with a point charge at the center. Outside the sphere (Ω_s), the surrounding electrolyte contains mobile ions, leading to Debye screening effects, so the potential satisfies the LPBE:

$$\begin{cases} \nabla^2\phi_{\text{in}} = -\dfrac{q}{\varepsilon_m}\delta(\mathbf{r}) & \mathbf{r} \in \Omega_m \\ \nabla^2\phi_{\text{out}} - \kappa_D^2\phi_{\text{out}} = 0 & \mathbf{r} \in \Omega_s \end{cases} \tag{3.3.1}$$

To solve for $\phi(\mathbf{r})$, we exploit the spherical symmetry of the problem and rewrite Laplace's equation in spherical coordinates:

$$\frac{1}{r^2}\frac{d}{dr}\left(r^2\frac{d\phi_{\text{in}}}{dr}\right) = -\frac{q}{\varepsilon_m}\delta(r) \qquad \text{for} \quad r \leq R\,. \tag{3.3.2}$$

Integrating this equation using Gauss's law, we obtain the well-known Coulomb potential with an additional constant:

$$\phi_{\text{in}}(r) = \frac{q}{4\pi\varepsilon_m r} + A, \tag{3.3.3}$$

where A is a constant representing the contribution of the ionic atmosphere.
Outside the sphere, the LPBE reduces to the modified spherical Bessel equation:

$$\left(\frac{d^2}{dr^2} + \frac{2}{r}\frac{d}{dr} - k_D^2 r^2\right)\phi_{\text{out}} = 0 \quad r > R \tag{3.3.4}$$

whose general solution is:

$$\phi_{\text{out}}(r) = B\frac{e^{-\kappa r}}{r} + C\frac{e^{\kappa r}}{r}. \tag{3.3.5}$$

To ensure that the potential remains finite as $r \to \infty$, we impose $C = 0$, yielding:

$$\phi_{\text{out}}(r) = B\frac{e^{-\kappa r}}{r}. \tag{3.3.6}$$

This solution reveals the characteristic exponential screening introduced by the electrolyte, in contrast to the pure Coulombic $1/r$ dependence observed in vacuum.
The two unknown constants, A and B, are determined by enforcing the boundary conditions at $r = R$, which require continuity of the potential:

$$\phi_{\text{in}}(R) = \phi_{\text{out}}(R), \tag{3.3.7}$$

and continuity of the normal component of the displacement field:

$$\varepsilon_1 \left.\frac{d\phi_{\text{in}}}{dr}\right|_{r=R} = \varepsilon_2 \left.\frac{d\phi_{\text{out}}}{dr}\right|_{r=R}. \tag{3.3.8}$$

Solving for A and B, we obtain:

$$\begin{aligned} A &= \frac{q}{4\pi R}\frac{\varepsilon_m - \varepsilon_s(1+\kappa R)}{\varepsilon_m \varepsilon_s(1+\kappa R)} \\ B &= \frac{q}{4\pi \varepsilon_s}\frac{e^{\kappa R}}{1+\kappa R} \end{aligned} . \tag{3.3.9}$$

Thus, the electrostatic potential is:
Inside the sphere ($r < R$):

$$\phi_{\text{in}}(r) = \frac{q}{4\pi\varepsilon_m}\left(\frac{1}{r} - \frac{1}{R} + \frac{\varepsilon_m}{\varepsilon_s R(1+\kappa R)}\right) . \tag{3.3.10}$$

Outside the sphere ($r > R$):

$$\phi_{\text{out}}(r) = \frac{q}{4\pi\varepsilon_s}\frac{1}{1+\kappa R}\frac{e^{-\kappa(r-R)}}{r}. \tag{3.3.11}$$

These expressions illustrate how the presence of the electrolyte introduces exponential screening beyond the sphere, while the dielectric contrast influences the electrostatic field inside.
Using Eqs. (3.2.17) and (3.2.18), we can express the polarization and ionic contributions to the potential at the charge position:

$$\phi_{pol}(0) = \left(\frac{1}{\varepsilon_s} - \frac{1}{\varepsilon_m}\right)\frac{q}{4\pi R}, \tag{3.3.12}$$

$$\phi_{ion}(0) = -\frac{q}{4\pi\varepsilon_s}\frac{k_D}{1-k_D R}. \tag{3.3.13}$$

The corresponding energy terms, following Eq. (3.1.6), are:

$$\Delta G_{pol} = \frac{1}{2}q\phi_{pol}(0) = \left(\frac{1}{\varepsilon_s} - \frac{1}{\varepsilon_m}\right)\frac{q^2}{8\pi R} , \tag{3.3.14}$$

$$\Delta G_{ion} = \frac{1}{2}q\phi_{ion}(0) = -\frac{q^2}{8\pi\varepsilon_s}\frac{k_D}{(1+k_D R)} . \tag{3.3.15}$$

These expressions match the analytical results for polarization and ionic energies derived in [5, Eq. (88)].

3.3.2 Multi Non-Overlapping Spheres

For solutes represented by N_s non-overlapping dielectric spheres $\Omega_{m,i}$, each with the same dielectric constant $\varepsilon_m = \varepsilon_0 \varepsilon_{r,m}$ and centered at points $\mathbf{r}_i \in \mathbb{R}^3$. Our goal is to determine the total self-consistent electrostatic potential $\phi(\mathbf{r})$ at any point $\mathbf{r} \in \mathbb{R}^3$.

Each sphere $\Omega_{m,i}$ has a radius R_i and contains a fixed, centrally located point charge q_i for $i = 1, \ldots, N_s$. The total potential is given by:[5,6]

$$\phi(\mathbf{r}) = \begin{cases} \phi_{\text{in},i}(\mathbf{r}) = \phi_{coul,i}(\mathbf{r}) + \check{\phi}_{\text{in},i}(\mathbf{r}), & \mathbf{r} \in \Omega_{m,i}, \\ \phi_{\text{out}}(\mathbf{r}) = \sum_{i=1}^{N_s} \phi_{\text{out},i}(\mathbf{r}), & \mathbf{r} \in \Omega_s, \end{cases} \tag{3.3.16}$$

where the summation $\sum_{i=1}^{N_s}(\cdot)$ in ϕ_{out} reflects the superposition principle, which applies in the Debye-Hückel description. The term $\phi_{coul,i}$ in (3.3.16) represents the Coulombic potential due to the given free charge q_i situated at $\mathbf{r}_i$:

$$\phi_{coul,i}(\mathbf{r}) = \frac{q_i}{4\pi\varepsilon_m \|\mathbf{r} - \mathbf{r}_i\|} \,. \tag{3.3.17}$$

The unknown potentials $\check{\phi}_{\text{in},i}$ and $\phi_{\text{out},i}$ are expressed through local eigenfunction expansions of Laplace type for $\check{\phi}_{\text{in},i}$ and Poisson-Boltzmann type for $\phi_{\text{out},i}$:

$$\begin{aligned} \check{\phi}_{\text{in},i}(\mathbf{r}) &= \sum\nolimits_{n,l} L_{nl,i} \tilde{\varrho}_i^n Y_n^l(\hat{\boldsymbol{\varrho}}_i) \,, \\ \phi_{\text{out},i}(\mathbf{r}) &= \sum\nolimits_{n,l} G_{nl,i} k_n(\tilde{\varrho}_i) Y_n^l(\hat{\boldsymbol{\varrho}}_i) \,. \end{aligned} \tag{3.3.18}$$

Here, the dimensionless $\tilde{\varrho}_i = k_D \varrho_i$ is the scaled (by a Debye screening length k_D^{-1}) radial coordinate of $\mathbf{r}$ measured from the i-th sphere's center:

$$\boldsymbol{\varrho}_i = \mathbf{r} - \mathbf{r}_i \,, \quad \varrho_i = \|\boldsymbol{\varrho}_i\| \quad \text{and} \quad \hat{\boldsymbol{\varrho}}_i = \boldsymbol{\varrho}_i / \varrho_i \,,$$

$k_n(\cdot)$ are modified spherical Bessel functions of the second kind, and $Y_n^l(\cdot)$ are the standard orthonormal complex-valued spherical harmonics (see Ref. [10]). The summation $\sum_{n,l}(\cdot)$ expands as $\sum_{n=0}^{+\infty} \sum_{l=-n}^{n}(\cdot)$.

Unknown coefficients $L_{nl,i}$ and $G_{nl,i}$ of (3.3.18) are determined by enforcing boundary conditions on the boundaries of spheres :

$$\begin{aligned} \phi_{\text{in},i}\big|_{\varrho_i \to R_i^-} &= \phi_{\text{out}}\big|_{\varrho_i \to R_i^+} \,, \\ \varepsilon_m \, (\hat{\mathbf{n}}_i \cdot \nabla \phi_{\text{in},i})\big|_{\varrho_i \to R_i^-} &= \varepsilon_s \, (\hat{\mathbf{n}}_i \cdot \nabla \phi_{\text{out}})\big|_{\varrho_i \to R_i^+} \,, \end{aligned} \tag{3.3.19}$$

where $\hat{\mathbf{n}}_i$ is the outer unit normal on the boundary of $\Omega_{m,i}$.

When enforcing the boundary conditions (3.3.19) on the i-th spherical surface, all quantities must be expressed using the same set of basis functions—specifically, spherical harmonics $\{Y_n^l(\hat{\boldsymbol{\varrho}}_i)\}_{0 \le |l| \le n}$. To achieve this consistency, we expand the offside (i.e., those centered at $\mathbf{r}_j$, with $j \neq i$) screened harmonics $\{k_n(\tilde{\varrho}_j) Y_n^l(\hat{\boldsymbol{\varrho}}_j)\}_{0 \le |l| \le n}$ in ϕ_{out}

---

[10] J. D. Jackson. *Classical electrodynamics*. 3rd ed. London, Sydney, Singapore, New York: John Wiley & Sons Ltd, 1999..

using relations derived in Refs. [11] and [12]:

$$k_L(\tilde{\varrho}_j)Y_L^M(\hat{\boldsymbol{\varrho}}_j) = \textstyle\sum_{l_1,m_1} \mathcal{H}_{l_1 m_1}^{LM}(\mathbf{a}_{ij}) i_{l_1}(\tilde{\varrho}_i) Y_{l_1}^{m_1}(\hat{\boldsymbol{\varrho}}_i)\ . \tag{3.3.20}$$

In Eq (3.3.20), $i_n(\cdot)$ represents modified spherical Bessel functions of the first kind, and the coefficient $\mathcal{H}_{l_1 m_1}^{LM}(\mathbf{a}_{ij})$ is

$$\mathcal{H}_{l_1 m_1}^{LM}(\mathbf{a}_{ij}) = \sum_{l_2,m_2} (-1)^{l_1+l_2} H_{l_1 m_1 l_2 m_2}^{LM} k_{l_2}(\tilde{a}_{ij}) Y_{l_2}^{m_2}(\hat{\mathbf{a}}_{ij}) \tag{3.3.21}$$

where $\mathbf{a}_{ij} = \mathbf{r}_j - \mathbf{r}_i$ points from $\mathbf{r}_i$ to $\mathbf{r}_j$, $\varrho_i < a_{ij} = \|\mathbf{a}_{ij}\|$, $\tilde{a}_{ij} = k_D a_{ij}$, and

$$H_{l_1 m_1 l_2 m_2}^{LM} = C_{l_1 0 l_2 0}^{L0} C_{l_1 m_1 l_2 m_2}^{LM} \sqrt{\frac{4\pi(2l_1+1)(2l_2+1)}{2L+1}}\ . \tag{3.3.22}$$

Here, $C_{l_1 m_1 l_2 m_2}^{LM} = \langle l_1 l_2; m_1 m_2 \mid LM \rangle$ are Clebsch-Gordan coefficients. This formulation ensures a proper mathematical treatment of mutual polarization effects.
These operations readily convert boundary conditions (3.3.19) into a linear algebraic system governing the unknown coefficients of (3.3.18). Solving this system numerically fully determines the unknown potentials in (3.3.18). In practical computations, as in the case of a two-sphere system extensively described in Ref. [5], one must impose a truncation on the index n in (3.3.18)—setting an upper limit $n_{\max}$ determined by the user. This restriction influences the size of the resulting linear system. By progressively increasing $n_{\max}$, one ensures that computed quantities, such as potentials and energy, converge—i.e., their variations become negligible, staying within the reported numerical precision.
According to (3.3.16), the total electrostatic energy is given by:

$$\begin{aligned} \Delta G &= \frac{1}{2}\sum_{i=1}^{N_s} q_i \cdot \left(\phi_{\mathrm{in},i} - \phi_{coul,i}\right)\Big|_{\varrho_i=0} \\ &= \frac{1}{2}\sum_{i=1}^{N_s} q_i \cdot \check{\phi}_{\mathrm{in},i}\Big|_{\varrho_i=0} = \frac{1}{2}\sum_{i=1}^{N_s} q_i L_{00,i}/\sqrt{4\pi} \end{aligned} \tag{3.3.23}$$

where we have used the fact that $Y_0^0 = \frac{1}{\sqrt{4\pi}}$. The subtraction of the Coulombic potential $\phi_{coul,i}$ from the full potential $\phi_{\mathrm{in},i}$ in equation (3.3.16) ensures the removal of the self-energy term, preventing an infinite energy contribution.[5,8] To enhance the ability to compare calculations based on this analytical model with numerical results,[8] it is desirable to be able to compute not only the total electrostatic energy ΔG, but also its

---

[11] Y.-K. Yu. "Electrostatics of charged dielectric spheres with application to biological systems. III. Rigorous ionic screening at the Debye-Hückel level". *Physical Review E* 102, p. 052404, 2020..

[12] O. I. Obolensky, T. P. Doerr, and Yi-Kuo Yu. "Rigorous treatment of pairwise and many-body electrostatic interactions among dielectric spheres at the Debye-Hückel level". *Eur. Phys. J. E* 44, p. 129, 2021..

individual components (see (3.1.6)). While the Coulombic contribution is straightforward to determine, the computation of the remaining components is more intricate. To compute $\phi_{\text{pol},i,i}$ at point $\mathbf{r}_i$ (i.e., the center of the i–th sphere), we start by considering how the total polarization charge is distributed on the sphere's surface. The polarization charge density at $\varrho_i = R_i$ is given by:[5]

$$\begin{aligned}\sigma_{\text{tot},i}(\hat{\boldsymbol{\varrho}}_i) &= \varepsilon_0\left(\frac{1}{\varepsilon_m} - \frac{1}{\varepsilon_s}\right)\varepsilon_m k_D \frac{\partial}{\partial\tilde{\varrho}_i}\phi_{\text{in},i}\Big|_{\varrho_i=R_i} \\ &= \varepsilon_0\left(\frac{1}{\varepsilon_m} - \frac{1}{\varepsilon_s}\right)\varepsilon_m k_D\left(\frac{-q_i k_D}{4\pi\varepsilon_m\tilde{\varrho}_i^2} + \sum_{n,l} L_{nl,i} n \tilde{\varrho}_i^{n-1} Y_n^l(\hat{\boldsymbol{\varrho}}_i)\right)\Bigg|_{\varrho_i=R_i} .\end{aligned}$$

To determine the resulting reaction potential $\phi_{\text{pol},i,i}$ generated by this charge density at $\mathbf{r}_i$ (the center of the i–th sphere), we integrate the polarization charge density over the surface $\partial\Omega_{m,i}$ of sphere $\Omega_{m,i}$. Due to the orthogonality property of spherical harmonics, only the monopole term (i.e., the term with $n = 0$) contributes to the integral. This leads to a significant simplification, yielding:

$$\phi_{\text{pol},i,i} = \frac{1}{4\pi\varepsilon_0}\oint_{\partial\Omega_{m,i}} \frac{\sigma_{\text{tot},i}(\hat{\boldsymbol{\varrho}}_i)}{R_i}\mathrm{d}S = \frac{q_i}{4\pi R_i}\left(\frac{1}{\varepsilon_s} - \frac{1}{\varepsilon_m}\right) . \tag{3.3.24}$$

This result has an important physical interpretation. The reaction potential $\phi_{\text{pol},i,i}$ represents the electrostatic potential at the center of the sphere due to the induced surface charges. If the two permittivities were equal, this term would vanish, indicating that no polarization effects occur. However, when there is a dielectric mismatch, polarization charges appear at the interface, modifying the potential inside the sphere.
To determine the potential $\phi_{\text{pol},i,j}$ created by the same density $\sigma_{\text{tot},i}$ and evaluated at point $\mathbf{r}_j$, we integrate over the sphere's surface:

$$\phi_{\text{pol},i,j} = \frac{1}{4\pi\varepsilon_0}\oint_{\partial\Omega_{m,i}} \frac{\sigma_{\text{tot},i}(\hat{\boldsymbol{\varrho}}_i)\mathrm{d}S}{\|R_i\hat{\boldsymbol{\varrho}}_i - \mathbf{a}_{ij}\|} .$$

Here, the denominator represents the distance between an arbitrary surface point $R_i\hat{\boldsymbol{\varrho}}_i$ and the point $\mathbf{r}_j$, with $\mathbf{a}_{ij}$ denoting the displacement vector between sphere centers. Thus, $\boldsymbol{\varrho}_j = R_i\hat{\boldsymbol{\varrho}}_i - \mathbf{a}_{ij}$ is the vector pointing from $\mathbf{r}_j$ to a integration point on on $\partial\Omega_{m,i}$. To evaluate this integral, we use the addition theorem for spherical harmonics [10, § 3.6], which allows us to express the inverse distance as:

$$\frac{1}{\|R_i\hat{\boldsymbol{\varrho}}_i - \mathbf{a}_{ij}\|} = \frac{4\pi}{a_{ij}}\sum_{n,l}\frac{1}{2n+1}\left(\frac{R_i}{a_{ij}}\right)^n Y_n^l(\hat{\mathbf{a}}_{ij})Y_n^l(\hat{\boldsymbol{\varrho}}_i)^\star . \tag{3.3.25}$$

This expansion is particularly useful because of the orthogonality property of spherical harmonics when integrated over a sphere's surface. When substituting this expression into the integral, only terms with matching harmonics survive, leading to a simplified formula for $\phi_{\mathrm{pol},i,j}$:

$$\begin{aligned}\phi_{\mathrm{pol},i,j} =& \frac{q_i}{4\pi a_{ij}}\left(\frac{1}{\varepsilon_s}-\frac{1}{\varepsilon_m}\right)\\ &+\left(1-\frac{\varepsilon_m}{\varepsilon_s}\right)\sum_{n,l}\frac{n\tilde{R}_i^n L_{nl,i}}{2n+1}\left(\frac{R_i}{a_{ij}}\right)^{n+1} Y_n^l(\hat{\mathbf{a}}_{ij})\end{aligned} \tag{3.3.26}$$

where $\tilde{R}_i = k_D R_i$. The first term in (3.3.26) represents the classical image charge potential in a dielectric medium, analogous to the result obtained for a single sphere in an otherwise uniform dielectric. The second term, containing a sum over spherical harmonics, accounts for higher-order polarization effects that arise due to charge distribution asymmetries and interactions between different multipoles.

With the reaction potentials (3.3.24) and (3.3.26) now determined, the corresponding polarization energy contributions can be computed straightforwardly: $\frac{1}{2}q_i\phi_{\mathrm{pol},i,i}$ and $\frac{1}{2}q_j\phi_{\mathrm{pol},i,j}$, for all $i,j=\overline{1,\ldots,N_s}$, $j\neq i$. In particular, for a single isolated sphere, the self-energy term reduces to:

$$\Delta G_{pol} = \frac{1}{2}q_i\phi_{\mathrm{pol},i,i} = \frac{q_i^2}{8\pi R_i}\left(\frac{1}{\varepsilon_s}-\frac{1}{\varepsilon_m}\right),$$

which coincides with the classical Born energy expression in the zero ionic strength limit (see Ref. [5]). This demonstrates the agreement between our analytical framework and conventional electrostatic solvation models.

The ionic energy contributions (see (3.1.6)) can be computed by subtracting both the Coulombic and polarization contributions from the total energy ΔG. This step is crucial for making comparisons between analytical and numerical approaches to electrostatic modeling.

To validate and apply these analytical formulas in practical calculations, we have implemented MATLAB scripts for computing the potential and energy. The scripts are publicly available at `https://github.com/concept-lab/Analytical_Electrostatics/tree/main`. This implementation allows for efficient evaluation of electrostatic interactions in multi-sphere systems, making it a valuable tool for further research in biomolecular electrostatics and solvation modeling.

This analytical solution is particularly valuable as a benchmark because multi-sphere systems break global spherical symmetry, a feature rarely present in real biological environments. As a result, they offer a more realistic representation of biomolecular systems, where asymmetry and structural complexity are the norm.

3.4 Boundary conditions

In the idealized case of an infinite domain, the natural boundary condition for the PBE is that the electrostatic potential vanishes at infinity. The previous analytical solutions are derived under this assumption, as it ensures a well-posed problem without the need for artificial constraints. However, real bio-molecular problems require numerical solutions, which are necessarily restricted to a finite computational domain. In this case, choosing appropriate boundary conditions becomes crucial to minimizing artifacts and ensuring that the truncated domain provides an accurate approximation of the infinite system.

From a physical standpoint, the electrostatic potential and field are expected to decay to zero at a sufficient distance from the fixed charges. A straightforward approach is to impose homogeneous Dirichlet boundary conditions, setting the potential to zero at the domain boundary. However, this assumption is only valid when the *perfil*, that is the ratio between the size of the solute and that of the computational domain, is relatively small.

To extend the validity of the solution to larger *perfil* values, analytical approximations for the potential at an intermediate distance are often employed. A commonly used approach is the (D-H) boundary condition, which refines the basic Coulombic model by incorporating ionic screening effects. For a system with N fixed charges in a solvent containing a dissociated monovalent salt, the D-H potential takes the form:

$$\phi(\mathbf{r}) = \sum_{i=1}^{N} \frac{q_i e^{-k_D \|\tilde{\mathbf{r}}-\mathbf{r}\|}}{4\pi\varepsilon_s \|\tilde{\mathbf{r}}-\mathbf{r}\|} \,. \tag{3.4.1}$$

This approximation, also called the "fully penetrating solvent" model,[13] which consider the charges directly exposed to the solvent, introduces significant discrepancies compared to a more realistic scenario where charges reside within a low-dielectric solute. Two primary limitations arise: first, the model neglects the dipolar contribution generated in the low-polarization medium; second, it inaccurately places counterions within regions actually occupied by the solute. Of these, the second effect is more impactful than the first, which decays as a screened dipolar potential does.

A clear example of these limitations can be seen in the analytical solution for the LPBE in the simplest case: a single spherical solute of radius R with a central charge with a single charge q located in its center (3.3.11):

$$\phi(r) = \phi_{coul}(r) \frac{e^{kR}}{(1+kR)}$$

From this expression, it is evident that the difference between the actual potential and its D-H approximation vanishes at the same rate as the potential itself. This implies that the D-H approximation fails as a true asymptotic solution.

---

[13] W. Rocchia. "Poisson-Boltzmann equation boundary conditions for biological applications", 41pp. 1109–1118, 2005.

Let's now extend this reasoning to the more general case described by Eq. (3.2.26). We observe that the first two terms are prevalent at larger distances than the second one, since the potential generated by a dipole layer decays faster than that of a surface charge. One can thus conclude, at least qualitatively, that a more accurate asymptotic solution should be written as the sum of Debye-Hückel-like terms centered on points lying on the MS or in the Stern layer. This consideration, however, does not provide details on the parameters of these terms, since their knowledge requires that of the electric displacement at the MS, which become available only after the PBE is solved. Along the same qualitative lines, one could expect that the discrepancy between the actual potential and that obtained by the penetrating solvent approximation should increase with the volume of the solute, which excludes more counterions, and with its absolute net charge, which reduces the possibility of cancellations in the ionic reaction.

Chapter 4

Numerical Model

In this chapter, we present the numerical framework developed to discretize the Poisson–Boltzmann equation, which lies at the core of our electrostatic modeling approach. The construction of this scheme has been guided by two complementary objectives. On one hand, we aim to achieve high accuracy in evaluating the electrostatic potential and energy, particularly near the molecular surface where the dielectric discontinuity presents significant computational challenges. On the other hand, the scale of the problems typically encountered in biomolecular simulations requires a discretization strategy that yields sparse matrices with a simple structure and minimal stencil.

To address the issue of accuracy near the interface, we incorporate a physically and numerically motivated treatment of the permittivity discontinuity. In particular, we adopt a Weighted Harmonic Average (WHA) of the dielectric constant, introduced in Sec. 4.4. This technique ensures a consistent and stable representation of the jump in material properties across the molecular surface, reflecting the underlying physics more faithfully than naive interpolation schemes. The WHA is embedded within the Primal-Mixed Finite Element Method (PMFEM), which serves as the core of our numerical formulation, using a particular quadrature rule, described in Sec. 4.5.

The choice of a low-order finite element discretization on a structured Cartesian grid helps to control complexity and enables the use of efficient solvers. We also make use of reduced integration techniques,[1] which not only reduce computational cost but also help to prevent artificial stiffness that may arise in full integration schemes.

Our method begins with a reformulation of the second-order elliptic equation into a system of first-order equations. This mixed formulation introduces the electrostatic potential ϕ and the electric displacement field $\mathbf{D}$ as separate variables, allowing for a finer treatment of discontinuities. In particular, we adopt a primal mixed approach,[2,3]

---

[1] David S Malkus and Thomas JR Hughes. "Mixed finite element methods – reduced and selective integration techniques: a unification of concepts", 15pp. 63–81, 1978.

[2] J.E. Roberts and J.-M. Thomas. "Mixed and hybrid methods". In: *Finite Element Methods (Part 1)*. Vol. 2. Handbook of Numerical Analysis. Elsevier, 1991. Pp. 523–639. DOI: `https://doi.org/10.1016/S1570-8659(05)80041-9`.

[3] Thomas H. Robey. "The primal mixed finite element method and the LBB condition", 8pp. 357–379, 1992.

where global continuity is enforced for ϕ, while a partially discontinuous representation is permitted for $\mathbf{D}$. This asymmetry reflects the physical nature of the problem and improves numerical flexibility near interfaces. To reduce the number of globally coupled unknowns, we apply a standard static condensation procedure,[4] eliminating the degrees of freedom associated with the auxiliary variable $\mathbf{D}$ at the element level. In practice, this significantly enhances computational efficiency without sacrificing accuracy.

An additional strength of our implementation lies in its support for hierarchical mesh refinement. By adaptively refining the grid only in regions where higher resolution is needed, typically around the molecular boundary, we achieve substantial savings in memory and computation. Although our framework supports non-conforming meshes and the presence of hanging nodes, as discussed in earlier work,[5,6] we will focus on the simpler case of a full tensor-product Cartesian grid, in order to highlight the essential features of the our PMFEM strategy without the distraction of additional technicalities.

We implement the methods presented in this chapter for solving the LPBE in the software package `NextGenPB`, which has been developed specifically for efficient and accurate electrostatic computations in biomolecular systems.

4.1 Primal–Mixed Finite Elements Discretization of the LPBE

As already mentioned above, we start the derivation by formulating LPBE (2.5.15), over a domain $\Omega \subset \mathbb{R}^3$ as a system of two first order equations:

$$\begin{cases} \dfrac{1}{\varepsilon}\mathbf{D} + \nabla\phi & = 0 \\ \nabla \cdot \mathbf{D} + c\,\phi & = \rho^f. \end{cases} \tag{4.1.1}$$

We assume for the time being that homogeneous Dirichlet–type Boundary conditions are enforced on the whole boundary $\partial\Omega$ of Ω. A more in-depth discussion of boundary conditions will be provided in Sec. 4.8, and they are also addressed analytically in Sec. 3.4.

In order to numerically solve (4.1.1) via a Galerkin/Finite Element approximation we must, first of all, state the problem in weak form. To this end, we multiply both equations in (4.1.1) by suitable *test functions* and perform integration by parts to obtain:

---

[4] O. C. Zienkiewicz, R. L. Taylor, and J. Z. Zhu. *The finite element method*. Vol. 1. Butterworth-Heinemann Oxford, UK, 2013.

[5] Pasquale Claudio Africa, Carlo de Falco, and Simona Perotto. "Scalable recovery-based adaptation on Cartesian quadtree meshes for advection-diffusion-reaction problems", 1pp. 443–473, 2023.

[6] Federico Gatti et al. "Parallel simulations for fast-moving landslides: Space-time mesh adaptation and sharp tracking of the wetting front", 95pp. 1286–1309, 2023.

$$
\begin{aligned}
&\text{find } (\mathbf{D},\phi) \in U \times W \text{ s.t. } \forall(\boldsymbol{\sigma},w) \in U \times W : \\
&\int_D \frac{1}{\varepsilon}\,\mathbf{D}\cdot\boldsymbol{\sigma}\,\mathrm{d}V + \int_D \nabla\phi\cdot\boldsymbol{\sigma}\,\mathrm{d}V \quad = \quad 0\,, \\
&\int_D \mathbf{D}\cdot\nabla w\,\mathrm{d}V - \int_D c\,\phi\,w\,\mathrm{d}V \quad = \quad -\int_D \rho^f\,w\,\mathrm{d}V\,,
\end{aligned}
\tag{4.1.2}
$$

where $U \equiv \left(L^2(\Omega)\right)^3$ and $W \equiv H_0^1(\Omega)$. Introducing the bilinear forms $a(\cdot,\cdot) : U \times U \to \mathbb{R}$ and $b(\cdot,\cdot) : U \times W \to \mathbb{R}$, $\kappa(\cdot,\cdot) : W \times W \to \mathbb{R}$ and the linear operator $R : W \to \mathbb{R}$,

$$
\begin{aligned}
a(\mathbf{u},\mathbf{z}) &= \int_D \frac{1}{\varepsilon}\mathbf{u}\cdot\mathbf{z}\,\mathrm{d}V\,, \\
b(\mathbf{u},w) &= \int_D \mathbf{u}\cdot\nabla w\,\mathrm{d}V\,, \\
\kappa(w,v) &= \int_D c\,w\,v\,\mathrm{d}V\,, \\
R(w) &= \int_D \rho^f\,w\,\mathrm{d}V\,.
\end{aligned}
\tag{4.1.3}
$$

Eq. (4.1.2) becomes:

$$
\begin{aligned}
&\text{find } (\mathbf{D},\phi) \in U \times W \textit{ s.t.} \\
&\begin{cases}
a(\mathbf{D},\boldsymbol{\sigma}) + b(\boldsymbol{\sigma},\phi) = 0 \\
b(\mathbf{D},w) - \kappa(\phi,w) = -R(w)
\end{cases} \\
&\forall(\boldsymbol{\sigma},w) \in U \times W
\end{aligned}
\tag{4.1.4}
$$

The Galerkin/Finite Element method for the numerical approximation of (4.1.4) consists of looking for an approximate solution $(\mathbf{D}_h,\phi_h) \in U_h \times W_h$, where

$$
\begin{aligned}
&W_h \subset W, \;\; \dim(W_h) = N_v^h < \infty \\
&U_h \subset U, \;\; \dim(U_h) = N_e^h < \infty
\end{aligned}
$$

are two families of *finite dimensional* subspaces depending on the parametrized by the *mesh size h s.t.* $U_h \to U$ and $W_h \to W$ for $h \to 0$. Then, the discretized version of (4.1.4) takes the form:

$$\begin{aligned}
&\text{find } (\mathbf{D}_h, \phi_h) \in U_h \times W_h \ s.t. \\
&\begin{cases} a(\mathbf{D}_h, \boldsymbol{\sigma}) + b(\boldsymbol{\sigma}, \phi_h) = 0 \\ b(\mathbf{D}_h, w) - \kappa(\phi_h, w) = -R(w) \end{cases} \\
&\forall (\boldsymbol{\sigma}, w) \in U_h \times W_h
\end{aligned} \tag{4.1.5}$$

In order to guarantee the stability of (4.1.5), the chosen pair of finite dimensional spaces U_h and W_h must satisfy the Ladyzhenskaya–Babuška–Brezzi (LBB) condition[2,7] which is simply attained if $\nabla W_h \subset U_h$.[3] Denoting by $\{\boldsymbol{\sigma}_i\}$ a basis of U_h and by $\{w_k\}$ a basis of W_h, we can write $\mathbf{D}_h$ and ϕ_h as an appropriate linear combination of these bases, i.e.:

$$\mathbf{D}_h = \sum_{j=1}^{N_e^h} D_j^h \boldsymbol{\sigma}_j \ , \quad \phi_h = \sum_{k=1}^{N_v^h} \phi_k^h w_k \ . \tag{4.1.6}$$

We note that the dimension N_e^h of U_h is the number of edges in the mesh and dimension N_v^h of W_h is the number of interior vertices. We shall then request:

$$\begin{cases} \sum_j D_j^h a(\boldsymbol{\sigma}_j, \boldsymbol{\sigma}_i) + \sum_k \phi_k^h b(\boldsymbol{\sigma}_i, w_k) = 0 & \forall i\,, \\ \sum_j D_j^h b(\boldsymbol{\sigma}_j, w_n) - \sum_k \phi_k^h \kappa(w_k, w_n) = -R(w_n) & \forall n. \end{cases} \tag{4.1.7}$$

The matrix form of (4.1.7) is

$$\begin{bmatrix} \tilde{A} & B^T \\ B & -C \end{bmatrix} \begin{bmatrix} \mathbf{D}^h \\ \boldsymbol{\phi}^h \end{bmatrix} = \begin{bmatrix} 0 \\ -\boldsymbol{R} \end{bmatrix} , \tag{4.1.8}$$

where $\tilde{A} = [a(\boldsymbol{\sigma}_i, \boldsymbol{\sigma}_j)] = [a_{i,j}]$, $B = [b(\boldsymbol{\sigma}_i, w_k)] = [b_{i,k}]$, $\mathbf{D}^h = [D_1^h, \ldots, D_{N_e^h}^h]$, $\boldsymbol{\phi}^h = [\phi_1^h, \ldots \phi_{N_v^h}^h]$, $C = [\kappa(w_k, w_n)]$ and $\boldsymbol{R} = [R(w_1), \ldots, R(w_{N_v^h})]$.

In problems involving heterogeneous media, accurately computing the electric field $\mathbf{E} = -\nabla\phi$ presents additional challenges, particularly when the dielectric coefficient ε exhibits discontinuities that do not align with the computational grid. A naïve finite difference approach applied to a piecewise linear potential ϕ fails to capture these jumps, leading to spurious numerical artifacts.

The PMFEM effectively addresses this issue by introducing the dielectric displacement field, $\mathbf{D} = \varepsilon\mathbf{E}$, as an independent variable. Instead of enforcing the relation $\mathbf{E} = \varepsilon^{-1}\mathbf{D}$ pointwise, which can be prone to numerical instability near discontinuities, PMFEM approximates $\mathbf{D}$ in a way that naturally respects material interfaces.

---

[7] Daniele Boffi, Franco Brezzi, and Michel Fortin. In: "Algebraic Aspects of Saddle Point Problems". Pp. 123–195. Berlin, Heidelberg: Springer Berlin Heidelberg, 2013. DOI: `10.1007/978-3-642-36519-5\_3`.

This ensures a more stable and physically consistent treatment of permittivity variations, improving accuracy where traditional methods struggle. By prioritizing an accurate representation of **D**, PMFEM offers a robust and reliable approach to modeling electrostatics in complex media.

In the following sections, we provide a detailed description of the finite element spaces U_h and W_h. Additionally, we demonstrate that using the trapezoidal rule for quadrature, which places nodes at element vertices, leads to a discretization where permittivity is harmonically averaged along edges. While this is consistent with standard finite element techniques, we explore how modifying the quadrature weights (or equivalently, adjusting the averaging of permittivity) can significantly enhance accuracy, particularly in regions near the molecular surface where electrostatic effects are most sensitive to interface discontinuities.

4.2 FE Spaces W_h and U_h

The finite element spaces W_h and U_h, introduced in Sec. 4.1, form the backbone of our numerical approach to solving the governing equations (4.1.1). To construct them, we begin by introducing a partition $\mathcal{T}_h$ of the computational domain $\Omega \subset \mathbb{R}^3$. This partition consists of a finite set of non-overlapping elements K_i satisfying:

$$\mathcal{T}_h = \{K_i : \; K_i \cap K_j = \varnothing, \; i \neq j, \; \bar{\Omega} = \bigcup_i K_i\} \,, \tag{4.2.1}$$

where $\bar{\Omega}$ denotes the closure of Ω, and the parameter h represents the characteristic size of the elements.

To ensure a structured and efficient discretization, we adopt a Cartesian-product mesh. This results in a hexahedral grid obtained by partitioning the edges of Ω along the x-, y-, and z-axes, forming a regular lattice of cuboidal elements, simplifying numerical implementation.

To systematically define finite element functions on this mesh, we introduce the concept of a *reference element* $\hat{K}$, a standardized unit domain from which all elements in $\mathcal{T}_h$ are derived. Each physical element K is mapped from $\hat{K}$ using an invertible affine transformation F_K:

$$\begin{aligned} F_K \colon \mathbb{R}^3 &\to \mathbb{R}^3 \\ \hat{\mathbf{r}} &\mapsto F_K(\hat{\mathbf{r}}) = T_K \hat{\mathbf{r}} + t_K \,, \end{aligned}$$

where $T_K \in \mathbb{R}^3 \times \mathbb{R}^3$ is a nonsingular matrix encoding scaling, rotation, and shear effects, while $t_K \in \mathbb{R}^3$ is a translation vector (see Fig. 4.1). In the case of a structured Cartesian grid, the reference element $\hat{K}$ is the unit cube $[0,1]^3$. This standardized transformation provides a systematic way to describe finite element functions while maintaining geometric flexibility.

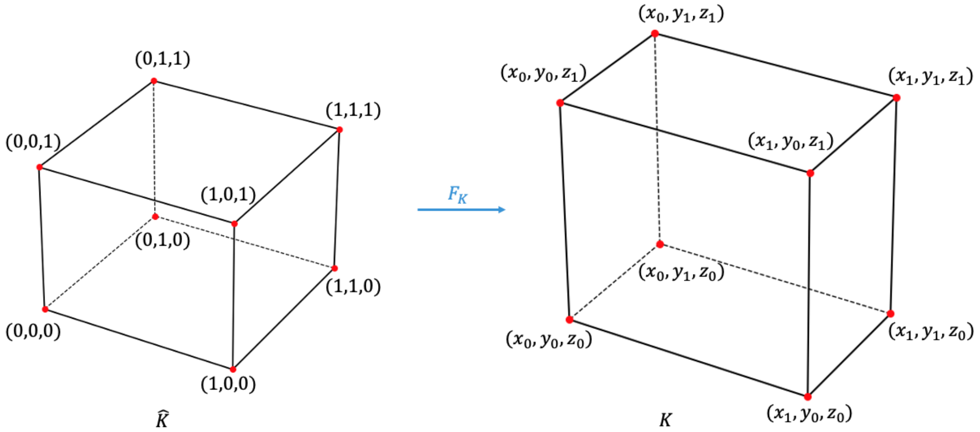

FIGURE 4.1: An affine transformation from a unit cube to a generic hexadron.

4.2.1 FE space for scalar functions: W_h

For a given partition $\mathcal{T}_h$, to approximate functions in $H_0^1(\Omega)$ while maintaining continuity across element boundaries, we construct the finite element space W_h as a conforming subspace. This space consists of piecewise polynomial functions:[8]

$$W_h = \{v \in \mathcal{C}^0(\bar{\Omega}) : v|_{\partial\Omega} = 0,\ v|_{K_t} \in \mathbb{P}_{l,m,n}(K_t),\ \forall K_t \in \mathcal{T}_h, \}\ , \tag{4.2.2}$$

where l, m, $n \in \mathbb{N}$, and $\mathbb{P}_{l,m,m}(K_t)$ represents the space of polynomials in three variables $(x, y, z) \in K_t$ with maximum degrees l, m, and n, respectively:

$$\mathbb{P}_{l,m,m}(K_t) = \{p_{l,m,n}(x,y,z) = \sum_{\substack{0\leq i\leq l \\ 0\leq j\leq m \\ 0\leq k\leq n}} \alpha_{i,j,k}\, x^i y^j z^k\ ,\ \mathbf{r} = (x,y,z) \in K_t\}\ . \tag{4.2.3}$$

The dimension of this polynomial space is $\dim(\mathbb{P}_{l,m,m}) = (l+1)(m+1)(n+1)$.
For computational efficiency, we adopt W_h as the space of piecewise trilinear continuous functions, corresponding to $\mathbb{P}_{1,1,1}(K_t)$. This choice ensures a balance between accuracy and computational cost. To construct the discrete representation of functions in W_h, we define the set of nodal points $X_v^h = \{\mathbf{r}_k\}_{k=1}^{N_v^h}$, which characterize the partition $\mathcal{T}h$. The basis functions $\{w_k\}_{k=1}^{N_v^h}$ for W_h are Lagrangian, satisfying the interpolation property:

---

[8] D. Boffi, F. Brezzi, and M. Fortin. *Mixed Finite Element Methods and Applications*. Vol. 44. Springer Series in Computational Mathematics. Berlin Heidelberg: Springer-Verlag, 2013.

$$w_k \in W_h : \; w_k(\mathbf{r}_l) = \delta_{kl} \quad \forall \mathbf{r}_l \in X_v^h \,, \tag{4.2.4}$$

where δ_{kl} is the Kronecker delta. Given an element K_t, the eight tri-linear Legendre basis associate to its nodes are defined as follow:

$$w_k(\mathbf{r}) = w_{x_a,y_b,z_c}(x,y,z) = l_a(x)l_b(y)l_c(z) \quad a,b,c = -1,1 \tag{4.2.5}$$

where

$$l_{-1}(\nu) = \frac{\nu_1 - \nu}{h_\nu} \qquad\qquad l_1 = \frac{\nu - \nu_0}{h_\nu}, \quad \nu = x,y,z \,. \tag{4.2.6}$$

Here, h_ν denotes the length of the element in the ν-direction, while ν_0 and ν_1 are the coordinates of the two endpoints of the element along that direction. In the reference element $\hat{K}$, the eight nonzero trilinear basis functions take the form:

$$\begin{aligned}
w_1(\hat{\mathbf{r}}) &= (1-\hat{x})(1-\hat{y})(1-\hat{z}) & \qquad w_5(\hat{\mathbf{r}}) &= (1-\hat{x})(1-\hat{y})\hat{z} \\
w_2(\hat{\mathbf{r}}) &= \hat{x}(1-\hat{y})(1-\hat{z}) & w_6(\hat{\mathbf{r}}) &= \hat{x}(1-\hat{y})\hat{z} \\
w_3(\hat{\mathbf{r}}) &= (1-\hat{x})\hat{y}(1-\hat{z}) & w_7(\hat{\mathbf{r}}) &= (1-\hat{x})\hat{y}\hat{z} \\
w_4(\hat{\mathbf{r}}) &= \hat{x}\hat{y}(1-\hat{z}) & w_8(\hat{\mathbf{r}}) &= \hat{x}\hat{y}\hat{z}
\end{aligned}$$

With this choice of basis, any scalar discrete function $\varphi_h \in W_h$ can be written as a linear combination of the basis functions, using a set of coefficients $\{\varphi_k^h\}_{k=1}^{N_v^h}$:

$$\varphi_h(\mathbf{r}) = \sum_{k=1}^{N_v^h} \varphi_k^h w_k(\mathbf{r}) \quad \forall \mathbf{r} \in \Omega \,. \tag{4.2.7}$$

The coefficients $\{\varphi_k^h\}$ correspond to the function values at the nodal points.

4.2.2 FE space for vector functions: U_h

As we previously discussed in Sec. 4.1, maintaining the stability of the variational problem hinges on selecting finite element spaces W_h and U_h that satisfy the Ladyzhenskaya–Babuška–Brezzi (LBB) condition. Given our choice of W_h as the space of piecewise trilinear continuous functions, a sufficient stability criterion is ensuring that the gradient space ∇W_h is contained within U_h.[3] To achieve this, we define U_h as the space of lowest-order Nédélec edge elements of the first kind.[9,10] These elements are particularly well-suited for problems involving vector fields because they

---

[9] Jean-Claude Nédélec. "Mixed finite elements in $\mathbb{R}^3$", 35pp. 315–341, 1980.

[10] Jean-Claude Nédélec. "A new family of mixed finite elements in $\mathbb{R}^3$", 50pp. 57–81, 1986.

enforce continuity of the tangential component across element interfaces while allowing normal discontinuities, a key requirement for accurately representing fields like the electric displacement or magnetic flux.
Formally, the space U_h consists of piecewise polynomials that are linear in two variables but constant in the third, ensuring that each component of $\mathbf{u}$ conforms to the prescribed structure:

$$\begin{aligned} U_h = \{\mathbf{u} = (u_1, u_2, u_3) \in (L^2(\Omega))^3 :& \\ u_1|_{K_t} \in \mathbb{P}_{0,1,1}(K_t),\ u_2|_{K_t} \in \mathbb{P}_{1,0,1}(K_t),\ u_3|_{K_t} \in \mathbb{P}_{1,1,0}(K_t),\ \forall K_t \in \mathcal{T}_h\}& \end{aligned} \tag{4.2.8}$$

This choice ensures that U_h provides the necessary flexibility for capturing vector field variations while preserving the compatibility required by the finite element discretization.
To construct a practical basis for this space, we employ functions derived from first-degree Whitney elements.[11] These basis functions, denoted as $\{\boldsymbol{\sigma}_j\}_{j=1}^{N_e^h}$, are specifically designed to maintain the essential properties of edge elements, such as preserving the tangential continuity across element boundaries. Choose an element K_t, the explicit form follows of the twelve basis associated to the edges are:[12]

$$\boldsymbol{\sigma}_j(\mathbf{r}) = \begin{cases} l_a(y) l_b(z)\,\hat{\mathbf{x}} & j \text{ on } x\text{-axis} \\ l_a(x) l_b(z)\,\hat{\mathbf{y}} & j \text{ on } y\text{-axis} \\ l_a(x) l_b(y)\,\hat{\mathbf{z}} & j \text{ on } z\text{-axis} \end{cases} \qquad a, b = -1, 1 \tag{4.2.9}$$

where $l_a(\nu)$ represents the linear polynomials associated with the edge nodes, as defined in Eq. (4.2.6).
Within the reference element $\hat{K}$, these basis functions are associated with the 12 edges of the element, and they are illustrated in Fig. 4.2. Unlike the nodal basis functions in W_h, which are naturally tied to vertices, these edge-based functions inherently respect the rotational degrees of freedom of vector fields. This makes them a crucial component in constructing stable and physically meaningful approximations of vector fields in our finite element formulation.

By choosing Nédélec elements for U_h and trilinear elements for W_h, we ensure a robust and stable discretization that aligns well with the mathematical structure of our problem. This combination not only satisfies the necessary stability conditions but also facilitates accurate numerical approximations, paving the way for reliable simulations.

---

[11] Hassler Whitney. *Geometric Integration Theory*. Princeton, N. J.: Princeton University Press, 1957.

[12] Wei Cai. In: "Computational Methods for Electromagnetic Phenomena: electrostatics in solvation, scattering, and electron transport". Pp. 205–227. Cambridge University Press, 2013.

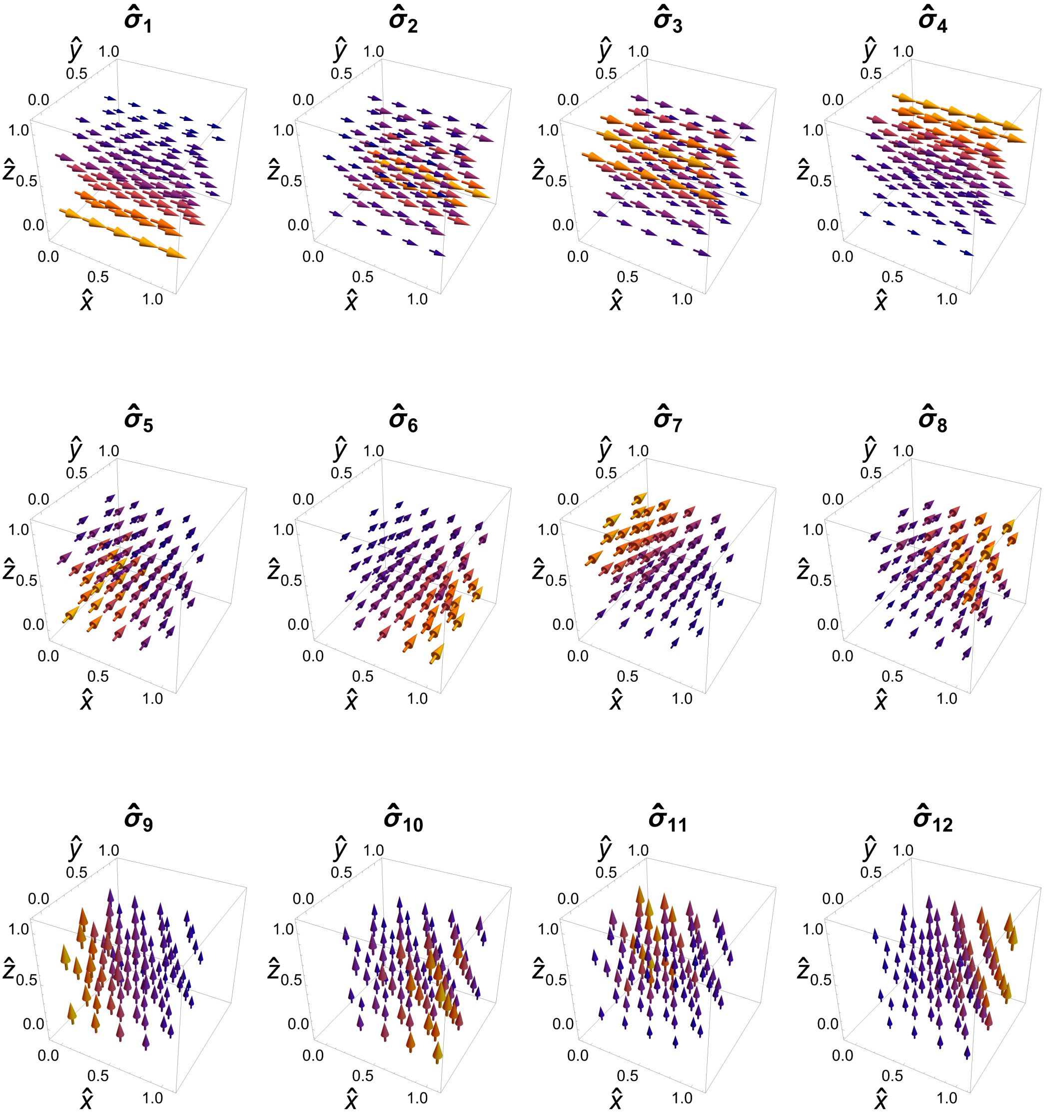

FIGURE 4.2: Edge fuction basis on the reference element $\hat{K}$.

4.3 Matrix Formulation

The structure and bandwidth of the matrices in (4.1.8) can be significantly simplified by approximating the integrals in (4.1.2) using low-order quadratures. To achieve a practical yet accurate system representation, we now derive the matrix elements within the PM formulation, ensuring a balance between computational efficiency and fidelity to the underlying physics.
Having established the finite element spaces U_h and W_h, we now focus on computing the matrix elements in the PM formulation. Our goal is to construct a system that balances computational efficiency with fidelity to the underlying physics.

4.3.1 Element Matrices

We begin by considering a single element K_t in the finite element mesh:

$$K_t = \{(x,y,z) \in \mathbb{R}^3 : x_t \leq x \leq x_{t+i},\ y_t \leq y \leq y_{t+i},\ z_t \leq z \leq z_{t+i}\} \in \mathcal{T}_h \ .$$

Within each element, the matrix entries are derived from the integrals:

$$\begin{aligned} a_{ij} &= \int_{K_t} \frac{1}{\varepsilon} \boldsymbol{\sigma}_i \cdot \boldsymbol{\sigma}_j \mathrm{d}x\, \mathrm{d}y\, \mathrm{d}z \quad \forall i,j = 1,\dots,12 \\ b_{ik} &= \int_{K_t} \boldsymbol{\sigma}_i \cdot \nabla w_k \mathrm{d}x\, \mathrm{d}y\, \mathrm{d}z \quad \forall i = 1,\dots,12,\ k = 1,\dots,8 \end{aligned} \tag{4.3.1}$$

While these integrals can be computed exactly using the basis functions defined in Sec. 4.2, practical implementations favor numerical quadrature for efficiency. Given our hexahedral element, a natural choice is the three-dimensional trapezoidal rule, which approximates integrals over an element K_t with dimensions $h_x = x_{t+1} - x_t$, $h_y = y_{t+1} - y_t$ and $h_z = z_{t+1} - z_t$ as:

$$\int_{K_t} F(x,y,z)\mathrm{d}V = \int_{x_t}^{x_{t+1}} \int_{y_t}^{y_{t+1}} \int_{z_t}^{z_{t+1}} F(x,y,z)\mathrm{d}x\, \mathrm{d}y\, \mathrm{d}z \simeq Q_{K_t}(F) \tag{4.3.2}$$

where the quadrature operator $Q_{K_t}(F)$ is defined as:

$$\begin{aligned} Q_{K_t}(F) = &\frac{h_x h_y h_z}{8} [F(x_t,y_t,z_t) + F(x_{t+1},y_t,z_t) + F(x_t,y_{t+1},z_t) + F(x_t,y_t,z_{t+1}) + \\ &F(x_{t+1},y_{t+1},z_t) + F(x_t,y_{t+1},z_{t+1}) + F(x_{t+1},y_t,z_{t+1}) + F(x_{t+1},y_{t+1},z_{t+1})] \ . \end{aligned} \tag{4.3.3}$$

This choice significantly simplifies the evaluation of element matrices and naturally leads to a diagonal structure for $\tilde{A}$. For a given edge j within element K_t, the corresponding diagonal entry is:

$$a_{jj}|_{K_t} = \int_{K_t} \frac{1}{\varepsilon}\boldsymbol{\sigma}_j \cdot \boldsymbol{\sigma}_j \mathrm{d}V \simeq Q_{K_t}(\frac{1}{\varepsilon}\boldsymbol{\sigma}_j \cdot \boldsymbol{\sigma}_j) = \frac{h_x h_y h_z}{8}\left[\frac{1}{\varepsilon_k} + \frac{1}{\varepsilon_n}\right] , \tag{4.3.4}$$

where $\varepsilon_k = \varepsilon(\mathbf{r}_k)$ and $\varepsilon_n = \varepsilon(\mathbf{r}_n)$ are the permittivity values at the two nodes defining the edge j.

The matrix B is not diagonal, however it remains sparse. Fixed an edge j, the only nonzero entries correspond to its two endpoint nodes, k and n. So the integrals over K_t are:

$$b_{jk} \simeq \sum_a Q_{K_a}(\boldsymbol{\sigma}_j \cdot \nabla w_k) = -\frac{\mathcal{A}_j}{4} \tag{4.3.5}$$

$$b_{jn} \simeq \sum_a Q_{K_a}(\boldsymbol{\sigma}_j \cdot \nabla w_n) = \frac{\mathcal{A}_j}{4} \tag{4.3.6}$$

where $\mathcal{A}_j$ represents the area of the face of K_t perpendicular to edge j.

4.3.2 Static Condensation

We can take advantage of the simple form of $\tilde{A}$ to reduce the total number of unknowns in the systems via a Schur–complement approach (often referred to as *static condensation* in the jargon of Finite Elements practitioners.[13]) Indeed, solving the first row of (4.1.8) for $\mathbf{D}^h$ we get

$$\mathbf{D}^h = -\tilde{A}^{-1}B^T\boldsymbol{\phi}^h \tag{4.3.7}$$

and plugging the latter into the second row

$$\left[-B\left(\tilde{A}^{-1}B^T\right) - C\right]\boldsymbol{\phi}^h = A\,\boldsymbol{\phi}^h = -\boldsymbol{R}. \tag{4.3.8}$$

Using this formulation, we can express the dielectric displacement along edge $j = \{k, n\}$ as:

$$D_j^k = -(a_{jj}^{-1}b_{jk}\phi_k^h + a_{jj}^{-1}b_{jn}\phi_n^h) = -\tilde{\varepsilon}_{kn}\frac{\phi_n - \phi_k}{h_{kn}} \tag{4.3.9}$$

---

[13] Olgierd Cecil Zienkiewicz et al. *The finite element method*. Vol. 3. McGraw-Hill, 1977.

where h_{kn} is the edge length and $\tilde{\varepsilon}_{kn}$ is the harmonic average of the permittivity values:

$$\tilde{\varepsilon}_{kn} = 2\frac{\varepsilon_k \varepsilon_n}{\varepsilon_k + \varepsilon_n} \,.$$

The final system matrix A, obtained from the static condensation of equation (4.3.8), exhibits a symmetric structure. For a single element K_t, it takes the form:

$$A|_{K_t} = \begin{bmatrix} D_{11} & \mathcal{E}_{12} & \mathcal{E}_{13} & 0 & \mathcal{E}_{15} & 0 & 0 & 0 \\ \mathcal{E}_{21} & D_{22} & 0 & \mathcal{E}_{24} & 0 & \mathcal{E}_{26} & 0 & 0 \\ \mathcal{E}_{31} & 0 & D_{33} & \mathcal{E}_{34} & 0 & 0 & \mathcal{E}_{37} & 0 \\ 0 & \mathcal{E}_{42} & \mathcal{E}_{43} & D_{44} & 0 & 0 & 0 & \mathcal{E}_{48} \\ \mathcal{E}_{51} & 0 & 0 & 0 & D_{55} & \mathcal{E}_{56} & \mathcal{E}_{57} & 0 \\ 0 & \mathcal{E}_{62} & 0 & 0 & \mathcal{E}_{65} & D_{66} & 0 & \mathcal{E}_{68} \\ 0 & 0 & \mathcal{E}_{73} & 0 & \mathcal{E}_{75} & 0 & D_{77} & \mathcal{E}_{78} \\ 0 & 0 & 0 & \mathcal{E}_{84} & 0 & \mathcal{E}_{86} & \mathcal{E}_{87} & D_{88} \end{bmatrix} \tag{4.3.10}$$

where:

$$\mathcal{E}_{k\beta} = -\tilde{\varepsilon}_{k\beta} \frac{\mathcal{A}_{k\beta}}{4h_{k\beta}}$$

$$D_{kk} = -\sum_{\beta} \mathcal{E}_{k\beta}$$

with β indexing the nodes connected to k by an edge. The parameters $\tilde{\varepsilon}_{k\beta}$, $h_{k\beta}$ and $\mathcal{A}_{k\alpha}$ represent, respectively, the harmonic average of the permittivity, the edge length, and the corresponding perpendicular face area.

By leveraging the finite element spaces introduced earlier and applying the trapezoidal quadrature rule, our formulation naturally yields the system matrix A in (4.3.8). This matrix correspond to those that would be obtained by taking the *harmonic average* of the permittivity over the edges and applying a standard Finite Element discretization of the problem.[14,15]

While the trapezoidal rule offers a simple and computationally efficient means of integration, it falls short in accurately resolving sharp transitions in permittivity. This limitation becomes particularly significant near the molecular surface, where abrupt dielectric variations critically influence electrostatic interactions. In the following sections, we introduce alternative quadrature strategies that refine the way permittivity is averaged across edges, enhancing accuracy in these challenging regions.

---

[14] Jinchao Xu and Ludmil Zikatanov. "A monotone finite element scheme for convection-diffusion equations", 68pp. 1429–1446, 1999.

[15] Peter A Markowich and Miloš A Zlámal. "Inverse-average-type finite element discretizations of self-adjoint second-order elliptic problems", 51pp. 431–449, 1988.

4.4 Coefficient Discontinuity: equation discretization across the molecular surface

As discussed earlier, we solve the LPBE using an orthogonal cubic FEM, where the electrostatic potential is represented in a first-order Lagrangian basis. In this framework, the potential and related quantities defined at the grid nodes are tri-linearly interpolated at off-grid positions. A direct consequence of this choice is that the interpolated potential varies linearly along grid edges, making the electric field constant along them.

This approach aligns well with the continuum electrostatics model when a grid edge lies entirely within a single medium, either the solute or the solvent. However, challenges arise when an edge crosses the MS, where the dielectric constant changes abruptly. According to continuum electrostatics theory, the potential must remain continuous across the interface, while the normal component of the dielectric displacement must also be conserved. These conditions are well captured by the PM-FEM formulation introduced earlier in this chapter. However, as a consequence, the normal component of the electric field undergoes a step discontinuity, something that simple linear interpolation between adjacent nodes cannot adequately capture. Conventional solutions to this problem can be increasing the grid resolution, possibly locally, using irregular grids to localize the nodes at the discontinuity or changing the shape of the elements so that they better fit that of the MS. All of these solutions, however, entail some increase in the degree of complexity of the method.

In our quest for increased accuracy at low computational impact, we note that the information that we can get from `NanoShaper`[16] is richer than simply telling whether a point is inside or outside the volume enclosed by the MS. We have analytical information related to where exactly the edges intersect the MS, together with the corresponding normal. Our goal is to leverage this information to enhance the way the equation is discretized on the MS-crossing edges. To achieve this, we explore an alternative quadrature rule that naturally emerges from the one-dimensional version of the problem, along with a more physics-based regularization of the discontinuity on intersected edges. Both approaches demonstrate that, for these edges, the most accurate approximation of the dielectric permittivity is given by a weighted harmonic average.

4.4.1 1D Numerical Approach

To better understand the connection between weighted harmonic edge averaging and the primal mixed formulation, we first examine a simplified 1D model of equation (4.1.1) with piecewise constant coefficients:

---

[16] Sergio Decherchi and Walter Rocchia. “A general and Robust Ray-Casting-Based Algorithm for Triangulating Surfaces at the Nanoscale”, 8pp. 1–15, 2013.

$$\begin{cases} -\left(\varepsilon(x)\,\phi'(x)\right)' + c(x)\,\phi(x) = \rho^f(x) & 0 < x < x_{max} \\ \varepsilon(x) = \varepsilon_s\ ,\ c(x) = c & 0 < x < \bar{x} \\ \varepsilon(x) = \varepsilon_m\ ,\ c(x) = 0 & \bar{x} < x < x_{max} \\ \phi(0) = \phi(x_{max}) = 0 & \end{cases} \tag{4.4.1}$$

To discretize this problem, we introduce a uniform triangulation of the domain $\Omega = (0, x_{max})$:

$$\Omega_i \equiv (x_i, x_{i+1}) \quad \text{s.t.} \quad x_i = i \cdot h\ ,\ h = \frac{x_{max}}{N_e^h},\ i = 1, \ldots, N_e^h + 1 = N_v^h\ . \tag{4.4.2}$$

Following the same procedure as in Sec. 4.1, we obtain the linear system:

$$\begin{bmatrix} \tilde{A} & B^T \\ B & -C \end{bmatrix} \begin{bmatrix} \mathbf{D}^h \\ \boldsymbol{\phi}^h \end{bmatrix} = \begin{bmatrix} 0 \\ -\boldsymbol{R} \end{bmatrix}, \tag{4.4.3}$$

where the matrices are given by:

$$\begin{aligned} \tilde{A} &= [a(\sigma_i, \sigma_j)] = [a_{ij}], \quad a_{ij} = \int_\Omega \frac{1}{\varepsilon(x)} \sigma_j(x) \sigma_i(x) \mathrm{d}x \\ B &= [b(\sigma_j, w_k)] = [b_{jk}], \quad b_{jk} = \int_\Omega \sigma_j(x) w_k'(x) \mathrm{d}x \\ C &= [\kappa(w_k, w_n)] = [c_{kn}],\ c_{kn} = \int_\Omega c(x) w_k w_n \mathrm{d}x \\ \boldsymbol{R} &= \left[\int_\Omega \rho^f w_k \mathrm{d}x\right] \end{aligned} \tag{4.4.4}$$

Since the discontinuity at $\bar{x}$ does not necessarily align with a mesh node, we assume that there exists an index $j \in [1, N_e^h]$ such that $x_j < \bar{x} < x_{j+1}$, and introduce the parameter $\alpha \in (0, 1)$ as:

$$\bar{x} = \alpha h + x_j = x_{j+1} - (1 - \alpha) h \tag{4.4.5}$$

On the above defined triangulation let us define the corresponding one-dimensional FE spaces:

$$W_h = \{v \in C^0(\bar{\Omega}) : v(0) = v(x_{max}) = 0,\ v|_{\Omega_i} \in \mathbb{P}_1(\Omega_i)\} = \text{Span}\{w_i(x)\}_{i=1}^{N_v^h}, \tag{4.4.6}$$

$$U_h = \text{Span}\{\sigma_j\}_{j=1}^{N_e^h}, \qquad \sigma_j = \chi_{\bar{\Omega}_j},\ j = 1, \ldots, N_e^h\ , \tag{4.4.7}$$

where the basis functions defined in (4.4.6) and (4.4.7) are depicted in Fig. 4.3a and Fig. 4.3b, respectively.

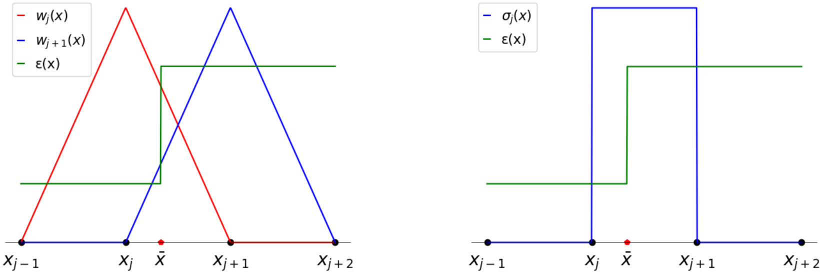

(A) $w_j(x)$

(B) $\sigma_j(x)$

FIGURE 4.3: One-dimensional basis functions.

With this choice of basis functions, the matrix $\tilde{A}$ remains diagonal, and each row of B has nonzero elements corresponding to the nodes defining the respective edge. However, in this case, we can easily compute the integrals exactly. Starting from $\tilde{A}$, if the element j does not have the discontinuity the integral over the element becomes:

$$a_{jj} = \int_{\Omega_j} \frac{1}{\varepsilon_j} \sigma_j(x) \sigma_j(x) \mathrm{d}x = \frac{h}{\varepsilon_j} \,, \tag{4.4.8}$$

where ε_j is equal to ε_m if j in on the right w.r.t. $\bar{x}$ and is equal to ε_s if j in on the left w.r.t. $\bar{x}$.

The interesting case is, indeed, when the computation is performed in element where the discontinuities in the coefficients actually occur:

$$a_{jj} = \int_{\Omega_j} \frac{1}{\varepsilon(x)} \sigma_j(x) \sigma_j(x) \mathrm{d}x = h \left(\frac{\alpha}{\varepsilon_s} + \frac{1-\alpha}{\varepsilon_m} \right) = h \left(\frac{\alpha \varepsilon_m + (1-\alpha)\varepsilon_s}{\varepsilon_m \varepsilon_s} \right) \,. \tag{4.4.9}$$

For the element of the matrix B, fixed the element j, the non-zero elements are:

$$b_{jk} = -1 \,, \quad b_{jn} = 1 \tag{4.4.10}$$

where k and n are the left and right nodes of the edge j, respectively.

So the dielectric displacement is:

$$D_j = \begin{cases} -\varepsilon_j \phi_h'|_{\Omega_j} = -\varepsilon_j \dfrac{\phi_n - \phi_k}{h} & \text{if } \bar{x} \notin (x_k, x_n) \\ -\bar{\varepsilon}\phi_h'|_{\Omega_j} = -\dfrac{\varepsilon_m \varepsilon_s}{\alpha\varepsilon_m + (1-\alpha)\varepsilon_s} \dfrac{\phi_n - \phi_k}{h} & \text{if } \bar{x} \in (x_k, x_n) \end{cases} \tag{4.4.11}$$

Not surprisingly, if $\bar{x} \notin (x_k, x_n)$, the dielectric displacement vector equals the permittivity multiplied by the electric field. However, if $\bar{x} \in (x_k, x_n)$, the dielectric displacement equals the electric field times a *weighted harmonic average* of the permittivity:

$$\bar{\varepsilon} = \frac{1}{\int_{\Omega_j} \varepsilon(x)} = \frac{\varepsilon_m \varepsilon_s}{\alpha\varepsilon_m + (1-\alpha)\varepsilon_s} \tag{4.4.12}$$

In the above derivations, we computed integrals exactly, which is feasible in this case due to the piecewise constant nature of the coefficients. However, in more general settings, numerical quadrature is required. To this end, let us introduce the following quadrature formula to approximate integrals over an interval of size h of functions which display a discontinuity at point at a distance αh from the first end of the interval:

$$\int_a^b F(x)\mathrm{d}x \simeq \alpha h F(a) + (1-\alpha)hF(b) =: Q_{(a,b),\alpha}(F). \tag{4.4.13}$$

Notice that $Q_{(a,b),\alpha}(F)$ is exact for piecewise constant functions and coincides with the trapezoidal rule when $\alpha = 1/2$. Indeed we can generalize (4.3.2) by assuming $\alpha = 1/2$ when no discontinuity occurs in (a, b). Using this quadrature formula, we obtain the same results which we obtain by the exact integration.

4.4.2 Physics-Based Approach

Let's consider two adjacent nodes, *1* and *2* along a given MS-crossing edge and let's call *0* the point where the edge intersects the MS. Let's then consider the two first-order Taylor expansions of the potential centered at the point of intersection along that edge. One expansion holds in medium *1*, while the other in medium *2*:

$$\phi(\mathbf{r}_1) = \phi(\mathbf{r}_0^-) + \mathrm{E}_\nu(\mathbf{r})\Big|_{\mathbf{r}_0^-} (r_1^\nu - r_0^{\nu,-}) + O((\mathbf{r}_1 - \mathbf{r}_0)^2) \tag{4.4.14}$$

$$\phi(\mathbf{r}_2) = \phi(\mathbf{r}_0^+) - \mathrm{E}_\nu(\mathbf{r})\Big|_{\mathbf{r}_0^+} (r_2^\nu - r_0^{\nu,+}) + O((\mathbf{r}_2 - \mathbf{r}_0)^2), \tag{4.4.15}$$

where $\mathbf{r}_0$ is the exact position of the intersection, $\mathbf{r}_1$ and $\mathbf{r}_2$ are the positions of the nodes, ν is the coordinate direction of the edge and E_ν is the $\nu-$component of the electric field. The symbols $\mathbf{r}_0^-$ and $\mathbf{r}_0^+$ denote the position's limit values as they approach the surface from the two different media and coincide.

The electric field at the intersection point can be written as the sum of the vector components normal and tangential to the MS. The electric field at the MS is not continuous, but it can be conveniently represented as the sum of its tangential component vector, which is continuous, and of the normal component vector of the electric displacement, also continuous, divided by the local dielectric constant:

$$\mathbf{E}(\mathbf{r}_0^{\pm}) = \mathbf{E}_t(\mathbf{r}_0) + \frac{\mathbf{D}_n(\mathbf{r}_0)}{\varepsilon(\mathbf{r}_0^{\pm})} \,. \tag{4.4.16}$$

By denoting with α the edge fraction in medium *1*, we obtain $r_1^{\nu} - r_0^{\nu,-} = -h_{\nu}\alpha$ and $r_2^{\nu} - r_0^{\nu,-} = h_{\nu}(1-\alpha)$, where h_{ν} is the length of the edge in the direction ν. The continuity of ϕ ensures $\phi(\mathbf{r}_0^-) = \phi(\mathbf{r}_0^+) = \phi(\mathbf{r}_0)$. Moreover, $\varepsilon(\mathbf{r}_0^-) = \varepsilon_1$ and $\varepsilon(\mathbf{r}_0^+) = \varepsilon_2$. If we now subtract term by term Eq. 4.4.15 from 4.4.14 while keeping only the linear terms and divide both sides by h, we obtain the expression for the incremental ratio of the potential with respect to the grid spacing, which in normal conditions of uniform medium, is the finite difference approximation of the electric field:

$$-\frac{\phi(\mathbf{r}_2) - \phi(\mathbf{r}_1)}{h_{\nu}} = E_{t\nu}(\mathbf{r}_0) + \frac{D_{n\nu}(\mathbf{r}_0)}{\varepsilon^{eff}} =: \mathrm{E}_{\nu}^{eff} \,, \tag{4.4.17}$$

where ε^{eff} takes the form of the WHA of ε_1 and ε_2:

$$\varepsilon^{eff} = \frac{1}{\dfrac{\alpha}{\varepsilon_1} + \dfrac{(1-\alpha)}{\varepsilon_2}} = \bar{\varepsilon} \,. \tag{4.4.18}$$

While harmonic averages have already been used in FEM at the crossing of a discontinuity,[2,3] this derivation provides a robust physical interpretation, going beyond the intuitive representation of a series of two capacitors, and a more accurate expression in terms of a WHA.

Thus, $\mathbf{E}^{eff}$ is the electric field corresponding to the correct voltage drop between $\mathbf{r}_1$ and $\mathbf{r}_2$, its tangential component equals that of the actual electric field at $\mathbf{r}_0$. The corresponding effective electric displacement is

$$\mathbf{D}^{eff} := \bar{\varepsilon}\mathbf{E}^{eff} = \mathbf{D}_n(\mathbf{r}_0) + \bar{\varepsilon}\mathbf{E}_t(\mathbf{r}_0) \,. \tag{4.4.19}$$

its normal component equals that of the actual electric displacement at $\mathbf{r}_0$. This construction provides a convenient expression for the dielectric constant to be used in the solution scheme, with an expression which is only slightly more complex than the conventional one and tends to it when α tends to 0 or to 1.

Moreover, if we assume to know $\phi(\mathbf{r}_1)$ and $\phi(\mathbf{r}_2)$, we can derive an interesting expression for the potential located exactly at the intersection with the surface:

$$\begin{aligned}\phi(\mathbf{r}_0) &= (1-\alpha)\phi(\mathbf{r}_1) + \alpha\phi(\mathbf{r}_2) + (1-\alpha)\alpha h_\nu D_{n\nu}\left(\frac{1}{\varepsilon_2} - \frac{1}{\varepsilon_1}\right) \approx \\ &\approx \phi(\mathbf{r}_1) + \frac{\alpha}{\varepsilon_1} \cdot \frac{\phi(\mathbf{r}_2) - \phi(\mathbf{r}_1)}{\dfrac{\alpha}{\varepsilon_1} + \dfrac{(1-\alpha)}{\varepsilon_2}} \,.\end{aligned} \tag{4.4.20}$$

Expression in Eq. 4.4.20 descends from the following quite reasonable approximation: $D_{n\nu} \approx D_{n\nu}^{eff}$. In the next Chapter, we will benchmark this choice by comparing the surface potential and the ionic energy, which depends on it, against analytical values on single and multiple-sphere systems.

4.5 Weigted Harmonic Average in Primal Mixed FEM

As discussed in Sec. 4.4, a key challenge arises when the dielectric permittivity ε exhibits discontinuities that intersect the edges of mesh elements. A possible approach is to enforce a WHA of ε based on the fractions of the edge that lie inside and outside the molecule. This technique provides a physically informed and numerically robust treatment of permittivity jumps at the discrete level.

In the context of lowest-order Nédélec finite elements, using a basic quadrature rule such as the trapezoidal rule naturally leads to the classical harmonic average (see Sec. 4.3). While this is often adequate, it can fail to capture the influence of highly heterogeneous media. The flexibility of the PMFEM framework allows us to go beyond this limitation by tailoring the quadrature used in assembling the local matrix $\tilde{A}$, enabling more precise integration over discontinuous media.

Recall that the trapezoidal rule used to evaluate integrals over the reference element K_t can be directionally decomposed. For a given Cartesian direction $\nu \in \{x, y, z\}$, we can express the rule as a sum of one-dimensional quadrature contributions along the edges of K_t aligned with ν:

$$Q^{\nu}_{K_t}(F) = \frac{\mathcal{A}_\nu}{4} \sum_{e_\nu=1}^{4} Q_{e_\nu}(F) \,, \tag{4.5.1}$$

where e_ν indexes the four edges of K_t aligned with direction ν, $\mathcal{A}_\nu$ is the area of the face of K_t perpendicular to direction ν, and $Q_{e_\nu}(F)$ represents the 1D trapezoidal rule applied along edge e_ν.

Inspired by the one-dimensional approach to permittivity discontinuity (Eq. (4.4.13)), we now adapt the quadrature along each edge by introducing a weighted-inspired scheme. Specifically, we define a new quadrature:

$$Q^{\nu}_{K_t}(F) = \frac{\mathcal{A}_\nu}{4} \sum_{e_\nu=1}^{4} Q_{e_\nu,\alpha_{e_\nu}}(F) \, , \tag{4.5.2}$$

where the weighted edge-based quadrature is given by:

$$Q_{e_\nu,\alpha_{e_\nu}}(F) = h_\nu [\alpha_{e_\nu} F(\mathbf{r}_k) + (1-\alpha_{e_\nu}) F(\mathbf{r}_n)] \, . \tag{4.5.3}$$

Here, $\mathbf{r}_k$ and $\mathbf{r}_n$ are the vertices of edge e_ν, and $\alpha_{e_\nu} \in [0,1]$ encodes the geometric fraction of the edge lying in each medium, enabling the integration to respect the physical discontinuity in ε. In the absence of any intersection (i.e., the edge is wholly contained in one region), we recover the standard trapezoidal rule (Eq. (4.3.2)) by taking $\alpha_{e_\nu} = \frac{1}{2}$.

With this refined quadrature, we can update the entries of the local stiffness matrix accordingly. For an element K_t and an edge j aligned with direction ν, the corresponding diagonal entry of the local matrix $\tilde{A}$ becomes:

$$a_{jj}|_{K_t} = \int_{K_t} \frac{1}{\varepsilon} \boldsymbol{\sigma}_j \cdot \boldsymbol{\sigma}_j \, \mathrm{d}V \simeq Q^{\nu}_{K_t}(\frac{1}{\varepsilon} \boldsymbol{\sigma}_j \cdot \boldsymbol{\sigma}_j) = \frac{h_x h_y h_z}{4} \left[\frac{\alpha_j}{\varepsilon_k} + \frac{1-\alpha_j}{\varepsilon_n} \right] \tag{4.5.4}$$

where ε_k and ε_n are the dielectric values on either side of the edge, and $h_x h_y h_z$ is the volume of K_t.

The corresponding dielectric displacement along edge j becomes:

$$D^k_j = -(a^{-1}_{jj} b_{jk} \phi^h_k + a^{-1}_{jj} b_{jn} \phi^h_n) = -\bar{\varepsilon}_{kn} \frac{\phi_n - \phi_k}{h_{kn}} \tag{4.5.5}$$

where $\bar{\varepsilon}_{kn}$ is the WHA of the nodal dielectric constants across the edge between k and n:

$$\bar{\varepsilon}_{kn} = \frac{\varepsilon_k \varepsilon_n}{\alpha_j \varepsilon_n + (1-\alpha_j)\varepsilon_k}$$

After applying static condensation, the global matrix A maintains the same sparsity pattern as in Eq. (4.3.10), but its entries now encode the WHA-corrected dielectric properties:

$$\mathcal{E}_{k\beta} = -\bar{\varepsilon}_{k\beta} \frac{\mathcal{A}_{k\beta}}{h_{k\beta}} \, . \tag{4.5.6}$$

We will refer to this formulation as the *Weighted Harmonic Average Primal Mixed Finite Element Method* (WHA-PMFEM).

4.5.1 Standard FE with WHA of the permittivity

Interestingly, the benefits of WHA are not limited to PMFEM. The same strategy can be applied in the classical continuous Galerkin framework via the so-called *Edge-Averaged Finite Element* (EAFE) method.[14]

To see this, we now apply a standard first-order continuous finite element discretization to the LPBE (2.5.15):

$$\begin{aligned}&\text{Find } \phi_h \in W_h, \textit{ s.t.}\\ &\int_\Omega \varepsilon \nabla \phi_h w_i \mathrm{d}V + \int_\Omega \kappa^2 \phi_h w_i \mathrm{d}V = \int_\Omega \rho^f w_i \mathrm{d}V, \qquad i = 1, \dots, N_v^h.\end{aligned} \tag{4.5.7}$$

where w_i are the standard nodal basis functions (cf. Eq. (4.2.5)). Expanding the solution as

$$\phi_h(\mathbf{r}) = \sum_{j=1}^{N_v^h} \phi_j \, w_j(\mathbf{r}),$$

and inserting this into Eq. (4.5.7) yields:

$$\sum_{j=1}^{N_v^h} \phi_j \int_\Omega \varepsilon \nabla w_j \nabla w_i \mathrm{d}V + \sum_{j=1}^{N_v^h} \phi_j \int_\Omega \kappa^2 w_j w_i \mathrm{d}V = \int_\Omega \rho^f w_i \mathrm{d}V, \quad i = 1, \dots, N_v^h. \tag{4.5.8}$$

This system can be compactly written in matrix form as:

$$(M + C) \, \boldsymbol{\phi^h} = R, \tag{4.5.9}$$

where the stiffness matrix $M = [m_{ij}]$ has entries

$$m_{ij} = \int_\Omega \varepsilon \nabla w_j \cdot \nabla w_i \, \mathrm{d}V$$

and C collects the mass-like contributions from the reaction term.

Using the trapezoidal quadrature rule, we find that the structure of M is analogous to the PMFEM matrix A in Eq. (4.3.10), but with scalar basis gradients replacing edge basis functions. In particular, we obtain:

$$\begin{aligned}\mathcal{E}_{k\beta} &= -\hat{\varepsilon}_{k\beta} \frac{\mathcal{A}_{k\beta}}{4h_{k\beta}}\\ D_{kk} &= -\sum_\beta \mathcal{E}_{k\beta}\end{aligned}$$

where β ranges over nodes adjacent to k, and the coefficient $\hat{\varepsilon}_{k\beta}$ denotes the arithmetic mean of nodal permittivities:

$$\hat{\varepsilon}_{k\beta} = \frac{\varepsilon_k + \varepsilon_\beta}{2} .$$

In the EAFE method, this arithmetic average is replaced with an edge-based average, ideally, the same weighted harmonic average $\bar{\varepsilon}_{ij}$ introduced earlier. The resulting matrix is assembled as:

$$M_{AEFE} = [m_{ij,\ AEFE}], \qquad m_{ij,\ AEFE} = \hat{\varepsilon}_{ij} \int_\Omega \nabla w_j \nabla w_i \mathrm{d}V . \tag{4.5.10}$$

By adopting $\hat{\varepsilon}_{ij} = \bar{\varepsilon}_{ij}$, the stiffness matrix constructed via EAFE matches the matrix A obtained from PMFEM after static condensation and WHA quadrature in Eq. (4.5.2). This highlights a deep consistency between the two approaches, despite their differing formulations.

4.6 Treatment of Point Sources

In Eq. (4.1.1), the distribution of fixed charges ρ^f is expressed as a linear combination of Dirac delta functions:

$$\rho^f(\mathbf{r}) = \sum_{i=1}^{N} q_i \delta(\mathbf{r} - \mathbf{r}_i) = \sum_{i=1}^{N} \rho_i^f(\mathbf{r}) , \tag{4.6.1}$$

where q_i and $\mathbf{r}_i$ denote the charge and position of the i-th atom, respectively. These point sources introduce singularities in the analytical solution of the PBE, presenting a significant challenge for numerical methods. To address this issue, two primary strategies are typically employed:

- **Smoothed Charge Representation**: Instead of modeling atomic charges as singular points, they are represented as continuous charge distributions with compact support.[17,18]
- **Regularized Reformulation**: In this approach, the point sources are removed from the domain and their effects are incorporated via a surface charge density, defined either on Γ or on $\partial\Omega$. Many methods in this category leverage explicit Green's function solutions of the LBPE operator, as reviewed in Ref. [19].

---

[17] Anna-Karin Tornberg and Björn Engquist. "Numerical approximations of singular source terms in differential equations", 200pp. 462–488, 2004.

[18] Bamdad Hosseini, Nilima Nigam, and John M. Stockie. "On regularizations of the Dirac delta distribution", 305pp. 423–447, 2016.

[19] Arum Lee, Weihua Geng, and Shan Zhao. "Regularization methods for the Poisson-Boltzmann equation: comparison and accuracy recovery". *Journal of Computational Physics* 426, p. 109958, 2021..

Both strategies are effective in mitigating singularities, and the choice between them depends on the problem formulation and the computational framework. In our case, we adopt the first strategy. The implementation details are described below.
Since we employ a finite element discretization to solve the LPBE, the most natural way to define a continuous charge distribution with compact support is by expressing it as a linear combination of finite element shape functions (4.2.7). In particular, we use first-order continuous Lagrangian basis functions, each associated with a degree of freedom located at a mesh vertex. Consequently, the smoothed charge density $\rho^f_{i,h}(\mathbf{r})$ associated with the i-th atom can be defined as:

$$\rho^f_{i,h}(\mathbf{r}) := \sum_{k=1}^{N_v^h} w_k(\mathbf{r}) q_{i,k} \tag{4.6.2}$$

where $q_{i,k}$ denotes the nodal value of the i-th atomic charge at node k.
A key requirement for the nodal coefficients $q_{i,k}$ is that they must preserve the total charge. This implies:

$$\int_\Omega \rho^f_{i,h}(\mathbf{r})\,\mathrm{d}V = \sum_k q_{ik} \int_\Omega w_k(\mathbf{r})\,\mathrm{d}V = q_i\,. \tag{4.6.3}$$

A simple and effective way to satisfy this constraint is to define:

$$q_{i,k} := \frac{q_i w_k(\mathbf{r}_i)}{\int_\Omega w_k(\mathbf{r})\,\mathrm{d}V}\,. \tag{4.6.4}$$

This definition guarantees charge conservation, as shown below:

$$\int_\Omega \rho^f_{i,h}(\mathbf{r})\,\mathrm{d}V = q_i \sum_k \frac{w_k(\mathbf{r}_i) \int_\Omega w_k(\mathbf{r})\,\mathrm{d}V}{\int_\Omega w_k(\mathbf{r})\,\mathrm{d}V} = q_i \sum_k w_k(\mathbf{r}_i) = q_i\,.$$

The final equality holds due to the partition of unity property of the basis functions.
An important feature of the smoothed charge representation in the finite element framework is its local support and physically consistent multipole behavior. Specifically, when using first-order continuous finite elements, each shape function is nonzero only within the elements to which its corresponding node belongs. Consequently, if the atomic center $\mathbf{r}_i$ falls inside an element K_i, only the shape functions associated with the eight vertices of K_i contribute to the smoothed charge distribution $\rho^f_{i,h}(\mathbf{r})$. This results in a compact, efficiently computable support for each atomic charge. In the case of a structured Cartesian mesh with hexahedral elements, this smoothed distribution can be written as:

$$\rho^f_{i,h}(\mathbf{r}) = \frac{q_i}{V_{K_i}} \sum_{k\in K_i} w_k(\mathbf{r}) w_k(\mathbf{r}_i)\,, \tag{4.6.5}$$

where V_{K_i} is the volume of the element K_i containing $\mathbf{r}_i$.

Beyond computational locality, this construction exhibits a highly desirable electrostatic property: the dipole moment of the smoothed charge distribution vanishes with respect to the atomic position $\mathbf{r}_i$. The discrete dipole moment associated with this interpolation is:

$$\mathbf{p} = \frac{q_i}{V_{K_i}} \sum_{k \in K_i} (\mathbf{r}_k - \mathbf{r}_i) w_k(\mathbf{r}_k) w_k(\mathbf{r}_i) = \frac{q_i}{V_{K_i}} \sum_{k \in K_i} (\mathbf{r}_k - \mathbf{r}_i) w_k(\mathbf{r}_i) = 0 \ . \tag{4.6.6}$$

This cancellation arises due to the symmetry of the interpolation functions. If we denote the local coordinates of the element by $(\bar{x}, \bar{y}, \bar{z})$ and label each vertex k by a triple (a, b, c) with $a, b, c \in -1, 1$, then for the Lagrange basis functions l_a, l_b, and l_c we have:

$$(\mathbf{r}_{(a,b,c)} - \bar{\mathbf{r}}) l_a(\bar{x}) l_b(\bar{y}) l_c(\bar{z}) = -(\mathbf{r}_{(-a,-b,-c)} - \bar{\mathbf{r}}) l_{-a}(\bar{x}) l_{-b}(\bar{y}) l_{-c}(\bar{z}) \ .$$

The fact that the electric dipole is zero, is not merely a mathematical curiosity, but it has practical electrostatic consequences. At large distances, the potential generated by a localized charge distribution can be expanded in a multipole series, with the monopole (total charge) dominating, followed by the dipole and then higher-order terms. Since our smoothed representation eliminates the dipole moment, the leading correction to the far-field potential becomes the quadrupole term, which decays faster with distance. This significantly improves the accuracy of the electrostatic potential in regions far from the source, a crucial advantage in biomolecular simulations and long-range electrostatics.

4.7 Electrostatic energy calculation

It is convenient now to recast the energy of a linearized Poisson-Boltzmann system as a sum of three terms, as shown in Eq. (3.1.6):

$$\Delta G = \frac{1}{2} \sum_{i=1}^{N} q_i \left(\phi_{coul}(\mathbf{r}_i) + \phi_{pol}(\mathbf{r}_i) + \phi_{ion}(\mathbf{r}_i) \right) = \Delta G_c + \Delta G_{pol} + \Delta G_{ion} \ .$$

The Coulombic term, deprived of the singularity related to the self-energy, can be calculated analytically as follows:

$$\Delta G_c = \sum_{i=1}^{N_{atoms}} \sum_{j<i} \frac{q_i q_j}{4\pi\varepsilon_m r_{ij}} \tag{4.7.1}$$

where r_{ij} represents the distance between charges i and j.

The two remaining energy terms involve surface integrals, and we address them differently.

4.7.1 The polarization contribution

The polarization contribution to the electrostatic energy can be written as the energy of the fixed point charges i inside the solute subjected to the potential generated by the polarization charges spread over the MS, presented in Eq. (3.2.17):

$$\Delta G_{pol} = \frac{1}{2} \sum_{i=1}^{N_{atoms}} q_i \int_{\Gamma} \frac{\sigma(\tilde{\mathbf{r}})}{4\pi\varepsilon_0 \|\tilde{\mathbf{r}} - \mathbf{r}_i\|} \mathrm{d}S \tag{4.7.2}$$

where $\mathbf{r}_i$ is the position of the charge on the $i-$th atom and σ is the surface polarization charge.

We take advantage of the Gauss law's property to calculate this contribution. In Eq. (4.4.17), we conjecture that the best way to approximate a region where there is a dielectric discontinuity with a region where the dielectric is uniform is to assume that the uniform dielectric takes the WHA form. We therefore use $\mathbf{D}^{eff}$ as the best way to estimate the flux of D_n passing through the MS intersected by a cube. Once we have solved the PBE, we can easily derive, for each MS-intersecting edge, the quantity $\mathrm{D}_{v}^{eff} h^2$, which corresponds to the flux of $\mathbf{D}^{eff}$ through a square orthogonal to the edge.

If we now consider the flux of $\mathbf{D_n}$ through the part of the MS contained in the cube, one can note that an accurate evaluation would require a good knowledge of both D_n and of the local MS shape. But if we apply Gauss law to the space region inside the cube, which is also located between the MS and the square orthogonal to the edge which passes through the intersection, as represented in Fig. 4.4, we can suggest, since in our model there is no free charge located around the MS, the following approximation:

$$\mathrm{D}_{n,v} h^2 |_{square} \approx \iint_{MS \cap cube} D_n dS \, . \tag{4.7.3}$$

By means of this approach, we derive the total polarization charge q_p located on the piece of MS intersecting a cube and concentrate it on the intersection point $\mathbf{r}_p$ between the MS and the grid:

$$q_p \approx \varepsilon_0 \left(\frac{1}{\varepsilon_s} - \frac{1}{\varepsilon_m} \right) \mathrm{D}_{v}^{eff} h^2 \, . \tag{4.7.4}$$

The final calculation takes, therefore, the following form:

$$\Delta G_{pol} = \frac{1}{2} \sum_{i=1}^{N_{atoms}} \sum_{p=1}^{N_{Ic}} \frac{q_i q_p}{4\pi \|\mathbf{r}_p - \mathbf{r}_i\|} \tag{4.7.5}$$

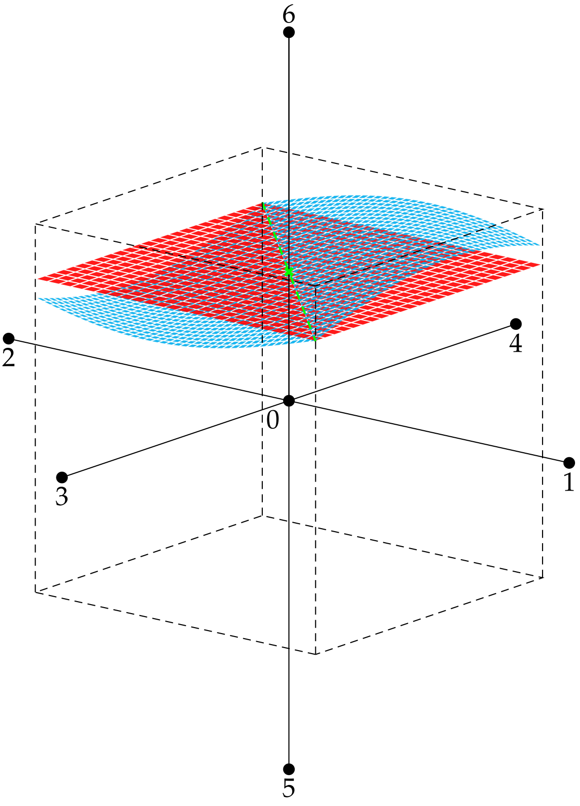

FIGURE 4.4: Black dots represent the "current" node 0 and its six adjacent ones. The green cross represents the intersection between the edge connecting nodes 0 and 6 and the MS (in light blue). The reddish square is the intersection between the cube and the plane orthogonal to the edge and passing through the said intersection. The green dashed line represents the intersection between this plane and the MS.

where N_{Ic} is the total number of cubes intersecting the MS.

4.7.2 Ionic direct contribution calculation

By considering Eqs. (3.2.18) and (3.1.6), one can get the expression for the direct ionic contribution:

$$\Delta G_{ion} = \frac{1}{2}\sum_{i=1}^{N_{atoms}} q_i \left(\int_\Gamma \phi(\tilde{\mathbf{r}}) \frac{(\tilde{\mathbf{r}} - \mathbf{r}_i)\cdot \mathbf{n}(\tilde{\mathbf{r}})}{4\pi \|\tilde{\mathbf{r}} - \mathbf{r}_i\|^3} \mathrm{d}S - \frac{1}{\varepsilon_s} \int_\Gamma \frac{\mathbf{D}(\tilde{\mathbf{r}})\cdot \mathbf{n}(\tilde{\mathbf{r}})}{4\pi \|\tilde{\mathbf{r}} - \mathbf{r}_i\|} \mathrm{d}S \right) \tag{4.7.6}$$

Here, the second integral is equivalent, up to a multiplicative constant, to that in Eq. (4.7.2), and thus is treated similarly.
We now focus on discretizing the first integral of Eq. (4.7.6):

$$I = \int_\Gamma \phi(\tilde{\mathbf{r}}) \frac{(\tilde{\mathbf{r}} - \mathbf{r}_i)\cdot \mathbf{n}(\tilde{\mathbf{r}})}{4\pi \|\tilde{\mathbf{r}} - \mathbf{r}_i\|^3} \mathrm{d}S \ . \tag{4.7.7}$$

To evaluate this integral, we take again the advantage of the information delivered by `NanoShaper`, namely analytical intersections and normals (Fig. 4.5). This is used to locally re-triangulate the surface via the marching cubes algorithm. The total molecular surface is hence approximated as the union of the triangles:

$$\Gamma \approx \bigcup_{j=1}^{N_t} \Gamma_j \tag{4.7.8}$$

where N_t is the number of triangles in the cube grid. Overall, using this information, the integral (4.7.7) can be discretized as follows:

$$I \approx \sum_{j=1}^{N_t} \int_{\Gamma_j} \phi(\tilde{\mathbf{r}}) \frac{(\tilde{\mathbf{r}} - \mathbf{r}_i)\cdot \mathbf{n}(\tilde{\mathbf{r}})}{4\pi \|\tilde{\mathbf{r}} - \mathbf{r}_i\|^3} \mathrm{d}S \approx \sum_{j=1}^{N_t} \frac{T_j}{3} \sum_{k=A,B,C} \phi(\mathbf{r}_k) \frac{(\mathbf{r}_k - \mathbf{r}_i)\cdot \mathbf{n}(\mathbf{r}_k)}{4\pi \|\mathbf{r}_k - \mathbf{r}_i\|^3} \tag{4.7.9}$$

where T_j is the area of the $j-$th triangle and k labels its three vertices. The potentials at the triangle vertices are calculated through the formula (4.4.20). While the type of calculations performed in Sec. 3.2 are quite common in the treatment of elliptic PDEs, we are not aware of any PB solver implementing this solution for the calculation of the ionic contribution to the electrostatic energy.

4.8 Exploiting de-refinement for more efficient BCs

As discussed in Sec. 3.4, even the likely most refined BCs currently in use for Finite Difference and Finite Element Poisson–Boltzmann solvers, often called Coulombic, cannot truly be considered asymptotic. Although they are widely regarded as highly accurate, their precision can still be sensitive to the specific features of the molecular system being modeled. Moreover, their computational cost grows considerably with

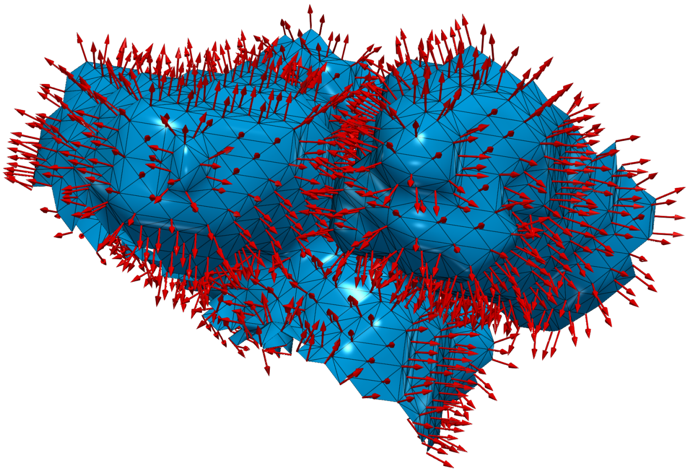

FIGURE 4.5: Triangulation of the MS with normal vectors given by NS.

system size, since evaluating them requires computing distance-based interactions between all atomic charges and each mesh element located on the outer boundary of the domain where the equation is solved.

On the other side, null, homogeneous Dirichlet BCs would, in principle, be exact when applied at an infinitely far distance from the solute regardless of its features. However, using such boundary conditions effectively often requires an excessively large computational domain. This leads to a very low percentage of the mesh being filled by the solute (commonly referred to as the perfil) and consequently, a significant waste of computational resources on degrees of freedom located far out in the solvent, where no meaningful interactions occur.

But numerical advances allow us to rethink this traditional trade-off. In particular, grid adaptivity, which is usually adopted to increase the accuracy in the most critical regions, which in the PB are the point charges and the MS, can just as effectively be applied in the opposite direction, to reduce resolution in the bulk solvent where fine detail is unnecessary. Importantly, while adapting the mesh near complex geometries (like the MS) may introduce technical challenges, applying de-refinement in the more homogeneous solvent region is comparatively straightforward and computationally cheap.

Building on this idea, we propose a strategy that offers an optimal compromise between accuracy and efficiency. We begin by defining a tight computational box closely surrounding the solute, using a high mesh density to achieve a perfil around 90%. Then, we progressively de-refine the mesh beyond this inner region until a much lower perfil is reached, say between 15% and 20%. This allows us to emulate the effect of moving the boundary "to infinity" without actually solving on an enormous uniform grid. It is important to note, however, that our mesh structure is based on an octree of cubic elements. This implies that the total computational domain must be a cube whose side length is a power of two times the smallest grid spacing. As a result, once the inner (finely resolved) box is fixed, the exact overall perfil cannot be explicitly prescribed. Instead, we can only estimate or bound the final perfil, which depends on the extent of the outer, coarser grid levels introduced during de-refinement.

4.9 Software Architecture

The numerical advancements introduced through the WHA-PMFEM and the adaptive local de-refinement strategy are fully integrated into a new open-source solver: `NextGenPB`. This solver is freely available on GitHub at `https://github.com/vdiflorio/NextGenPB` and `https://github.com/concept-lab/NextGenPB`.

From the outset, the guiding principle in designing `NextGenPB` has been *modularity through reuse*. Rather than building every component from scratch, the code strategically leverages high-quality Free Software libraries, wrapping them in abstraction layers that promote extensibility, flexibility, and ease of maintenance. This approach, which provides both interoperability and future-proofing, is directly inherited from `bimpp`, the core C++ library upon which the solver is built.[5,20]

In what follows, we provide an overview of the major components of the code, describing their purpose and the design decisions that shape their implementation.

Data Input The simulation workflow begins with the reading of two key input files:

- the `options.pot` file, which contains all the configuration and simulation parameters;
- and a `.pqr` file, which encodes the 3D molecular structure, including atomic positions, charges, and radii.

These molecular properties are parsed and stored using a class defined in the `NanoShaper` library.[16,21] This class encapsulates all necessary atomic information and serves as the foundation for downstream operations, from surface generation to dielectric mapping.

Surface Creation A precise representation of the molecular surface is central to accurate electrostatic modeling. To this end, `NextGenPB` interfaces directly with the `NanoShaper` library,[16,21] which provides a versatile and efficient set of surface generation algorithms. These include solvent-excluded surfaces (SES), Gaussian surfaces,

---

[20] Carlo de Falco. *bimpp*. `https://www.github.com/bimpp`. Accessed: 2024-12-23.

[21] Sergio Decherchi et al. "NanoShaper–VMD interface: computing and visualizing surfaces, pockets and channels in molecular systems", 35pp. 1241–1243, 2018.

and others. The molecular surface created by `NanoShaper` is seamlessly mapped onto the computational domain and used to define boundary conditions between the MS, such as spatially varying dielectric coefficients. In particular, based on the geometric information extracted from `NanoShaper`, `NextGenPB` identifies the mesh edges that intersect the molecular surface (i.e., the MS-crossed edges). These edges are then selected as candidates for the application of the WHA scheme, enabling an accurate and physically consistent representation of the permittivity jump across the interface.

Adaptive Mesh Creation One of the distinctive features of `NextGenPB` is its use of hierarchically refinable meshes, which enables precise spatial resolution where needed while keeping computational costs under control elsewhere. This adaptive mesh capability is provided through the `bimpp` mesh management class, which internally wraps the highly scalable `p4est` library.[22,23] The Octree-based Cartesian mesh supports local refinement and de-refinement, forming the structural backbone for applying WHA-PMFEM efficiently across complex molecular domains.

Assembly of Matrices and Vectors The discrete operators required by the Poisson–Boltzmann formulation are assembled in parallel using the tools provided by `bimpp`. This includes constructing the system matrix and right-hand-side vector, managing inter-process communication, and organizing data structures across the distributed memory architecture. These components reflect the theoretical framework discussed in Sec. 4.1 and are optimized for high-performance computation.

Solving the Linear System Once the system is assembled, `NextGenPB` provides multiple solver pathways, thanks again to `bimpp`'s abstraction layer. Direct solvers (through `MUMPS`[24,25]) and iterative solvers (via `LIS`[26,27]) are both accessible, depending on the problem size and desired performance characteristics.
In most practical scenarios, the solver of choice is the Conjugate Gradient (CG) method from the `LIS` library, preconditioned with Symmetric Successive Over-Relaxation (SSOR). This combination has demonstrated strong performance and robustness across a wide range of simulations. Unless explicitly stated otherwise, this is the default solver setup used throughout the numerical experiments in the following chapters.

---

[22] Carsten Burstedde, Lucas C. Wilcox, and Omar Ghattas. "`p4est`: Scalable Algorithms for Parallel Adaptive Mesh Refinement on Forests of Octrees", 33pp. 1103–1133, 2011.

[23] Carsten Burstedde and Lucas C. Wilcox amd Tobin Isaac. *p4est: Parallel AMR on Forests of Octrees*. `https://www.p4est.org`. Accessed: 2024-12-10.

[24] P.R. Amestoy, I.S. Duff, and J.-Y. L'Excellent. "Multifrontal parallel distributed symmetric and unsymmetric solvers", 184pp. 501–520, 2000.

[25] Carsten Burstedde and Lucas C. Wilcox amd Tobin Isaac. *MUMPS:MUltifrontal Massively Parallel sparse direct Solver*. `https://www.p4est.org`. Accessed: 2024-12-10.

[26] Akira Nishida. "Experience in Developing an Open Source Scalable Software Infrastructure in Japan". In: *Computational Science and Its Applications – ICCSA 2010*. Ed. by David Taniar et al. Berlin, Heidelberg: Springer Berlin Heidelberg, 2010. Pp. 448–462.

[27] A. Nishida. *Lis: Library of Iterative Solvers for Linear Systems*. `https://www.ssisc.org/lis`. Accessed: 2024-12-10.

Energy Calculations Beyond solving for the electrostatic potential, `NextGenPB` is capable of computing all the relevant energetic contributions associated with the LPB model. Crucially, the code is designed to calculate all energy contributions in a single simulation run, avoiding redundant recomputation. This is accomplished using the procedures outlined in Sec. 4.7, where each term is evaluated separately but efficiently, making full use of the already assembled data structures and potential field. This feature enhances both the performance and user experience of the software, allowing researchers to extract detailed energetic profiles from a single execution without additional configuration or code changes.

Post-Processing data saving To facilitate downstream analysis, `NextGenPB` supports high-performance, parallel data output. Using `bimpp`'s I/O layer and linking to the `liboctave` library,[28] simulation results can be exported in structured binary format compatible with `GNU Octave`. This allows users to leverage existing Octave/Matlab scripts for batch post-processing, visualization, or further numerical analysis.
In addition, the solver supports export in `VTK` format, enabling direct visualization of potentials, charge densities, and dielectric profiles using tools like ParaView. This dual-format support enhances the usability of the code and lowers the barrier for integrating `NextGenPB` into broader computational pipelines.

---

[28] John W. Eaton et al. *GNU Octave version 9.2.0 manual: a high-level interactive language for numerical computations*. 2024.

Chapter 5

Numerical Results

This chapter presents a comprehensive analysis of both the accuracy and computational performance of the proposed solver, benchmarked against widely used methods in biomolecular simulations. The evaluation covers test cases with known analytical solutions as well as realistic biomolecular systems. Additionally, we explore the parallelization efficiency and scalability of our implementation on High-Performance Computing (HPC) platforms.

Unless otherwise specified, the following simulations use a solvent dielectric constant of 80, a solute dielectric constant of 2, an ionic strength of 0.145 mol/L and a temperature of 298.15K.

5.1 Accuracy: Analytically Solvable Systems

To rigorously assess the accuracy of our solver, we compare its results with those obtained using two widely recognized approaches: the finite difference (FD) method implemented in the DelPhi solver,[1] and the second-order accurate method employed by MIBPB.[2,3] These comparisons are grounded in test systems for which analytical solutions to the linearized Poisson–Boltzmann equation (LPBE) are available, particularly many-sphere configurations presented in Chap. 3, based on formulations from [4–8], among others.

---

[1] Lin Li et al. "DelPhi: a comprehensive suite for DelPhi software and associated resources", 5pp. 1–11, 2012.

[2] Y. C. Zhou, Michael Feig, and G. W. Wei. "Highly accurate biomolecular electrostatics in continuum dielectric environments", 29pp. 87–97, 2008.

[3] Duan Chen et al. "MIBPB: A software package for electrostatic analysis", 32pp. 756–770, 2011.

[4] Y.-K. Yu. "Electrostatics of charged dielectric spheres with application to biological systems. III. Rigorous ionic screening at the Debye-Hückel level". *Physical Review E* 102, p. 052404, 2020..

[5] O. I. Obolensky, T. P. Doerr, and Yi-Kuo Yu. "Rigorous treatment of pairwise and many-body electrostatic interactions among dielectric spheres at the Debye-Hückel level". *Eur. Phys. J. E* 44, p. 129, 2021..

[6] S. V. Siryk et al. "Charged dielectric spheres interacting in electrolytic solution: a linearized Poisson-Boltzmann equation model". *J. Chem. Phys.* 155, p. 114114, 2021..

[7] S. Siryk and W. Rocchia. "Arbitrary-Shape Dielectric Particles Interacting in the Linearized Poisson-Boltzmann Framework: An Analytical Treatment". *J. Phys. Chem. B* 126, pp. 10400–10426, 2022..

[8] Y.-K. Yu. "Electrostatics of charged dielectric spheres with application to biological systems. II. A formalism bypassing Wigner rotation matrices". *Physical Review E* 100, p. 012401, 2019..

To ensure fairness and consistency, all solvers are evaluated using identical grid structures and simulation parameters, although the NGPB solver is, by design, more flexible in its meshing strategy.

5.1.1 The Kirkwood Sphere

We begin with a fundamental test case: a single dielectric sphere immersed in an electrolytic medium. This configuration admits an analytical solution to the linearized Poisson–Boltzmann equation (LPBE), making it a valuable benchmark. Although the spherical system can easily be solved analytically, it shares some commonalities with more complex alternatives since its symmetry differs from that of the Cartesian grid on which it is mapped and solved.
As detailed in Sec. 3.3.1 and expressed by Eq. (3.3.15), the analytical solutions for the polarization and ionic energies are:

$$\Delta G_{pol} = \frac{1}{2}\left(\frac{1}{\varepsilon_s} - \frac{1}{\varepsilon_m}\right)\frac{q^2}{4\pi R} \tag{5.1.1}$$

$$\Delta G_{ion} = -\frac{1}{2}\frac{q^2}{4\pi\varepsilon_s}\frac{k_D}{(1+k_D R)} \tag{5.1.2}$$

where q is the point charge placed at the center of the sphere, R is the sphere's radius, and k_D is the inverse Debye length, characterizing the ionic strength of the medium.

Solvers Comparison All solvers operate on a uniform mesh with a grid spacing of 0.5 Åto ensure consistent and comparable results. The computational domain is set such that the sphere occupies approximately 15% of the total volume. The test sphere has a radius of 2 Å and carries a unit charge (1 e.s.u.).
We evaluate and compare the polarization and ionic energies, as well as the electrostatic potential at the sphere's surface, against the analytical reference. Tab. 5.1 summarizes the energy comparison. NGPB consistently outperforms both DelPhi and MIBPB, achieving relative errors at least one order of magnitude smaller for each energy component.
To assess the accuracy of the electrostatic potential at the sphere's surface, we interpolate the potential at any surface point inside a cubical volume using the potential values at the eight vertices employing a trilinear function. Fig. 5.1 presents the results as a box plot. In this plot (and in what will follows):

- The cross marks the mean value,
- The box spans the interquartile range (IQR), representing the central 50% of the data,
- The whiskers extend to include 96% of the values,
- The most extreme 2% on either side are shown as outliers.

The plot highlights NGPB's superior accuracy in reproducing surface potentials, offering not only better mean values but also reduced variance compared to other solvers.

-	Polarization	Ionic	Total
Value $[K_bT]$	-68.31	-0.35	-68.65
Relative error			
NGPB	7.38e-10	3.39e-02	1.72e-04
DelPhi	5.89e-05	-5.98e-01	-2.97e-03
MIBPB	7.16e-03		7.16e-03

TABLE 5.1: Analytical value and signed relative error in energy calculation for NGPB, DelPhi and MIBPB for the Kirkwood sphere. The percentage of box filling is 15%. For MIBPB, we could not identify the energy contributions from the polarization and ionic terms individually, so we report the error for their combined total along with the total energy error.

NGPB Error Convergence The Kirkwood sphere is also particularly well-suited for studying convergence behavior, as it allows us to impose exact analytical boundary conditions on $\partial\Omega$. This removes ambiguity from artificial boundary treatments and isolates the intrinsic accuracy of the numerical scheme.

To quantify convergence, we analyze both the electrostatic potential and energy errors with respect to mesh resolution. For the energy terms, we report the relative percentage error. For the potential, we define two complementary error metrics:

- Nodal error E_{nodes}: measures the average relative error at grid nodes located along edges intersected by the molecular surface:

$$E_{nodes} = 100 \cdot \sum_{k \in \mathcal{K}} \left| \frac{\phi(\mathbf{r}_k) - \phi_a(\mathbf{r}_k)}{\phi_a(\mathbf{r}_k)} \right| . \tag{5.1.3}$$

- Surface error E_{surf}: assesses the error in interpolated potential values directly on the molecular surface using the WHA-based interpolation described in Sec. 4.4.2:

$$E_{surf} = 100 \cdot \sum_{k \in \mathcal{K}} \left| \frac{\phi_s(\mathbf{r}_k) - \phi_a(\mathbf{r}_k)}{\phi_a(\mathbf{r}_k)} \right| \tag{5.1.4}$$

Here, $\mathcal{K}$ denotes the set of nodes on these intersected edges, $\phi_a(\mathbf{r}_k)$ denotes the analytical potential, and ϕ_s denotes the surface-interpolated value—computed using Eq. (4.4.20) for NextGenPB and classical trilinear interpolation for other solvers.

Despite the presence of a dielectric discontinuity, NGPB demonstrates robust and nearly optimal convergence behavior. As shown in Fig. 5.2a, the potential errors (both nodal and surface) exhibit convergence rates between 1.6 and 1.7. Similar rates are observed for the ionic and total energy (Fig. 5.2b). Notably, the polarization energy

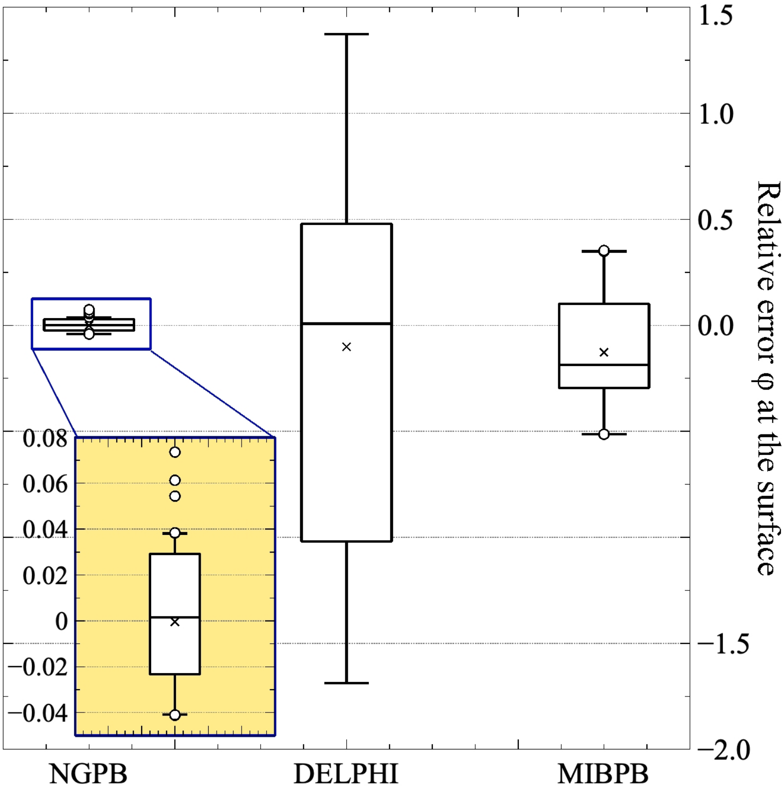

FIGURE 5.1: Box plot of the signed relative error for the electrostatic potential at the surface, comparing NGPB, DelPhi, and MIBPB results against analytical solutions for the Kirkwood sphere. The surface potential is evaluated at the vertices generated by NanoShaper, using Eq. (4.4.20) for NGPB and classical trilinear interpolation for DelPhi and MIBPB.

exhibits even greater stability and accuracy, remaining largely unaffected by grid resolution. This is because the total flux of the electric displacement on the surfaces is calculated with high precision and positioned exactly at the vertices of the triangulated surface.

It is important to note that in the absence of dielectric interfaces or singular sources, linear finite element methods are known to exhibit quadratic convergence at nodal points, thanks to a property known as superconvergence.[9,10] While the complex interplay of dielectric discontinuities and point charges in our test case precludes reaching

---

[9] José A Ferreira and Rolf D Grigorieff. "On the supraconvergence of elliptic finite difference schemes", 28pp. 275–292, 1998.

[10] Pasquale Claudio Africa, Carlo de Falco, and Simona Perotto. "Scalable recovery-based adaptation on Cartesian quadtree meshes for advection-diffusion-reaction problems", 1pp. 443–473, 2023.

this theoretical optimum, the NGPB solver comes remarkably close, further affirming its accuracy and robustness under non-ideal conditions.

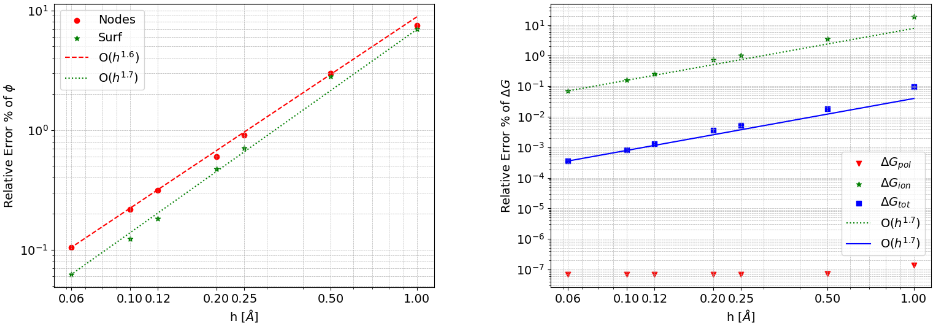

(A) (B)

FIGURE 5.2: Convergence of (left) electrostatic potential errors (calculated at nodes using (5.1.3) and on surfaces using (5.1.4)) and (right) total energy errors with mesh refinement for the Kirkwood sphere, compared to analytical values. NGPB exhibits near-optimal convergence behavior even in the presence of dielectric discontinuities.

5.1.2 Non-Overlapping Spheres

As introduced in Sec. 3.3.2, analytical solutions can also be derived for systems composed of multiple non-overlapping spheres. These systems closely resemble realistic biomolecular environments in terms of the challenges they pose for PB solvers, excluding only the complexity associated with constructing the MS. For this purpose, we consider a 30-sphere configuration depicted in Fig. 5.3. The positions of the spheres are deliberately chosen to eliminate any spatial symmetry, further increasing the difficulty of the problem and mimicking real-world molecular asymmetry. Additionally, to test the solver's ability to reproduce electrostatic potentials in a biologically relevant context, we follow a strategy commonly used in pKa estimation protocols:[11] the three spheres located at the highest z-coordinates are assigned zero charge. This allows us to assess how well the solvers compute the electrostatic potential at neutral atoms—an essential capability for titration-based calculations.

For this benchmark, we assess our code in terms of accuracy and compare it with that of other well-established solvers, such as DelPhi and MIBPB. All solvers are tested using identical simulation settings: a uniform grid with spacing of 0.5 Å, homogeneous Dirichlet boundary conditions, and a computational domain where spheres occupy approximately 20% of the total volume. The results are summarized in Tabs. 5.2 and 5.3, and visually represented in Fig. 5.4. As with the single-sphere case, NGPB

---

[11] Yifan Song, Junjun Mao, and M. R. Gunner. "MCCE2: Improving protein pKa calculations with extensive side chain rotamer sampling", 30pp. 2231–2247, 2009.

delivers superior accuracy, with relative errors in both energy and potential consistently outperforming DelPhi and MIBPB. The error in total energy for NGPB is nearly an order of magnitude lower than that of DelPhi and more than double that of MIBPB. Furthermore, NGPB remains stable and reliable even in regions with null charge, accurately reproducing potential values at the centers of neutral spheres.

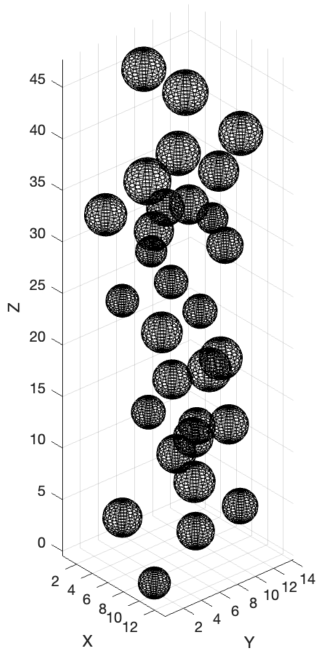

FIGURE 5.3: Schematic representation of the 30-sphere benchmark system. The configuration lacks spatial symmetry and includes three neutral spheres for assessing potential accuracy.

5.1.3 Assessment of Boundary Conditions

In this section, we evaluate the effectiveness of the BCs implemented in our solver, as introduced in Sec. 4.8. It is well established that different boundary conditions, along with grid-induced artifacts, can significantly affect the outputs of a PB calculation. However, the extent of this influence depends on the specific physical quantity being analyzed.

To explore this, we begin with a one-sphere system and compare the impact of D-H (or Coulombic) BCs against that of null Dirichlet BCs, at a perfil of 80%. At this setting, the D-H BCs clearly provide greater accuracy. As shown in Fig. 5.5 and Tab.5.4,

-	Polarization	Ionic	Total
Value $[K_bT]$	-10310.57	-151.13	-2255.59
Relative error			
-	Polarization	Ionic	Total
NGPB	-4.16e-05	1.39e-02	7.46e-04
DelPhi	4.13e-04	-8.85e-02	-4.04e-03
MIBPB	4.00e-03		1.86e-02

TABLE 5.2: Analytical value and signed relative error in energy calculation for NGPB, DelPhi and MIBPB on the 30-sphere system. The percentage of box filling is 20%, and null BCs are used. For MIBPB, we can not separate the energy contributions from the polarization and ionic terms individually, so we report the error for their combined total along with the total energy error.

-	Atom1	Atom2	Atom3
NGPB	2.71e-05	-1.19e-03	-4.66e-03
DelPhi	6.04e-04	4.60e-03	8.56e-03
MIBPB	-2.99e-01	-3.07e-01	-2.97e-01

TABLE 5.3: Signed relative error of the electrostatic potential on uncharged atoms for NGPB, DelPhi, and MIBPB in the 30-sphere system, compared to the analytical solution. The box filling percentage is 20%, and null BCs are applied.

the improved accuracy strongly affects the potential at the solute surface and, consequently, the ionic component of the energy. However, this impact becomes negligible if only the polarization term—typically the dominant contribution—is considered.

We then show the results obtained by leaving a uniform grid resolution on a region of parallelepipedal shape around the solute and performing a grid de-refinement until a much larger computational domain is reached. This technique allows us to bring the boundaries of the computational domain at a distance where null Dirichlet BCs become accurate irrespective of the system-specific geometry. This is obtained without a significant increment of the number of degrees of freedom, which may even get reduced for highly non-globular solutes relative to standard cubic computational domains (see Fig. 5.6).

We apply this strategy to a 30-sphere system, comparing D-H/Coulombic BCs at 80% perfil with null BCs under de-refinement down to 20% perfil, starting from both 80%

BCs	Polarization	Ionic	Total
D-H @80%	7.38e-10	4.91e-02	2.49e-04
NULL @80%	7.38e-10	6.12e-01	3.10e-03

TABLE 5.4: Signed relative error in energy calculations using NGPB compared to analytical results, showing performance with null BCs and and Debye-Hückel (D-H) BCs for one-sphere systems at 80% box filling (perfil).

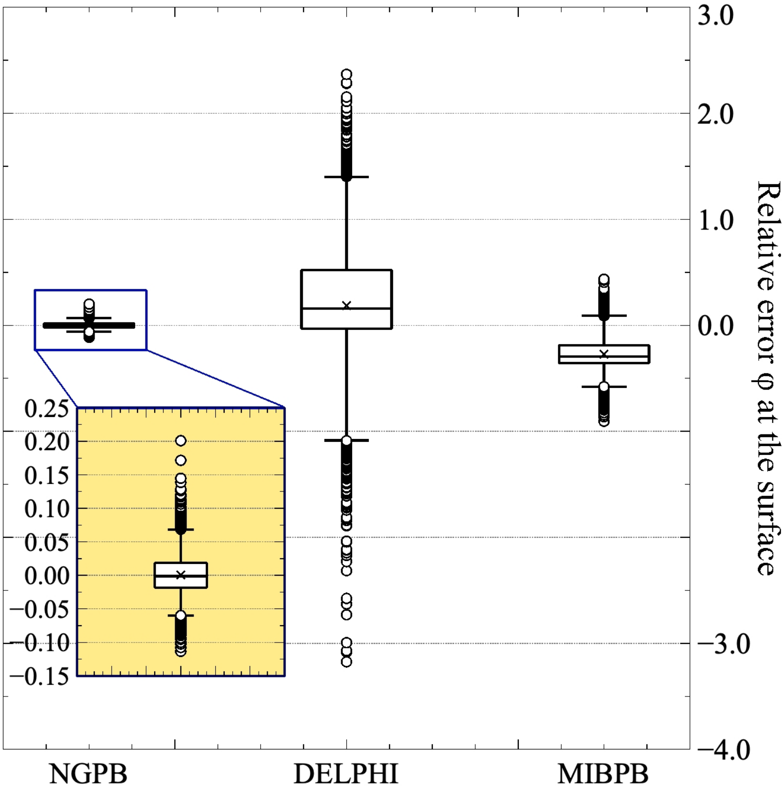

FIGURE 5.4: Box plot of the signed relative error for the electrostatic potential at the surface, comparing NGPB, DelPhi, and MIBPB results against analytical solutions for the 30-sphere system. The surface potential is evaluated at the vertices generated by NanoShaper, using Eq. (4.4.20) for NGPB and classical trilinear interpolation for DelPhi and MIBPB.

and 95%. As seen in Fig. 5.7, null BCs achieve excellent accuracy once the boundary is sufficiently far from the solute (perfil $\leq$ 20%).
Moreover, adopting a parallelepipedal rather than cubic grid and refining the domain from 80% to 95% before de-refining offers a favorable trade-off. The extra degrees of freedom introduced in the solvent region are offset by the more efficient grid layout, resulting in enhanced accuracy without prohibitive computational cost. This combined approach proves both robust and practical for large-scale PB simulations.

5.2 Real Biomolecular Systems

In the previous sections, we have presented and validated the theoretical foundation and computational performance of our solver. However, to truly assess its utility

and accuracy, it is essential to apply it to realistic biomolecular systems, systems that mirror the complexities and intricacies of actual biological molecules. Electrostatic interactions play a fundamental role in driving molecular recognition, binding, and overall molecular behavior, making accurate electrostatic calculations crucial for understanding and predicting the function of biomolecules in biological processes.
Here, we demonstrate the effectiveness of our solver by applying it to several real-world biomolecular systems. These include systems with complex geometries and intricate molecular interactions, where precision and computational efficiency are paramount. By investigating the electrostatic properties of these systems, we can evaluate the solver's performance in a biologically relevant context and further establish its potential for applications in drug design, biomolecular engineering, and structural biology.

5.2.1 Binding Energy Calculation

One of the most critical applications of PB solvers in molecular biophysics is the estimation of binding free energies. These energies quantify the thermodynamic favorability of molecular interactions, such as those between a protein and a ligand or two biomolecular partners. In this section, we evaluate the accuracy and convergence

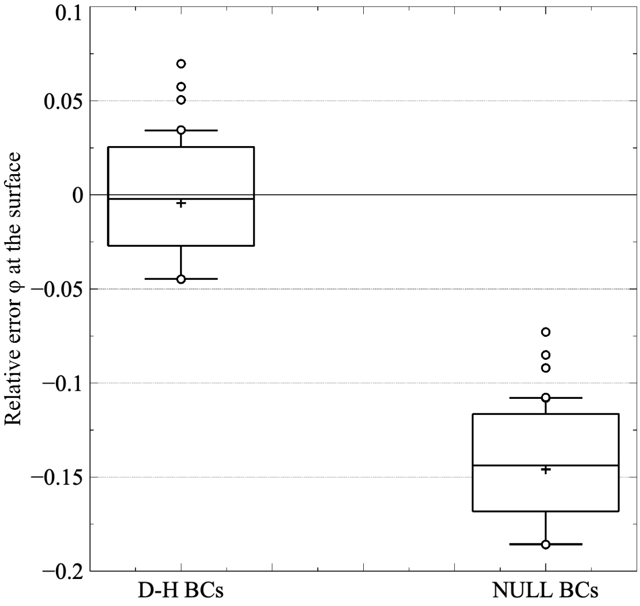

FIGURE 5.5: Box plot of signed relative error of potential at the surface compared to analytical results for one-sphere systems, showing NGPB performance with different BCs at 80% box filling (perfil). The surface potential is evaluated at the vertices generated by NanoShaper, using Eq. (4.4.20).

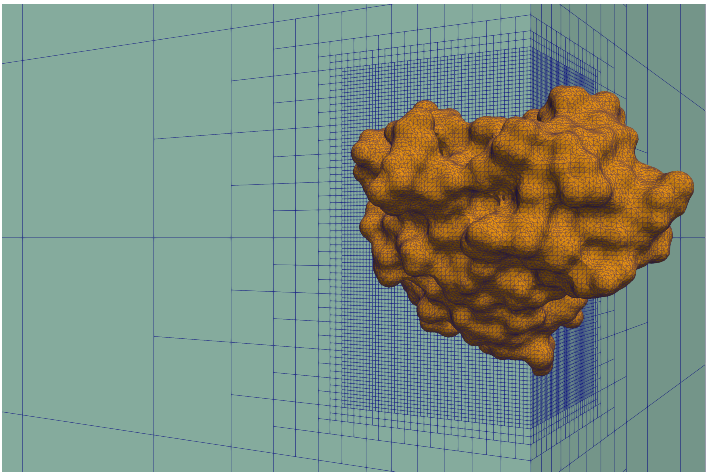

FIGURE 5.6: Visualization of the adaptive grid used to extend the computational domain for accurate BCs implementation

behavior of our solver, NGPB, by focusing on the binding free energy difference, denoted $\Delta\Delta G$. This quantity captures the change in electrostatic free energy upon complex formation and is defined as:

$$\Delta\Delta G = \Delta G_c - \Delta G_1 - \Delta G_2 \tag{5.2.1}$$

where ΔG denotes the total electrostatic energy as defined in Eq. (3.1.6), and the subscripts c, 1, and 2 correspond to the complex and its two unbound components, respectively.

To put our solver to the test, we consider six representative biomolecular complexes from the benchmark dataset compiled by Fenley and co-workers.[12] These complexes span a diverse range of charge distributions and molecular sizes, making them well-suited for probing solver performance in realistic scenarios. Our goal is to assess how well NGPB captures $\Delta\Delta G$ and total energy across varying grid resolutions. To do this, we compute energies at several resolutions and use results obtained at a fine grid spacing of 0.2 Å as our reference. We then evaluate the rate and quality of convergence as the grid becomes coarser. Moreover, we place our results in context by comparing against several state-of-the-art PB solvers, including CPB,[13] MIBPB,[2] DelPhi,[1]

---

[12] Robert C Harris, Alexander H Boschitsch, and Marcia O Fenley. "Influence of grid spacing in Poisson-Boltzmann equation binding energy estimation", 9pp. 3677–3685, 2013.

[13] Alexander H Boschitsch and Marcia O Fenley. "A fast and robust Poisson-Boltzmann solver based on adaptive Cartesian grids", 7pp. 1524–1540, 2011.

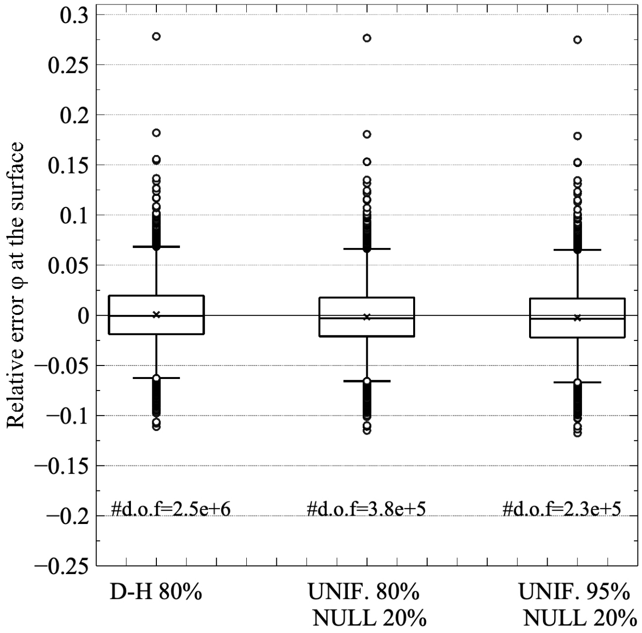

FIGURE 5.7: Box plot of signed relative error of potential at the surface compared with analytical results on the 30-spheres system using different BCs. D-H/Coulombic BCs on a cubic grid with 80% perfil are used in the leftmost column. In the second and third, parallelepipedal uniform grid (perfil of 80% and 95%, respectively) followed by a derefined one until 20% are used. The reduction in d.o.f. from the first and the second columns is due to the aspect ratio of the system, which permits a further computational saving due to the parallelepipedal shape of the uniform grid.

PBSA,[14] APBS[15] and FEM-BEM,[16] using published results from the works [16, 17]. To balance computational cost and accuracy, we use a locally refined grid setup. A 90% perfil uniform grid is applied around the solute, followed by progressive derefinement toward 20% perfil in the bulk solvent, which allows for domain enlargement without an exponential growth in degrees of freedom. To mitigate errors due to grid positioning, we perform 30 random displacements of the solute centroid within a cube of side equal to half the grid spacing. We then report the mean and standard deviation of the computed energies.

---

[14] Jun Wang et al. "Poisson-Boltzmann solvents in molecular dynamics simulations", 3pp. 1010–1031, 2008.

[15] Nathan A Baker et al. "Electrostatics of nanosystems: application to microtubules and the ribosome", 98pp. 10037–10041, 2001.

[16] Michał Bosy et al. "Coupling finite and boundary element methods to solve the Poisson-Boltzmann equation for electrostatics in molecular solvation", 45pp. 787–797, 2024.

[17] Duc D Nguyen, Bao Wang, and Guo-Wei Wei. "Accurate, robust, and reliable calculations of Poisson-Boltzmann binding energies". *Journal of computational chemistry* 38, pp. 941–948, 2017..

Tab. 5.6 summarizes the computed $\Delta\Delta G$ and total electrostatic energy across grid resolutions, along with standard deviations from centroid displacements. Using data for CPB[12] and MIBPB,[17] Fig. 5.8 shows the convergence plots for these solvers alongside those of NGPB. As one can see, we obtained satisfactory convergence at a grid spacing of 0.67 Å for $\Delta\Delta G$. As per the total energy, see Fig. 5.9, NGPB results are already quite accurate, starting from a grid spacing of 1 Å. For calculating $\Delta\Delta G$, CPB reaches good convergence values for grid spacing values ≤ 0.4 Å, while MIBPB has better control over the results at larger spacings and a less rapid convergence in the low spacing range. It is worth noting that both local refinement around the surface, as done in CPB, and second-order accuracy enforcement, as done in MIBPB, entail a quite significant computational cost. The results for individual binding energies at the finest mesh for different solvers, also taken from Refs. [12, 17], are compared with those of NGPB. Interestingly, while there can be quite significant differences among the results of different solvers and considering that there is no ground truth for these realistic systems, we can however observe that the results of NGPB are always close to those of MIBPB, which is supposedly among the most accurate solvers since it enforces second-order accuracy.

An additional point of interest emerges when analyzing the ionic component of the binding energy. This term, often considered negligible in moderately charged systems, can become significantly more influential in systems with high net charges. To better understand this effect, we decompose the total binding energy as follows:

$$\Delta\Delta G = \Delta\Delta G_{coul} + \Delta\Delta G_{pol} + \Delta\Delta G_{ion} \tag{5.2.2}$$

where $\Delta\Delta G_{coul}$ captures direct Coulomb interactions, $\Delta\Delta G_{pol}$ accounts for polarization effects, and $\Delta\Delta G_{ion}$ reflects ionic contributions. Tab. 5.5 presents this breakdown across the benchmark systems. We find that for systems with higher charge densities, $\Delta\Delta G_{ion}$ plays a non-negligible role in determining the total binding energy It is plausible that the observed discrepancies among some of the considered solvers, which are larger for more highly charged systems, are due to the specific ways used to calculate this term.

In conclusion, these results affirm that NGPB not only achieves competitive accuracy in computing binding energies but does so with greater computational efficiency at coarser resolutions. Its accuracy closely matches that of MIBPB and shows robustness across varying grid setups, making it a valuable tool for the study of realistic biomolecular interactions.

5.2.2 Application to Large Systems

Advances in experimental structural biology—particularly cryo-electron microscopy and X-ray crystallography—are now delivering biomolecular structures at atomic or near-atomic resolution, even for macromolecular assemblies of unprecedented size. These breakthroughs open new frontiers in our understanding of complex biological

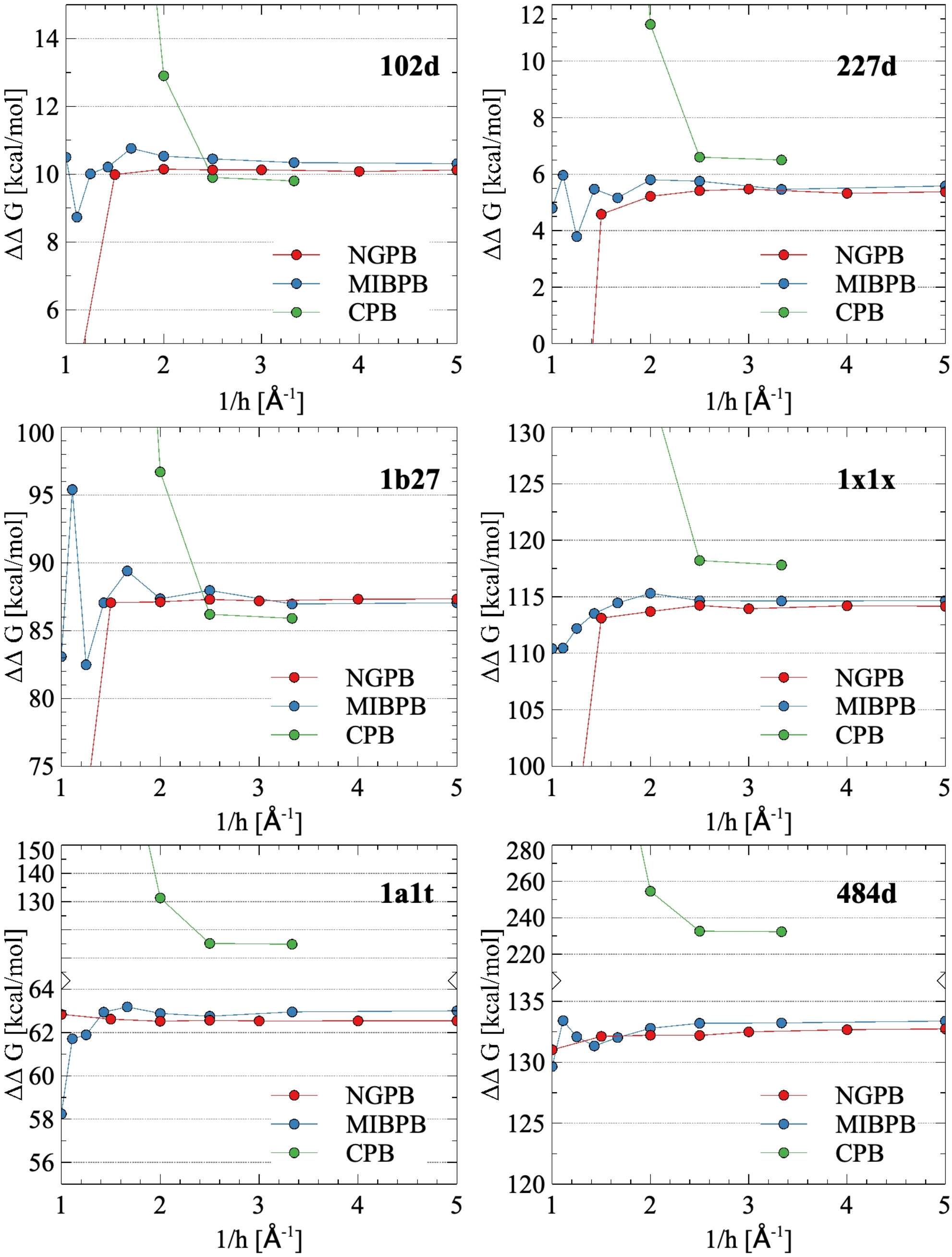

FIGURE 5.8: Convergence trends of binding free energy $\Delta\Delta G$ for each molecular complex toward the finest mesh solution, evaluated for NGPB, MIBPB, and CPB approaches.

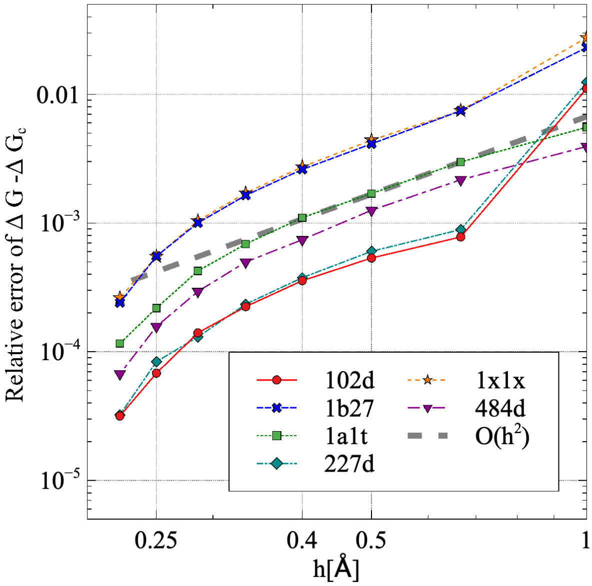

FIGURE 5.9: NGPB convergence profile for the total electrostatic energy w.r.t. the case where $h = 0.2$ Å.

Complex	Total charge $[e]$	$\Delta\Delta G_{ion}/\Delta\Delta G$
102d	-20	0.90
227d	-20	1.71
1b27	-4	0.03
1x1x	-3	0.02
1a1t	8	0.59
484d	-16	0.35

TABLE 5.5: Relative contribution of the ionic component ($\Delta\Delta G_{ion}$) to the total binding energy ($\Delta\Delta G$) for each molecular complex, highlighting its significance in the overall binding free energy.

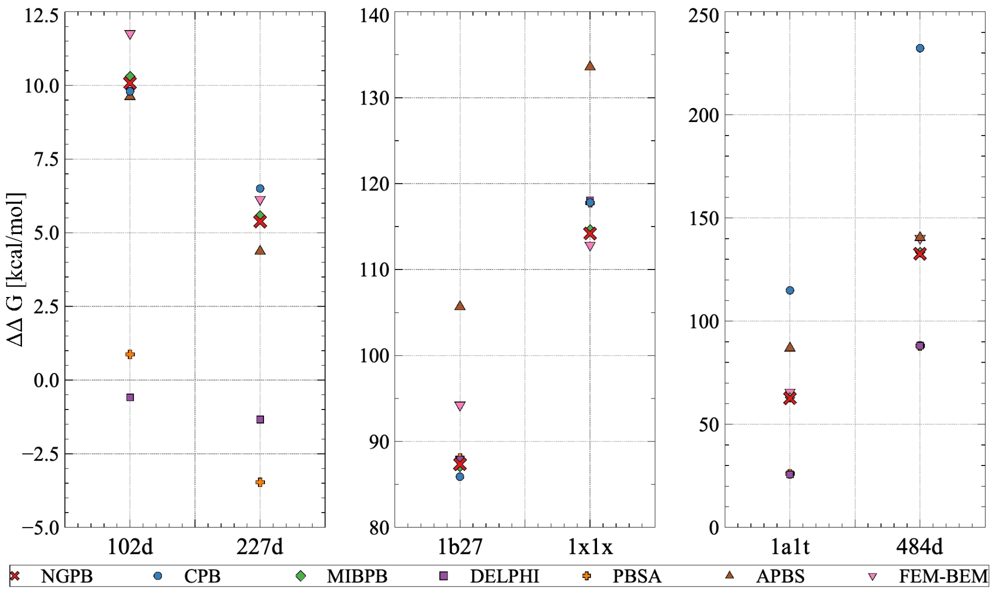

FIGURE 5.10: Comparison of calculated binding energies across different PB solvers (NGPB, MIBPB, CPB, DELPHI, PBSA, APBS, FEM-BEM) at fine grid resolution (0.2 Åspacing), demonstrating solver-dependent variations in electrostatic binding free energy calculations.

systems, but they also pose serious computational challenges. Electrostatic calculations for such massive systems demand solvers that are not only accurate but also highly efficient and scalable.

To demonstrate the capability of NextGenPB in handling these challenges, we applied our solver to compute the electrostatic potential for two large viral systems: the capsid of the swine influenza virus H1N1 and the human adenovirus, whose structure is available in the Protein Data Bank under the identifier 1VSZ. For the H1N1 capsid—a system characterized by its extensive, quasi-spherical shell structure—we adopted a grid spacing of 2 Å, which balances computational efficiency with sufficient resolution to capture global electrostatic features across the viral envelope. In contrast, for the 1VSZ adenovirus, we employed a finer grid resolution of 0.5 Å. This higher resolution was chosen to capture finer electrostatic details near the capsid's intricate surface features and internal cavities, where local variations in potential are critical to understanding molecular recognition and interaction sites. Once the electrostatic potentials were computed, we mapped them onto the molecular surfaces of both systems. These visualizations, shown in Fig. 5.11 for H1N1 and Fig. 5.12 for 1VSZ, reveal key insights into the spatial distribution of electrostatic charge. Regions of highly positive or negative potential are clearly highlighted, suggesting potential hotspots for interaction, such as binding sites for nucleic acids, host receptors, or therapeutic agents.

Despite the significant differences in size and structural complexity between the two systems, NextGenPB delivers consistent and meaningful results, underscoring its scalability and versatility in the field of computational electrostatics.

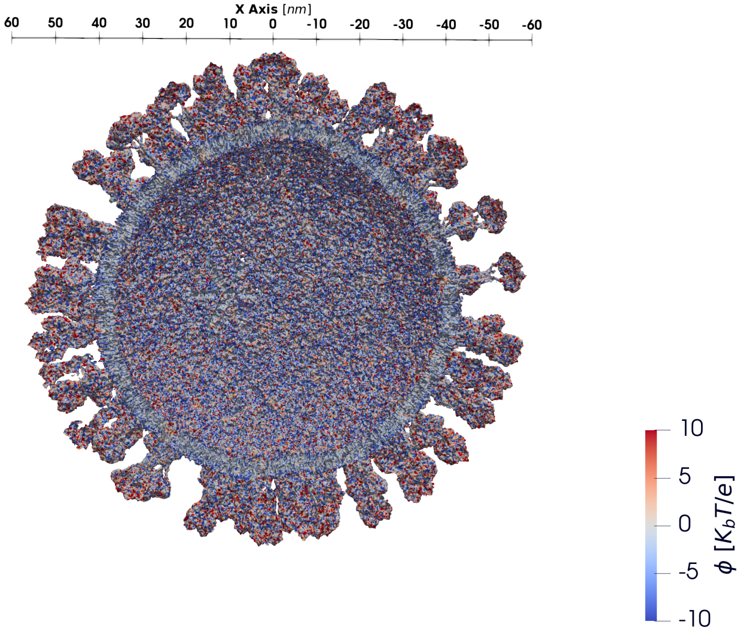

FIGURE 5.11: Cross-sectional view of the H1N1 swine influenza virus structure (14 million atoms), with molecular surface coloration representing local electrostatic potential calculated by NGPB.

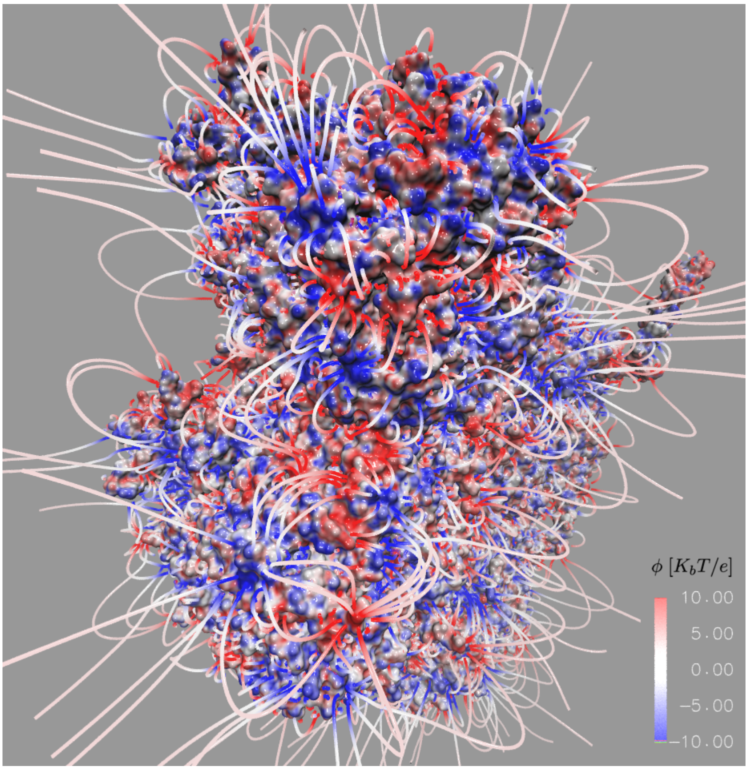

FIGURE 5.12: Human adenovirus structure (pdb id 1VSZ, 180457 atoms) with the molecular surface colored based on the local electrostatic potential calculated by NGPB and showing main electric field lines.

	102d		1b27		1a1t	
h[Å]	$\Delta\Delta G$	σ	$\Delta\Delta G$	σ	$\Delta\Delta G$	σ
1.00	11.16	28.10	54.49	12.44	63.17	2.30
0.67	9.87	1.34	86.71	2.41	62.82	1.09
0.50	10.01	0.42	87.16	0.99	62.35	0.68
0.40	10.24	0.43	87.31	0.72	62.79	0.50
0.33	10.08	0.42	87.34	0.34	62.54	0.26
0.25	10.08	0.28	87.30	0.22	62.51	0.23
0.20	10.08	0.20	87.35	0.17	62.59	0.19
	ΔG	σ	ΔG	σ	ΔG	σ
1.00	-25612.73	21.94	-64947.35	6.20	-41003.42	1.92
0.67	-25550.94	1.13	-64982.73	1.49	-41012.02	0.80
0.50	-25552.22	0.34	-64990.27	0.79	-41016.33	0.37
0.40	-25553.14	0.29	-64993.69	0.43	-41018.32	0.29
0.33	-25553.83	0.30	-64995.87	0.19	-41019.71	0.11
0.25	-25554.65	0.18	-64998.33	0.13	-41021.29	0.15
0.20	-25555.00	0.14	-64999.58	0.08	-41022.01	0.09

	227d		1x1x		484d	
h[Å]	$\Delta\Delta G$	σ	$\Delta\Delta G$	σ	$\Delta\Delta G$	σ
1.00	-17.30	26.39	74.41	13.91	130.84	4.09
0.67	4.58	1.82	112.77	1.84	131.93	0.93
0.50	5.43	1.02	113.87	0.89	132.16	0.57
0.40	5.43	0.53	114.12	0.63	132.00	0.52
0.33	5.43	0.27	114.05	0.51	132.37	0.46
0.25	5.47	0.25	114.09	0.44	132.60	0.30
0.20	5.38	0.18	114.19	0.22	132.63	0.30
	ΔG	σ	ΔG	σ	ΔG	σ
1.00	-27099.69	22.64	-64663.93	5.28	-39427.15	2.91
0.67	-27030.78	1.43	-64707.76	1.08	-39435.01	0.66
0.50	-27032.26	0.45	-64714.43	0.61	-39439.08	0.48
0.40	-27033.44	0.35	-64718.07	0.59	-39441.38	0.34
0.33	-27034.18	0.18	-64720.31	0.44	-39442.46	0.24
0.25	-27034.96	0.18	-64722.83	0.268	-39443.98	0.18
0.20	-27035.40	0.14	-64724.03	0.17	–39444.68	0.09

TABLE 5.6: Calculated binding free energies (ΔG), binding free energy differences ($\Delta\Delta G$), and corresponding standard deviations across 30 independent calculations for each molecular complex.

Chapter 6

Conclusions

This work addresses the electrostatic interactions in charged systems, typically biomolecules, immersed in electrolyte solvents. To this end, we have presented the fundamental equations that best describe the system, implemented novel numerical models, and explored potential practical applications.

We began by discussing the principles of electrostatics relevant to molecular biology. The solvent is modeled as a continuous medium with a high dielectric constant, in which the ions are embedded and represented as a continuous charge distribution. The solute, typically a biomolecule, is treated as a region enclosed by the molecular surface (MS), characterized by a low dielectric constant and containing fixed point charges. Chap. 2 laid the physical foundation for the PBE, including the derivation of its linearized and generalized forms. We showed how a more general formulation of the problem allows for the inclusion of effects typically neglected in standard PB theory, such as finite-size ions and dielectric inhomogeneities.

In Chap. 3, we focused on the analytical study of the LPBE. We introduced a new decomposition of the internal electrostatic potential into Coulombic, polarization and ionic contributions. We reformulated volumetric ionic potentials as surface integrals, which enabled fairly tractable analysis and much greater accuracy in boundary-layer regions. Analytical results of the LPBE were developed for geometries such as the Kirkwood sphere, as well as systems of non-overlapping spheres of arbitrary number, allowing exact benchmarks against which methods developed later could be compared.

A numerical model based on the Primal–Mixed Finite Element Method (PMFEM) has been introduced in Chap. 4. This formulation was chosen because, when the potential ϕ is approximated using piecewise linear functions, standard first-order finite differences become inconsistent with the true electric field in the presence of discontinuous coefficients that are not aligned with the computational grid. However, the PMFEM allows consistency with the dielectric displacement field by sacrificing the pointwise relation $E(x) = \varepsilon(x)D(x)$ and replacing it with an averaged approximation.

A significant challenge addressed in this work was the treatment of coefficient discontinuities across the molecular surface Γ. We presented a dual approach: a 1D analytical model to understand the local behavior near interfaces, and a physics-based weighted harmonic average (WHA) to ensure proper flux continuity. This approach was embedded directly into the FE formulation, leading to improved stability and convergence. The treatment of point sources was handled through a regularized projection strategy, preserving physical accuracy without introducing numerical instabilities.

Chap. 4 also presented a detailed method for calculating electrostatic energies, including the polarization contribution and the ionic direct term, both crucial for estimating biomolecular binding energies. Moreover, we introduced mesh de-refinement strategies to reduce computational cost while maintaining precision in key regions, such as near the interface Γ and around atomic centers. The numerical method was implemented in `NextGenPB`, a modern software architecture written with scalability and modularity in mind. This platform allows for easy integration with external tools, supports adaptive meshing, and is optimized for high-performance computing environments.

In Chap. 5, we validated our method through numerical testing. Comparisons with analytical results for the Kirkwood model and multi-sphere systems demonstrated excellent agreement, confirming the correctness of the solver and its implementation. Further, we tested our method on real biomolecular systems, including proteins with thousands of atoms. We demonstrated the solver's capability to compute binding free energies and electrostatic potential distributions with high accuracy and efficiency. The accurate representation of boundary conditions, validated through sensitivity tests, further confirmed the robustness of our numerical treatment.

Key Contributions

The key contributions of this thesis can be summarized as follows:

- Theoretical Integration: A complete pipeline from physical modeling to numerical solution for biomolecular electrostatics, grounded in thermodynamically consistent extensions of the PBE.
- Analytical Decomposition: A novel analytical formulation of the LPBE solution using Green's identities, leading to surface-integral representations and physically interpretable potential components.
- Advanced Numerical Formulation: Development and implementation of a Primal–Mixed Finite Element solver incorporating WHA for material interfaces and regularization for point charges.
- Efficient and Scalable Code: Implementation of the above in the `NextGenPB` software, enabling simulations of complex systems with thousands of atoms on adaptive meshes.
- Validation on Real Systems: Demonstration of solver accuracy against both analytical benchmarks and realistic molecular systems, including binding energy computations.

Limitations and Future Work

While the current formulation handles linear PBE and its extensions with high fidelity, several avenues for improvement remain. The extension to the nonlinear PBE is a natural next step and would allow for more accurate modeling of highly charged systems or those with strong ionic screening. Future work may also focus on integrating a more sophisticated ion-size and solvation model, perhaps informed by statistical mechanics or coarse-grained simulations.

Another promising direction involves coupling NextGenPB to molecular dynamics (MD) simulations to compute time-resolved electrostatic properties, or embedding the solver within multi-scale modeling frameworks. The use of machine learning techniques to predict potential maps or optimize mesh refinement dynamically could also significantly enhance performance in large-scale simulations.

Lastly, the framework developed here could be extended beyond biomolecular systems, to applications in colloidal science, electrochemistry, and nanotechnology, where electrostatic interactions play a central role in self-assembly and transport processes.

Part II

Additional work: Microscopic state equation for oscillator chains

The content of this Part reflects work that has been previously published in the article:

Di Florio, V., Giberti, C., Rondoni, L. et al. Microscopic state equation for oscillator chains. Eur. Phys. J. Plus 139, 622 (2024). `https://doi.org/10.1140/epjp/s13360-024-05419-1`

Rather than reworking the material to conform to a different referencing style, the original citation format has been retained for coherence and consistency with the published version. In particular, references appear in-line rather than as footnotes, as was done in the original manuscript.

Chapter 7

Microscopic state equation for oscillator chains

7.1 Introduction

The properties of 1-dimensional systems made of linearly or nonlinearly interacting oscillators are the subject of a vast literature, that began with the FPUT model [1], and then ramified in countless directions. Initially, the problem of energy equipartition, relaxation to equilibrium, and related ergodic notions were investigated. Later, energy transport in non-equilibrium conditions became most popular. See *e.g.* [2] for a selection of works concerning both phenomena. Chains of oscillators have been considered because of their simplicity and, more recently, because they appeared to enjoy some properties of nano-technological interest [3]. While energy equipartition is fairly well understood [4–7], the transport of energy still poses numerous questions. One widely accepted view is that energy transport in FPUT-like 1-dimensional systems is typically anomalous, *i.e.* it violates Fourier law, although different and even contrasting points of view are found in the specialized literature, see *e.g.* [8–12]. One characteristic feature of anomalous transport is that bulk properties depend on the boundary conditions and, in particular, depend on the length of the chain. Therefore, local thermodynamic equilibrium [1] is not established [14–17]. Indeed, by its very definition, locality requires spacial correlations to decay within mesoscopic distances. Then, properties of matter in the bulk, such as the transport coefficients, are not affected by boundaries located "sufficiently far", *i.e.* beyond a moderate number of mean free paths from the place of interest. For a detailed discussion of the local thermodynamic equilibrium condition see *e.g.* references [18] Chapter II Section 9, [19] Chapters 3–5, [20] Section 15.1, [21] Section 2.3, [22] Section 3.3, [23] Chapter 1, [24, 25]. It is clear that observables of small and low dimensional systems are less likely to obey local thermodynamic equilibrium than 3-dimensional macroscopic systems, because spatial constraints hinder the decay of correlations. This constitutes part of the reasons leading to anomalous transport.

---

[1] Thermodynamic equilibrium is the fundamental property justifying the local mass, momentum and energy balances as thermodynamic relations [13].

Interestingly, mean free paths are known to be unbounded in many 1-dimensional systems, so locality is violated, but in certain cases one may identify structures that interact over short distances and enjoy locality (high frequency modes), while others do not, and lead to anomalous transport (low frequency modes) [26]. This allows a consistent description of the phenomenon at hand. Furthermore, there are models and conditions under which transport turns normal even in 1-dimensional systems, see *e.g.* [2, 3, 27–29]. In particular, the symmetries of the oscillators interaction potentials have been found to play an important role in certain models [8–12]. This result can also be obtained by adding a strain to the chains [30].

Given the complexity of such a scenario, it is desirable to find relations describing the state of 1-dimensional systems in terms of a reduced number of variables, *i.e.* of counterparts of the thermodynamic equations of state, holding beyond standard thermodynamics. In this respect, it is interesting to recall the beginning of Section 9 of Ref.[18], which explains that different kinds of thermodynamic quantities exist *"Thermodynamic physical quantities are those which describe macroscopic states of bodies. They include some which have both a thermodynamic and a purely mechanical significance, such as energy and volume. There are also, however, quantities of another kind, which appear as a result of purely statistical laws and have no meaning when applied to non-macroscopic systems, for example entropy".*

The relation discovered in Ref.[15] (Eq. (5) of that paper), and investigated in a handful of papers: [16, 17, 31, 32] seems to be a good candidate for such an equation of state. Indeed, we are going to show that it holds in a vast variety of cases, in which the boundary between purely mechanical and purely statistical quantities is blurred, both in absence and in presence of external drivings. Although it is reminiscent of the virial theorem of Clausius [33], we conclude that this relation does not derive straight from pure mechanics: it carries statistical information as well. At the same time, it is a microscopic kind of relation because it does not involve averaging over many particles or over very large times.

The rest of the article is organised as follows. In Section 7.2 we present and discuss the microscopic state equation and review the 1-dimensional particle systems on which it is tested. In Section 7.3, we numerically evaluate the validity of Eq. (7.2.7) for different potentials. In Section 7.4, we focus our attention on the behaviour of $\beta-$FPUT chains, giving an attempt at a theoretical explanation of our results. In this section the chain with stochastic baths is also considered. In section 7.5, we validate the linear relation (7.2.7) for 2-dimensional nets. Finally, in Section 7.6, we draw our conclusions.

7.2 Models and the microscopic relation

In the present paper, we consider systems of N interacting oscillators of unit mass and positions $x_i \in \mathbb{R}$, with $i = 1, ..., N$. In positions x_0 and x_{N+1} we place particles that do not move and interact respectively with particle 1 and N like all oscillators do. In some cases, these walls repel the approaching moving particles, confining the dynamics within the interval $[x_0, x_{N+1}]$, in other cases, they allow the moving particles to pass beyond them. Particles 1 and N also interact with deterministic or stochastic thermostats, of temperatures T_L and T_R respectively. Letting r denote the difference of coordinates of particles with consecutive labels, *e.g.* $(x_{i+1} - x_i)$, the potential energies of the particles interactions we investigate are expressed by:

$$\bullet \text{ Harmonic:} \quad V(r) = \frac{k}{2}(r-a)^2 \tag{7.2.1}$$

$$\bullet \text{ Harmonic+hard core:} \quad V(r) = \begin{cases} \frac{k}{2}r^2 & \text{if } r > a \\ +\infty & \text{if } r \leq a \end{cases} \tag{7.2.2}$$

$$\bullet \text{ Soft-point:} \quad V(r) = \frac{1}{2}\left(r^2 + \frac{1}{r^2}\right) \tag{7.2.3}$$

$$\bullet \text{ Lennard-Jones:} \quad V(r) = 4\epsilon\left[\left(\frac{\sigma}{r}\right)^{12} - \left(\frac{\sigma}{r}\right)^{6}\right] \tag{7.2.4}$$

$$\bullet\ \beta - \text{FPUT:} \quad V(r) = \frac{g_2}{2}(r-a)^2 + \frac{g_4}{4}(r-a)^4 \tag{7.2.5}$$

In Eq. (7.2.1), a is the distance at which the energy is minimum. In Eq. (7.2.2), a is the radius of the hard core elastic repulsion. In Eq.(7.2.4), ϵ characterizes the intensity of the interaction, and σ is the distance at which the Lennard-Jones (LJ) potential vanishes, $a = 2^{1/6}\sigma$ being the rest distance at which the potential switches from being repulsive to being attractive. In Eq.(7.2.5), a is the distance at which the β-FPUT force vanishes, *i.e.* the rest distance at which the interaction energy is minimum. The rest distance of the soft-point chain (SPC), i.e. the chain with potential (7.2.3), is $a = 1$. In the LJ case, we also consider first and second nearest neighbour interactions, meaning that they consist of the sum of two terms involving two neighbours, respectively with characteristic distances σ and 2σ:

$$V(r_1, r_2) = 4\epsilon\left[\left(\frac{\sigma}{r_1}\right)^{12} - \left(\frac{\sigma}{r_1}\right)^{6}\right] + 4\epsilon\left[\left(\frac{2\sigma}{r_2}\right)^{12} - \left(\frac{2\sigma}{r_2}\right)^{6}\right] \tag{7.2.6}$$

where r_1 is the distance between the particle of interest i say, and particle $i+1$, and r_2 the distance between particle i and particle $i+2$. Then, the mechanical equilibrium configuration of the chain is the same produced by the potential (7.2.4).

Denoting by $S_i = \langle r_i \rangle$ the time average of $r_i = x_{i+1} - x_i$, *i.e.* of the difference of the coordinates of two particles with consecutive labels (obviously a microscopic quantity), and by $T_i = \langle p_i^2/2 \rangle$ the time average of the kinetic energy of the particle labelled by i

(another microscopic quantity), Eq. (5) of Ref.[15] can be written as:

$$T_i = c_1 \cdot S_i + c_2 , \quad i = 1, ..., N \tag{7.2.7}$$

where c_1 and c_2 are real coefficients that depend on the system under investigation. This relation has been reported to hold in numerous situations, cf. [15–17, 31]. Was c_2 negligible, we would have had a microscopic version of Boyle's law, but in general c_2 is not negligible. The quantities S and T can be seen as microscopic extensions of the notions of local inverse density and temperature (apart from the factor k_B).[2] In Ref.[32], the equation of state (7.2.7) has been derived under the assumption that a functional dependence $F(S, T) = 0$ of S and T exists at each point along the chain, and that $\Delta T = T_R - T_L$ is small.

Based on the results of Refs.[10, 30], in the present paper, we are going to show that such a derivation does not apply in the case of symmetric potentials, and we develop a more general approach. In particular, we investigate the validity of the equation of state (7.2.7) mainly considering 1-dimensional chains of oscillators linked by nearest neighbors interactions. We study the effects of stretching or compressing our chains, which is achieved placing the walls at distances larger or shorter than $N + 1$ times the rest distance a. The deformation of the chain is quantified introducing the dilation factor:

$$\alpha = \frac{x_{N+1} - x_0}{a(N+1)} \quad , \tag{7.2.8}$$

where x_{N+1} and x_0 are the fixed positions at the two ends of the chain. In the absence of thermostats, the moving particles oscillate about their mechanical equilibrium positions, expressed by:

$$x_i^{eq} = i\, a\, \alpha , \quad i = 1, \dots N . \tag{7.2.9}$$

When $\alpha = 1$ the chain is neither stretched nor compressed, and the quantity that can be associated with pressure, P say, depends on the potential, *e.g.* for $\beta-$FPUT, $\alpha = 1$ corresponds $P = 0$. The cases with $\alpha > 1$ correspond to a stretched chain, called negative pressure states, $P < 0$. The cases with $\alpha < 1$ correspond to compressed chains, of positive pressure, $P > 0$. This terminology is motivated by the assumption that the equilibrium statistic of the microscopic phases are given by canonical distributions with a constant parameter P denoting the pressure, and is justified by the fact that the particles at $x = 0$ and $x = (N + 1)a$ are subjected to mean forces that respectively pull inside, vanish, or push outside the interval $[x_0, x_{N+1}]$ they delimit.

We have found that changing α at fixed T_L and T_R, intriguing and unexpected profiles of S and T arise, and that the microscopic equation of state (7.2.7) robustly holds,

---

[2] The thermodynamic density and temperature require not only averaging over microscopically very long times, but also averaging over mesoscopic cells occupied by a large number of particles, in which boundary effects are negligible compared to the content of the bulk.

except in particular regions of the parameter space, which are wider in the case of the β-FPUT chains than in the other chains we studied. These facts are related to the symmetries of the interaction potentials, which under certain conditions also affect the energy transport as in Refs. [8–12, 30], while under other conditions they do not [34, 35]. Omitting to repeat all times that the boundary particles usually do not behave like the bulk particles, our main findings are the following.

Commonly, the T profile interpolates monotonically between T_L and T_R, hence relation (7.2.7) can be verified if also S is monotonic. This is not always the case. For instance, Eq. (7.2.7) does not hold for the β-FPUT chains, whose potential is symmetric, when the mechanical equilibrium configuration of the chain constitutes a lattice whose nodes are the rest positions of the potential. In that case, indeed, the S profile is flat. Differently, in the case of harmonic potentials, which are also symmetric, Eq.(7.2.7) holds. The fact is that both S and T are flat in the bulk of harmonic chains, hence Eq. (7.2.7) is verified with $c_1 = 0$ and $c_2 = T$. Stretching or compressing the β-FPUT chain, *i.e.* setting $\alpha > 1$ or $\alpha < 1$ respectively the situation changes drastically. The rest positions of the particles in the chain do not coincide anymore with $x_i = ia$. Consequently, the interaction potential is not symmetric about the mechanical equilibrium positions, the S profile acquires a slope, and it gradually couples to T as Eq. (7.2.7) prescribes.

For asymmetric potentials, the relation (7.2.7) is generally quite robust under parameters variations. The β-FPUT chains are peculiar from this point of view. This may be related to the fact that their potential, while confining particles more strongly than harmonic potentials, lacks a short range repulsive singularity.

Changing bath temperatures one obtains different S and T profiles, with different c_1 and c_2. Fixing T_R, these coefficients vary linearly with T_L up to quite large values, and then they bend toward a nonlinear regime for still higher values. This has been observed to be the case for the β-FPUT, the SPC and the nearest neighbour LJ potentials. The above suggests that Eq.(7.2.7) is a non-trivial relation, albeit simple and concerning the two most obvious observables of 1-dimensional particles systems. Symmetries of potentials and equilibrium positions play an enthralling role, here, as they do for energy transport.

As analogous results hold also with stochastic thermal baths, Eq. (7.2.7) is suitable to play the role of an equation of state for nonequilibrium (even non-stationary and non-thermodynamic) states of oscillators chains,[3] capable of distinguishing qualitatively different situations for a wide set of 1-dimensional systems. Indeed, with only two microscopic parameters, it characterizes states in a simple fashion, without need for detailed knowledge of the dynamics, like equilibrium thermodynamic equations of state.

We conclude that the case of $\alpha = 1$, which is usually investigated, is peculiar also from the point of view of the state equation (7.2.7), that qualitatively changes behavior at that point. In fact, it is reasonable that something happens when pressure changes from positive to negative. Interestingly, reducing temperature jumps or eliminating them, setting $T_L = T_R$, do not change this qualitative picture. The validity of

---

[3] In equilibrium it holds, but trivially.

Eq.(7.2.7) is gradually restored when the asymmetry of the overall interaction potential turns significant.

In the following sections we report our results about systems with the potentials introduced above. The numerical integrator used is the fourth-order Runge-Kutta method with step size 10^{-3}. In most cases the heat baths are modelled by the deterministic Nosé-Hoover thermostat with relaxation time set to 1. However, in order to check the robustness of our results against the modeling of the baths, a stochastic bath is used and described in Subsection 7.4.2.

7.3 Effect of interaction potentials

The microscopic interaction potentials have limited impact on thermodynamic quantities, that concern large systems occupying a 3-dimensional volume. The effect may be observed on a quantitative level for certain variables, but systems characterized by quite different microscopic dynamics enjoy an almost incredible similarity as proven, for instance, by the perfect gas law or by the existence of universality classes. About thermal phenomena, this was concisely and wittily expressed in Ref. [36] even for non-equilibrium macroscopic systems, driven by thermal baths interacting with their surface: *"the properties of a 'long' metal bar should not depend on whether its ends are in contact with water or with wine 'heat reservoirs'*. Recently these notions have been considered also in the case of anomalous transport phenomena [37], which low-dimensional lattices of oscillators commonly yield. Nevertheless, no fully developed theory is available about such phenomena and systems. Moreover, the non-locality observed in numerous 1-dimensional systems may amplify the effect of microscopic interactions, and affect the validity of certain relations. Therefore, we now investigate the validity of Eq. (7.2.7) for different interaction potentials, recalling that potential symmetry or asymmetry at times make a difference also for transport [10, 30]. In our case, the interaction potential is indeed responsible for different phenomena, which we first illustrate and later interpret theoretically. We begin with the harmonic potential, which is symmetric, and with the non-symmetric potential obtained adding hard core interactions to the harmonic springs. These potentials may be regard as two limit cases obtained by deformation of the $\beta-$FPUT potential. Later we briefly consider also the Lennard-Jones and the SPC potentials.

7.3.1 Harmonic and harmonic plus hard core

Consider harmonic potentials with $\alpha = 1$ and Nosé-Hoover thermostats at $T_L = 5$ and $T_R = 1$. We realize that Eq.(7.2.7) is trivially verified, as already observed in Ref. [15] for much larger ΔT, because the T and S profiles are flat in the bulk of the harmonic chain, and Eq.(7.2.7) holds setting $c_1 = 0$, and properly fixing c_2.

If we add hard core repulsion to the harmonic thermostatted chain, see Eq.(7.2.2), we find that the T and S profiles generally verify Eq.(7.2.7), with $c_1 > 0$. Then, kinetic temperature and mass distribution are coupled in such a way that the mean distance between particles is higher in the regions of higher kinetic temperature. This is

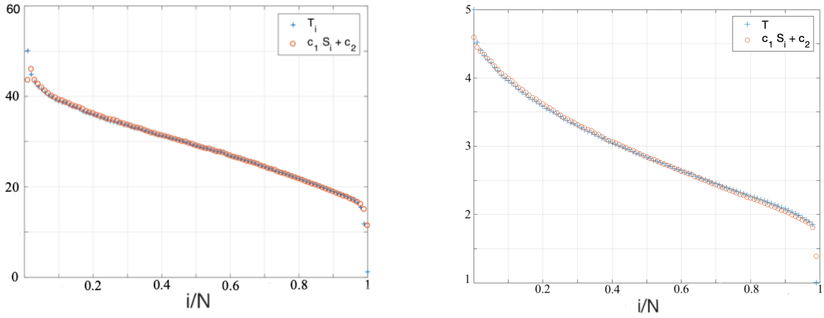

FIGURE 7.1: Left panel: long range harmonic potential and short range hard core repulsion (7.2.2) with $N = 100$ and $T_L = 50$ and $T_R = 1$. In this panel red circles represent the right hand side of (7.2.7). Right panel: verification of relation (7.2.7), for SPC chains with $\alpha = 1$, $T_R = 1$ and $T_L = 5$. In both cases, temperature and S profiles are non-trivially coupled since relation (7.2.7) is perfectly verified with $c_1 > 0$. This means that density of particles is lower where the kinetic temperature is higher. The values of c_2 are not negligible, therefore this system does not behave like a perfect gas.

what one would expect for a normal thermodynamic system, when the mean kinetic temperature corresponds to the thermodynamic temperature, and the mean distance between particles can be directly related to the inverse density. In particular, the left panel of Fig. 7.1 shows the excellent agreement of the data with relation (7.2.7) for simulations with $N = 100$, $\alpha = 1$, and a relatively large ΔT that should not fit the derivation of Ref. [32]. Note that c_2 is large in our simulations, which excludes that the system be considered a perfect gas. Indeed, for a perfect gas the temperature is proportional to the inverse of the density, so c_2 is zero. On the contrary, we note that for a system of many particles, $N \gg 1$, and given L, the average length of the chain, c_2 approximately equals the mean temperature of the chain:

$$c_2 \simeq \overline{T} = \frac{1}{N} \sum_{i=1}^{N} T_i$$

In fact, computing the mean temperature, Eq. (7.2.7) yields:

$$\frac{1}{N} \sum_{i=1}^{N} T_i = \frac{c_1}{N} \sum_{i=1}^{N} S_i + c_2 = \frac{c_1}{N} L + c_2 \tag{7.3.1}$$

which approximately equals c_2 if N is large compared to L, *i.e.* if the spacing between particles is small on the scale of the chain.

7.3.2 SPC potential

In the SPC case, Eq.(7.2.7) is well verified, for $\alpha = 1$ with $c_1 > 0$, see the right panel of Fig. 7.1, which means that the density of particles is lower where the kinetic temperature is higher, as normally expected when thermodynamic identifications make sense. This is illustrated by simulations performed for $N = 100$ and Nosé-Hoover thermostats of temperatures $T_L = 5$ on the left, and $T_R = 1$ on the right.
Further simulations lead to the same results. The behaviour of c_1 and c_2 with T_L is quite interesting: at small T_L, they lie on a straight line, which bends at higher T_L, cf. Fig. 7.2. The relatively high values of c_2 indicate that this chain does not behave like a perfect gas, if S and T are interpreted as thermodynamic quantities.

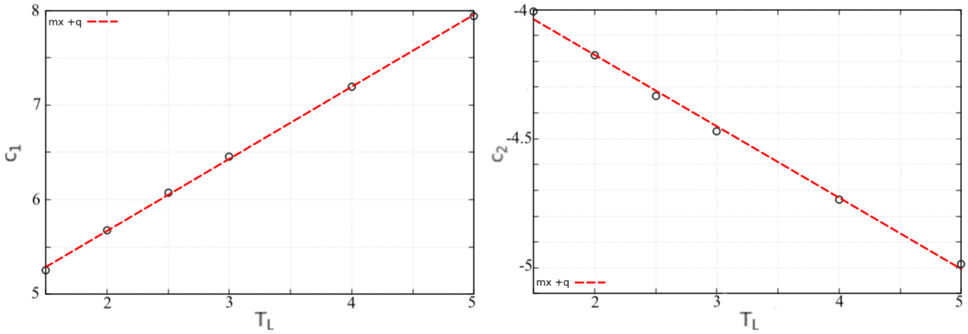

FIGURE 7.2: Behaviour of c_1 (left) and c_2 (right) with Nosé-Hoover thermostats at $T_L \in [1.5, 5]$ for SPC chains with $T_R = 1$, $a = 1$ and $\alpha = 1$. The red dashed lines are the linear fit for T_L up to 5. A linear behaviour is evidenced for relatively small T_L, which turns non-linear at higher T_L.

7.3.3 LJ potential

For the LJ case, the validity of (7.2.7) is verified quite generally for $\alpha = 1$ with $c_1 > 0$, as we have observed for $N = 100$, 150 and 200. As an example, in the right upper panel of Fig. 7.3 we represent the case $N = 200$ with first and second nearest neighbour interactions. Interestingly, although Eq. (7.2.7) also performs relatively well, the situation is different for the LJ potential with nearest neighbour interaction only, cf. left upper panel of Fig. 7.3. Indeed, the S profile is slightly non-monotonic, while the T profile is monotonic, which means that Eq. (7.2.7) cannot be exact, but only approximately valid. Nevertheless, this relation remains generally quite accurate, even under mild as well as strong stretching conditions, where c_1 is always positive. For nearest neighbor LJ chains we verified this fact for several values of α ranging from 1.2 to 100, and we found that relation (7.2.7) holds even when the raw data are noisy. This then suggests one further test. In the lower panels of Fig. 7.3, the profiles are shown for growing times of 1/4, 1/2, and total time $t_{\max}$ with $t_{\max} = 8 \cdot 10^5$. Figure 7.3 shows that relation (7.2.7) is verified also when T and S profiles are far from their asymptotic shape.

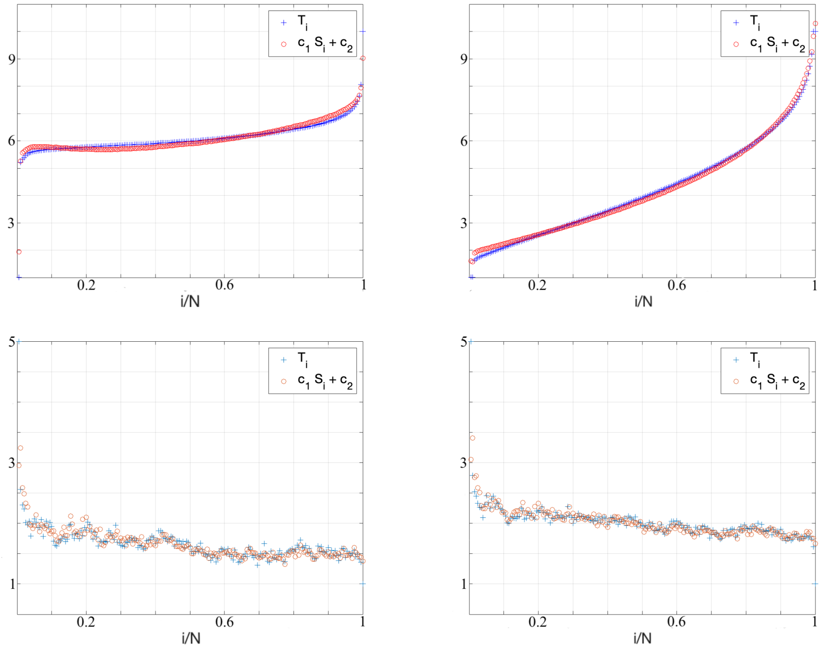

FIGURE 7.3: Top panels: Relation (7.2.7) for LJ chains with nearest neighbour interactions (left panel), and first and second nearest neighbour interactions (right panel). $N = 200$, $\alpha = 1$, $T_L = 1$ and $T_R = 10$. The density profile is not strictly monotonic, which makes Eq. (7.2.7) only approximately but reasonably well verified. Bottom panels: LJ chain with nearest neighbor interactions with $N = 200$, Nosé-Hoover thermostats at $T_L = 5$ and $T_R = 1$, and $\alpha = 100$. Equation (7.2.7) is verified even if the averaging times are quite short: 1/4 (left panel) and at 1/2 (right panel) of the maximum time.

One further observation for LJ chains is that the S profile converges to a bounded asymptotic profile S^∞ as the left reservoir temperature T_L grows, at fixed T_R=1. In other words, denoting by $S_i^{T_L}$ the value of the S profile at the i-th site, with left bath at temperature T_L, and by S_i^∞ the corresponding asymptotic value, we can write:

$$S_i^{T_L} = S_i^\infty + \delta_{T_L}(i)\,, \quad \text{where } \delta_{T_L}(i) \to 0 \quad \text{as} \quad T_L \to \infty\,. \tag{7.3.2}$$

Relation (7.2.7) holds for all T_L, and our simulations show that its coefficients c_1 and c_2 depend on T_L and draw a straight line up to quite large values of T_L. Consequently, the kinetic temperature profile at finite T_L can be related to the asymptotic S profile as:

$$T_i = c_1(T_L)S_i^\infty + c_2(T_L) + c_1(T_L)\delta_{T_L}(i)\,. \tag{7.3.3}$$

In fact, something more can be observed: Fig. 7.4 shows the validity of an asymptotic form of (7.2.7), i.e.:

$$T_i = \hat{c}_1(T_L)S_i^\infty + \hat{c}_2(T_L) \tag{7.3.4}$$

where

$$\hat{c}_1(T_L) = \frac{T_L - T_{L0}}{S_1^\infty - S_N^\infty}, \quad \hat{c}_2(T_L) = T_{L0} - \frac{T_L - T_{L0}}{S_1^\infty - S_N^\infty} S_1^\infty\,. \tag{7.3.5}$$

7.4 β-FPUT oscillators

Given the wide applicability of the state equation (7.2.7) revealed by the previous cases, in this section we investigate β-FPUT chains, which are known to be peculiar under various respects. We consider states of the chain at different pressure, generated by different stretching rates α.

When $\alpha = 1$, the chain is neither compressed nor stretched (for any value of a). In this case, not only the interaction potential is symmetric with respect to its center, but this center coincides with the rest distance for any pair of interacting particles. Consequently, the forces acting on each particle are symmetric with respect to their mechanical equilibrium positions, x_i^{eq}, about which particles oscillate if there are no thermostats.

In equilibrium conditions, i.e. if there are thermostats at same temperature acting on particles 1 and N, the mean distance of particle 1 from particles 0 and 2, and of particle N from particles $N-1$ and $N+1$ could be different from the mean distance between consecutive particles in the bulk of the chain. In fact, there would be different forces acting on these particles. On the other hand, physically one expects the symmetry of

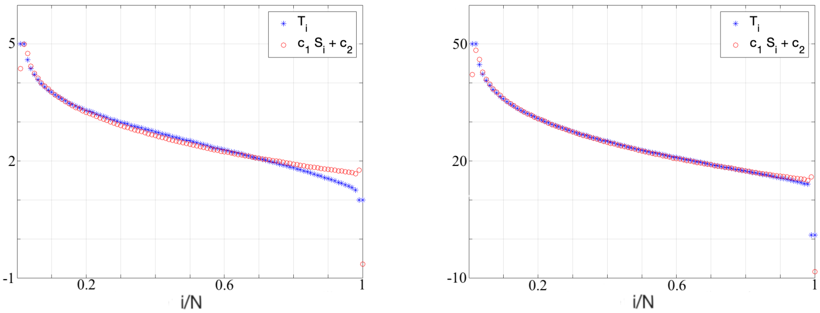

(A) $T_L = 5$

(B) $T_L = 50$

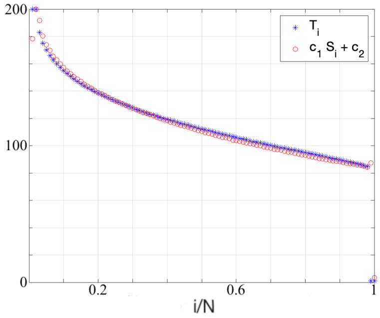

(C) $T_L = 200$

FIGURE 7.4: LJ chain with $N = 100$ and $T_R = 1$. Equation (7.3.4) with coefficients given by Eq.(7.3.5) is well verified. The S^{∞} profile is the one obtained at $T_L = 300$. Beyond this value, variations of this profile are not appreciable.

the potentials about the mechanical equilibrium positions to make equally spaced the bulk particles (that do not interact with thermostatted particles). The kinetic energy of all particles would also be uniform along the chain, therefore the state equation (7.2.7) would be trivially verified, i.e. with $c_1 = 0$, as usual at equilibrium.

Now, we consider β-FPUT chains with $a = 1$, $\alpha = 1$, and Nosé-Hoover thermostats at $T_R = 1$ and $T_L = 5$. Like in the case of harmonic chains studied in Ref.[36], we find that the inverse density profile, S, is practically flat, with $S_i = a$, apart from the region next to the walls and thermostats. This shows that the particles in the bulk oscillate about their mechanical equilibrium positions x_i^{eq}. Unlike harmonic chains, however, the kinetic temperature profile, T, monotonically decreases with the particle label i, interpolating between T_L and T_R, cf. Fig.7.5. This holds with different bath temperatures, as long $\alpha = 1$. In this case, (7.2.7) cannot hold because no factor c_1 turns the 0 angular coefficient of a horizontal line into a positive one. Consequently, the T and the S profiles are decoupled from each other, and cannot be related by an equation of state.

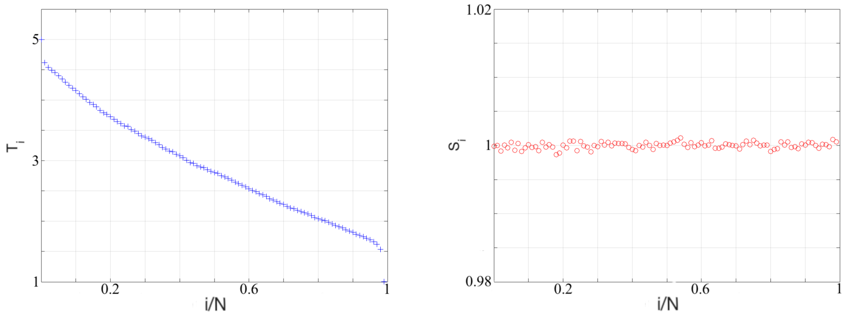

FIGURE 7.5: Profile of T (left) and S (right) for the $\beta-$FPUT chain with $N = 100$, $a = 1$ $\alpha = 1$, $T_L = 5$ and $T_R = 1$. The rest distance of particles is positive, hence they repel each other when they get too close. The length of the chain makes it neither stretched not compressed, on average. The profile of S is constant and equal to the equilibrium distance a, a part from negligible noise, magnified by the scale of the vertical axis.

Quite unexpectedly, then, the relation $F(P, S, T) = 0$ of Ref.[32], from which Eq.(7.2.7) could be obtained in the limit of small perturbations of the equilibrium state, does not apply, irrespective of the smallness of the perturbation. On the other hand, this is a singular condition that is strictly verified only at $\alpha = 1$, as far as simulations demonstrate. It signals that the chain behaviour drastically changes when passing from compressed to stretched.

We argue that such facts are consequence of the symmetry about the equilibrium positions of the forces acting on the oscillators. Symmetry tends to preserve the uniformity of the distribution of particles, as much as allowed by the contrasting effects of the boundary conditions.

As a matter of fact, the scenario changes for $\alpha \neq 1$, when the mechanical equilibrium positions (7.2.9) do not coincide anymore with the rest positions of the interaction

potential, which are points of symmetry for that potential.[4] Then, the forces acting on the particles appear generated by non-symmetric potentials, that contribute to break the spatial uniformity of the distribution of particles. The S and T profiles may then be coupled, and various possibilities arise.
For $\alpha < 1$, the chain is compressed, at "equilibrium" the pressure is positive, the gradients of the T and S profiles have same sign, and the constant c_1 is positive. This means that density is lower where the chain is hotter, which seems to be a normal condition. However, the relation (7.2.7) is not perfectly verified for $\alpha = 0.5$ and 0.8, as top row of Fig. 7.6 shows.

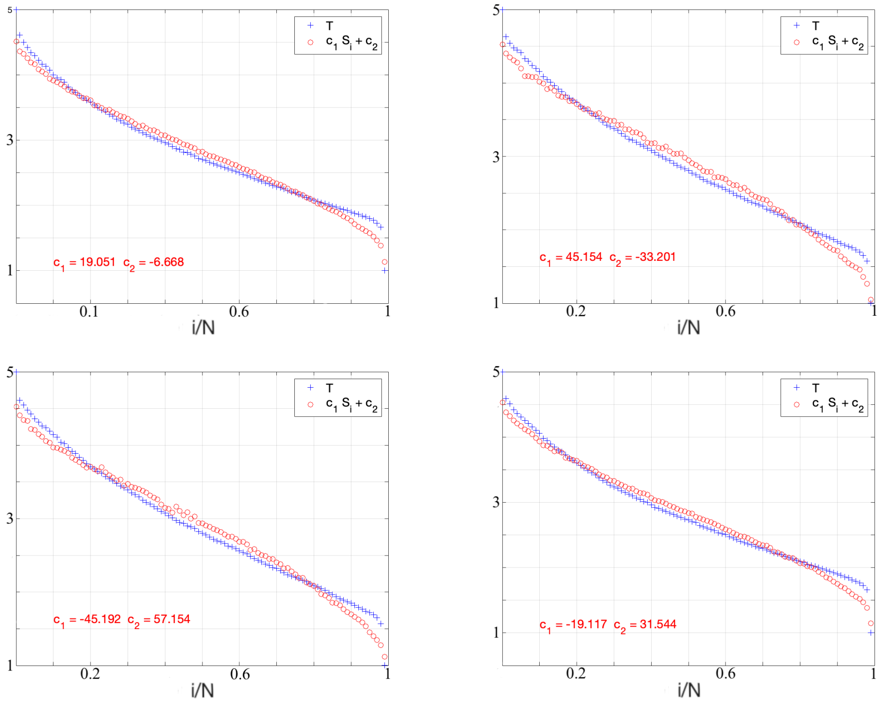

FIGURE 7.6: β−FPUT chain with $N = 100$, $a = 1$, and Nosé-Hoover thermostats at $T_L = 5$ and $T_R = 1$. Top row: the chain is compressed with $\alpha = 0.5$ (left) and $\alpha = 0.8$ (right). Bottom row: the chain is stretched with $\alpha = 1.2$ (left) and $\alpha = 1.5$ (right). Eq.(7.2.7) is better verified when α differs more from 1. Note the similarity of top left panel with bottom right panel, and of top right panel with bottom left panel. Under compression c_1 is positive. Under stretching it is negative.

Like under compression, Eq. (7.2.7) is only approximately verified when the chain is mildly stretched. Results from simulations with $a = 1$ and $\alpha = 1.2$ and 1.5 are reported in bottom row of Fig. 7.6. We may regard the range $1 < \alpha < 2$ analogous

---

[4] The case $a = 0$ means that the chain is always stretched and, indeed, we have found the same results obtained with $\alpha > 1$, hence we do not report them.

to $0 < \alpha < 1$ for shifting (with opposite sign) the chain mechanical equilibrium positions with respect to the rest positions of the interaction potential. Indeed, a similar performance of the linear relation is obtained. What matters is how much α differs from 1, whether larger or smaller. Note the similarity of the cases with $\alpha = 0.8$ and 1.2, and that of the cases with $\alpha = 0.5$ and 1.5. Relation (7.2.7) improves as $|1 - \alpha|$ grows; cf. left panel of the top row of Fig. 7.6, concerning the case $\alpha = 0.5$ and 0.8, with those of the top row of Fig. 7.6, for $\alpha = 1.2$ and 1.5.
Figure 7.7 provides an overview of the behaviour of the weakly deformed chain. As α departs from 1, growing or decreasing is the same, the mechanical equilibrium positions depart from the points of symmetry of the interaction potentials, and monotonic S profiles, which can be coupled with the monotonic profiles of T, immediately emerge: this appears to be a discontinuous non-equilibrium transition. Consequently, the linear relation (7.2.7) becomes verified, with varying degrees of accuracy.

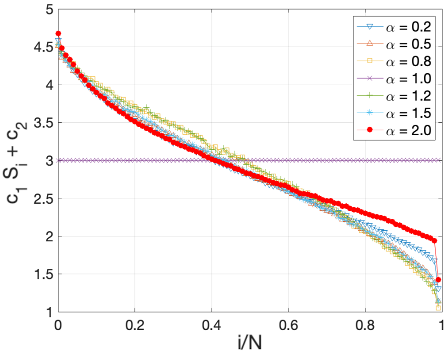

FIGURE 7.7: $\beta-$FPUT chain with $N = 100$, $a = 1$, and Nosé-Hoover thermostats at $T_R = 1$ and $T_L = 5$, and different values of α, in the interval $[0.2, 2]$. The sudden change of $c_1 S_i + c_2$, when α decreases or increases away from 1 is shown. For $\alpha = 1$, since the relation (7.2.7) does not work, we put $c_1 = 0$ and $c_2 = (T_L + T_R)/2 = 3$.

As c_1 and c_2 depend on the baths temperatures, it is interesting to study how they are related to each other. Having fixed T_R we have found the same behaviour observed for SPC and LJ, see Sec. 7.3.2 and 7.3.3, i.e. that both coefficients depend linearly on T_L at least up to a certain value, and then the dependence turns non-linear at higher T_L.

7.4.1 Effects of symmetry of potentials

As reported in Sec.7.4, the particles of the $\beta-$FPUT model, which has symmetric interaction potential, do not shift their mean position, even in presence of a temperature gradient, when the system is at its rest length ($\alpha = 1$). However, if we stretch or compress the chain, a mass gradient develops and can be coupled to the T profile. Moreover, some behaviour transition takes place as the stretching grows.

To understand why this happens, we have investigated the interactions changes that particles perceive under stretching. For the sake of definiteness we consider half of the potential acting on the generic i-th particle, i.e.:

$$V(r) = \frac{(r-a)^2}{2} + \frac{(r-a)^4}{4} , \tag{7.4.1}$$

where $r = r_i = x_{i+1} - x_i$ and a is the rest length of the spring. When the chain is neither stretched nor compressed ($\alpha = 1$), the mechanical equilibrium is expressed by $x_i^{eq} = i\,a$. In this case, the potential V is symmetric with respect to the mechanical equilibrium distance $r = r^{eq} = a$, and the density profiles are flat, in accord with the reasoning of Appendix A and the numerical data shown in Fig.7.5.
If we stretch the chain by a factor $\alpha > 1$, so that the distance between the two fixed particles at the ends of the chain is $\alpha(N+1)a$, the new equilibrium configuration is given by $\hat{x}_i^{eq} = i\,a\,\alpha \equiv i(a+d)$, where $d = a(\alpha - 1)$ is the distance between the stretched and the rest equilibrium positions. In this situation the particles oscillate about $\hat{x}_i^{eq}$ and the displacements r_i oscillate about $r = \hat{r}^{eq} = a + d$, which is neither a point of symmetry nor a minimum of V, see Fig. 7.8. Let us examine the effect of this asymmetry as the chain is stretched, and the vertical axis $r = \hat{r}^{eq}$ in Fig.7.8 is moved to the right of $r = a$ (corresponding to $d = 0$). In order to focus on the new equilibrium displacement $\hat{r}^{eq} = a + d$ we rewrite the potential V setting $r = \hat{r}^{eq} + z$ in (7.4.1), which yields:

(A) Unstrained (B) Strained

FIGURE 7.8: Under stretching the vertical axis indicating the equilibrium position is moved to the right.

$$V(r) \equiv V(\hat{r}^{eq} + z) = \frac{d^2}{2} + \frac{d^4}{4} + \widetilde{V}_\alpha(z)$$

with

$$\widetilde{V}_\alpha(z) = \mathbf{a}_1\, z + \mathbf{s}_2\, z^2 + \mathbf{a}_3\, z^3 + \mathbf{s}_4 z^4 , \tag{7.4.2}$$

where

$$\mathbf{a}_1 = d(1+d^2),\ \mathbf{s}_2 = \frac{1}{2}(1+3d^2),\ \mathbf{a}_3 = d,\ \mathbf{s}_4 = \frac{1}{4}.$$

The subscript α in (7.4.2) refers to the fact that the coefficients of the polinomial $\widetilde{V}_\alpha(z)$ via d depend on α. Indeed, the coefficients of the asymmetric terms (odd powers) in $\widetilde{V}_\alpha(z)$ are:

$$\mathbf{a}_1 = a(\alpha-1)(1+a^2(\alpha-1)^2), \quad \mathbf{a}_3 = a(\alpha-1),$$

and those of the symmetric one (even powers) are

$$\mathbf{s}_2 = \frac{1}{2}(1+3a^2(\alpha-1)^2), \quad \mathbf{s}_4 = \frac{1}{4}.$$

Obviously, the asymmetric coefficients vanish for $\alpha = 1$. Thus, in the case of a slightly stretched chain (*i.e.* for $\alpha \approx 1$) $\widetilde{V}_\alpha(z)$ is a small perturbation of the original symmetric potential that still dominates the dynamics. In the opposite limit, *i.e.* for a large stretching of the chain ($\alpha \gg 1$) the terms in the potential with the largest coefficients are the harmonic and the first order anharmonic ones, with $\mathbf{a}_1 \sim a^3(\alpha-1)^3$. More precisely, consider that anharmonic interactions are required for non-constant temperature profiles to be established, and that fluctuations of positions can be relatively large, *e.g.* $O(1)$. Then, for $a = 1$ or larger, we have the following:

1. For a stretching factor $\alpha = 1+\delta$ with $0 < \delta \ll 1$, (i.e. small $d > 0$), $\mathbf{a}_1, \mathbf{a}_3 = O(\delta)$ and $\mathbf{s}_2, \mathbf{s}_4 = O(1)$, then the nonlinear interaction is dominated by the symmetric potential terms $\mathbf{s}_2 z^2 + \mathbf{s}_4 z^4$ and, as in the case of β-FPUT with $\alpha = 1$, relation (7.2.7) fails.

2. For $\alpha \approx 1.5$ (i.e. $d \approx 0.5$), and deviations $z = O(1)$ from equilibrium, the amplitudes of symmetric and asymmetric terms, i.e. $\mathbf{s}_2 z^2 + \mathbf{s}_4 z^4$ and $\mathbf{a}_1 z + \mathbf{a}_3 z^3$, are of the same order (since the coefficients in (7.4.2) do the same) and the relation is only approximately satisfied (Fig. 7.6).

3. For $\alpha \approx 2$ (i.e. $d \approx 1$), and $z = O(1)$, the asymmetric nonlinear term becomes relevant. Indeed, $a \geq 1$ implies $\mathbf{a}_1 \geq \mathbf{s}_2, \mathbf{s}_4$ and the law (7.2.7) is almost perfectly satisfied (Fig. 7.7).

4. For $\alpha \gg 2$, we have $\mathbf{a}_1 > \mathbf{s}_2 > \mathbf{a}_3 > \mathbf{s}_4$ and, though the harmonic term is still dominant, the cubic term becomes increasingly important, since the coefficient of the quartic term $\mathbf{s}_4$ remains unchanged and equal to $1/4$. In this regime the particles become peculiarly correlated with each other and with the thermostats. Simulations in this regime are numerically challenging, so the possible results have to be further investigated.

We conclude that asymmetric interactions, whichever way they are generated, allow the validity of the equation of state (7.2.7), as long as they are not negligible.

This reasoning is consistent with simulations of a chain with this potential:

$$V(r) = \frac{g_2}{2}(r-a)^2 + \frac{g_3}{3}(r-a)^3 + \frac{g_4}{4}(r-a)^4 \,, \tag{7.4.3}$$

where $g_2 = g_4 = 1$ are constants and we study the validity of (7.2.7) modifying g_3. As we can see in top panels of Fig. 7.9, for $g_3 = 0.01$ the asymmetric term is totally dominated by the symmetric ones and the linear relation (7.2.7) is not satisfied. However, increasing the coefficient of the cubic term we can observe that the relation is better and better satisfied, cf. bottom panels of Fig. 7.9. Therefore, the mass gradient couples with the temperature gradient when the asymmetric term is not negligible, compared to the symmetric ones.

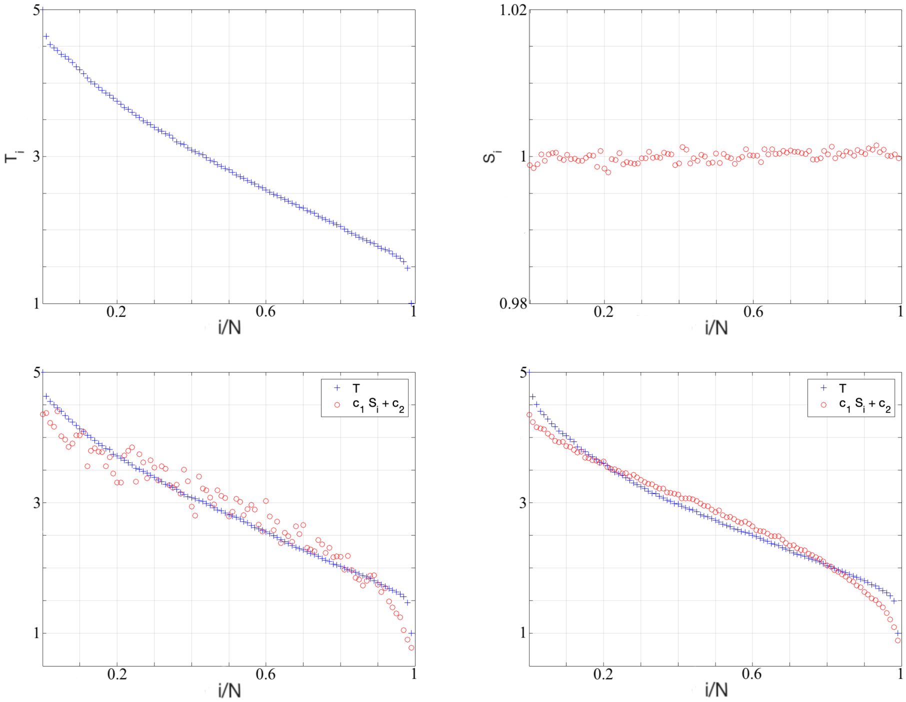

FIGURE 7.9: Top panels: the profiles of T and S for the chain with interacting potential (7.4.3) and $g_3 = 0.01$, $N = 100$, $a = 1$ $\alpha = 1$, $T_L = 5$, $T_R = 1$. In this case, the rest distance of particles is positive, hence particles repel each other when they get too close. However, even in the presence of a (small) cubic perturbation of the β-FPUT potential, the length of the chain makes it neither stretched nor compressed, on average. The profile of S is constant and equal to the equilibrium distance a, apart from negligible noise. Bottom panels: Linear relation (7.2.7) for the chain with interacting potential (7.4.3) and with $N = 100$, $a = 1$ $\alpha = 1$, $T_L = 5$ and $T_R = 1$. The coefficient of the cubic term of the potential is $g_3 = 0.1$ in the left panel and $g_3 = 1.0$ in the right one.

7.4.2 Stochastic baths

One may wonder whether the above results are due to the known peculiar nature of the Nosé-Hoover thermostat in 1-dimensional systems. As a matter of fact, the detailed structure of our results is affected by the thermal bath model, unlike what happens in real 3-dimensional thermodynamic systems, [15]. However, qualitatively they remain the same if the Nosé-Hoover thermostats are replaced by stochastic baths. Following Ref. [28], we implement such baths by simulating the elastic collisions of particles 1 and N with virtual Maxwellian bath particles at temperatures T_L and T_R, see Eqs. (41) and (42) of [28]. Moreover, the random number k of discrete time steps between two consecutive collision of a particle with the bath is assumed to have a geometric distribution:

$$P(k) = h(1-h)^{k-1} \quad , \tag{7.4.4}$$

where $h = \gamma \mathrm{d}t$, $\mathrm{d}t$ is the time step, and γ is a positive parameter such that $\gamma \mathrm{d}t \leq 1$, which determines the rate of interaction.
For β-FPUT with $T_R = 1$, $T_L = 5$ and $\mathrm{d}t = 10^{-3}$, we then varied α and γ, obtaining the following results:

$\alpha = 0.5$) Equation (7.2.7) holds with $c_1 > 0$, and thermostat efficiencies $\gamma = 10$, cf. Fig. 7.10a.

$\alpha = 1$) T profile monotonically decreases, while S profile is flat for $\gamma = 10$, cf. Fig. 7.10b. In this case, Eq. (7.2.7) does not work; density gradient and temperature gradients are decoupled.

$\alpha = 2$) T and S profiles have opposite trend, so the linear relation is verified with $c_1 < 0$. See Fig. 7.10c for $\gamma = 10$.

7.5 2-dimensional lattice

We briefly mention that an extension to 2-dimensional systems of Eq. (7.2.7) also holds. In this case, we consider a network with particles in positions $\mathbf{r}(i,j)$, $i = 1,\ldots,n_y$, $j = 1,\ldots,n_x$ in the plane (x,y). We have nearest neighbour harmonic interactions, with vanishing rest length, which means that the springs joining the particles are stretched. Then, particle labelled by (i,j) interact with particles labelled by $(i,j+1)$, $(i-1,j)$, $(i,j-1)$ and $(i+1,j)$. The boundary particles $\mathbf{r}(1,j), \mathbf{r}(n_y,j), \mathbf{r}(i,1), \mathbf{r}(i,n_x), i = 1,\ldots,n_y$, $j = 1,\ldots,n_x$ interact with wall particles that are at rest so that the positions $\mathbf{r}^{eq}(i,j) = (ai,aj)$ constitute the mechanical equilibrium configuration of the net. The particles on the left (L), $\mathbf{r}(i,1)$, also interact with a Nosé-Hoover thermostat at temperature T_L; those on the right (R), $\mathbf{r}(i,n_x)$, with a thermostat at temperature T_R. The kinetic temperature is defined by

$$T_{ij} = \left\langle v_{ij}^2 \right\rangle, \tag{7.5.1}$$

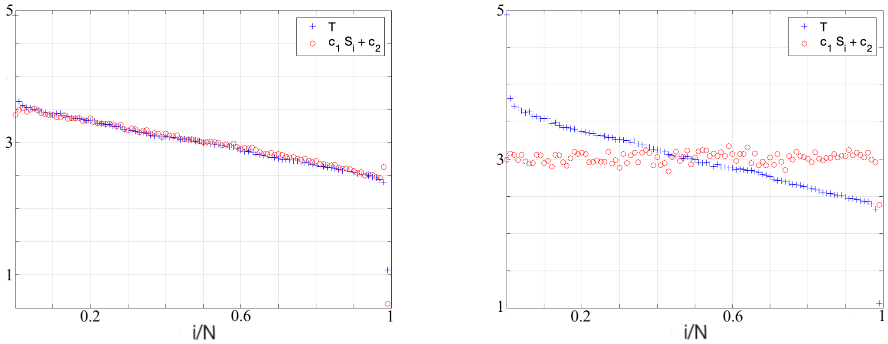

(A) $\gamma = 10$, $\alpha = 0.5$

(B) $\gamma = 10$, $\alpha = 1.0$

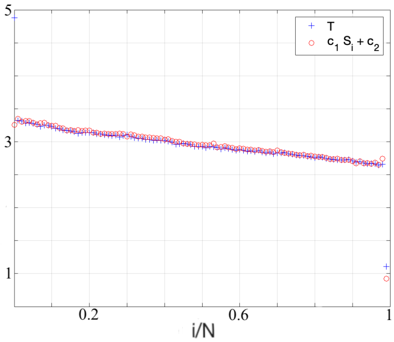

(C) $\gamma = 10$, $\alpha = 2.0$

FIGURE 7.10: FPUT chain with $N = 100$, $T_L = 5$ and $T_R = 1$, with stochastic baths. Top panels: stretching factor is $\alpha = 0.5$. Center panels: $\alpha = 1.0$, *i.e.* there is neither compression nor stretching. Bottom panels: stretching factor is $\alpha = 2.0$.

where $v_{ij} = \frac{d\mathbf{r}(i,j)}{dt}$ is the velocity of particle (i,j), while by inverse average distance of neighboring particles around the particle labelled by (i,j) we mean:

$$\left\langle S_{ij} \right\rangle = \frac{1}{4} \Big\langle |\mathbf{r}(i,j+1) - \mathbf{r}(i,j)| + |\mathbf{r}(i-1,j) - \mathbf{r}(i,j)| \\ + |\mathbf{r}(i,j-1) - \mathbf{r}(i,j)| \; + |\mathbf{r}(i+1,j) - \mathbf{r}(i,j)| \Big\rangle . \tag{7.5.2}$$

Our simulations show that, as common in 1-dimensional cases, the kinetic temperature in the center of the lattice gets higher than at the thermostatted boundaries[5]. On the other hand, unlike the one-dimensional temperature profile of the harmonic system, in the two dimensional one T_{ij} may be not flat in the bulk.

Now, we rewrite Eq. (7.2.7) for the particles labelled by (i,j) as:

$$\left\langle v_{ij}^2 \right\rangle = c_1 \, \rho_{ij}^{-1} + c_2, \tag{7.5.3}$$

where ρ_{ij} is the average density at (i,j). Because in two dimensions one may take ρ_{ij} as proportional to the inverse of a square distance, *i.e.* $\rho_{ij} \propto \langle S_{ij} \rangle^{-2}$, we obtain:

$$\left\langle v_{i,j}^2 \right\rangle = c_3 \, \left\langle S_{ij} \right\rangle^2 + c_4. \tag{7.5.4}$$

This prediction is confirmed by a numerical quadratic fit. We do not mention any other details here, except that an example in which (7.5.4) can be verified is, for instance, a 20 × 20 lattice with $T_L = 10$ and $T_R = 1$.

7.6 Concluding remarks

In this paper we have shown that Eq. (7.2.7) holds quite widely, and can be considered a state equation for 1-dimensional chains of oscillators. Was c_2 negligible, we would have had Boyle's law, but in general c_2 is not negligible, and it even gets larger for larger temperature jumps. This characterizes a non-standard state of aggregation of matter.

In certain regions of the parameter space, Eq. (7.2.7) fails, especially for the β-FPUT potential. In particular, Eq. (7.2.7) does not hold in $\beta-$FPUT chains when the mechanical equilibrium configuration of the chain constitutes a lattice whose nodes lie in the rest positions of the interaction potential, which is symmetric with respect to such positions. In that case, T is monotonic, thanks to the presence of nonlinear interactions, but S remains flat, hence the two profiles cannot be matched by a relation like (7.2.7).

---

[5] For instance, such a behavior i.e. $T_i > \max\{T_L, T_R\}$, can be observed in the bulk of a stretched 1-dimensional $\beta-$FPUT model with $N = 100$, $T_L = 5$, $T_R = 1$ and $\alpha > 3.5$.

The β-FPUT chains are peculiar, because their potential is symmetric, it confines particles more strongly than harmonic potentials, and it does not preserve their initial order. Nevertheless, this failure carries information about a significant change of behaviour, associated with a change of sign of pressure: in a range of values of the dilatation factor α around 1, the pressure is non-zero, and Eq. (7.2.7) holds.

In the harmonic cases, Eq. (7.2.7) is verified because both S and T profiles are flat, therefore it suffices to take $c_1 = 0$ and $c_2 = T$.

For non-linear interactions, the T profile typically interpolates monotonically between T_L and T_R, and S is monotonic, in such a way that values c_1 and c_2 can be found for Eq. (7.2.7) to represent the data. This is the case of the harmonic+hard core, LJ and SPC potentials. As changing bath temperatures one obtains different S and T profiles, c_1 and c_2 change too. The question is whether they follow any rule. As a matter of fact, they vary linearly with T_L up to quite large values of the difference $T_L - T_R$, and then they bend toward a nonlinear regime for still higher values. This has been observed to be the case for the β-FPUT, the SPC and the nearest neighbour LJ potentials. Furthermore, Eq.(7.2.7) holds even under time averaging not sufficient to yield the stationary state S and T profiles. This fact further shows that Eq.(7.2.7) goes beyond a thermodynamic law.

Noteworthy is the behaviour under compression or extension of the chains. The $\beta-$FPUT cases, in particular, present a variety of situations, in which the applicability of Eq. (7.2.7) alternates. Stretching or compressing the chain, the equilibrium positions of the particles in the chain shift with respect to the minimum of the pair interaction potential. Consequently, the particles in the bulk of the chain are subjected to potentials that appear symmetric or asymmetric, depending on the (a)symmetry of the interaction potential. The (a)symmetry depends on the stretching parameter α: changing α, the potential about the mechanical equilibrium positions changes from being dominated by its quadratic term, which is symmetric and not capable of producing a monotonic T profile, to being sensibly asymmetric, thanks to the linear and cubic terms. This is accompanied by transition regions in the range of α, in which the state equation (7.2.7) holds, to regions in which it does not. Such variations of behaviour occur because the volume (or inverse density) gets at times decoupled from the temperature.

In particular, varying α, flat S profiles acquire a slope, and gradually couple to the T profile via relation (7.2.7). The respective gradients have same sign, hence $c_1 > 0$, when $\alpha < 1$, *i.e.* positive pressure, while they have opposite sign, hence $c_1 < 0$, when $\alpha > 1$, *i.e.* negative pressure. Consequently, the applicability of Eq.(7.2.7) changes.

Notably, the linear state equation linking temperature and inverse density holds also in 2-dimensional systems, once the density is properly defined, considering that volume corresponds to squared distances, cf. equations (7.5.3) and (7.5.4).

The above suggests that Eq.(7.2.7) is a non-trivial relation, although simple and concerning the two most obvious observables of particles systems. It appears suitable to play the role of an equation of state for equilibrium (where it holds trivially), and non-equilibrium (even non-stationary and non-thermodynamic) states of oscillators networks. It distinguishes qualitatively different situations, for a wide set of systems. It characterizes states in a simple fashion, involving a small set of parameters, without detailed knowledge of the dynamics, as required of usual equilibrium thermodynamic equations of state, although it strictly is a microscopic relation.

Appendix A. Remark on flat density profiles

A peculiar fact concerning the $\beta-$FPUT model is that the S profile is flat even in non-equilibrium conditions, see Sec.7.4. In this appendix we discuss how the symmetry of the potential may induce this phenomenon. The natural situation in which the profile of S is flat is obviously the equilibrium condition, as a simple canonical computation (at temperature T) of the mean position of the $i-$th particle $\langle x_i \rangle$ shows. Indeed, defining $y_j = x_j - ja$, the average can be rewritten as follows:

$$\langle x_i \rangle = ia + C \int y_i \exp\left\{ -\beta \sum_{j=0}^{N} W(y_{j+1} - y_j) \right\} dy_1 \cdots dy_N \,, \tag{7.6.1}$$

where $\beta = (k_B T)^{-1}$, $y_0 = 0$, $y_{N+1} = 0$, $W(r) = r^2/2 + r^4/4$ comes from the $\beta-$FPUT potential (7.2.5) and $C > 0$ is the quotient between the kinetic part of the integral and the partition function. Since the integrand in (7.6.1) is odd, the integral vanishes, showing that $\langle x_i \rangle = ia$, that means that the S profile is flat.

For symmetry reason the flat profile is to be expected at equilibrium whatever nearest-neighbour potential is applied (provided that $x_i = ia$ is the stable mechanical equilibrium point), since the particles in the bulk are under the same forces from their left and their right neighbours. The result is like a symmetric potential that makes the average deviation from the equilibrium position null. Indeed, in the limit of small displacements y_i (to be expected at equilibrium) the potential in (7.6.1) is closely approximated by a positive definite quadratic form $W(y_1, \ldots, y_N) \simeq \sum_{i,j} q_{ij} y_i y_j$. As a consequence the integrand in (7.6.1) is odd and the integral vanishes.

In the case of a system in contact with two thermostats at different temperatures, $T_L \neq T_R$, this cannot be done because the system is out of equilibrium and the temperature of the chain as a whole does not exist. Then, we assume that a state of local equilibrium is achieved in which the temperature can be defined locally. Motivated by the observation that the mechanical properties of a chain (such as the modulus of elasticity) are expected to depend on the temperature [29], one may assume a temperature dependent profile of the constants that control the strength of the interaction between the particles. More precisely, we may introduce new versions of the $\beta-$FPUT or $\alpha\beta-$FPUT models, by modifying the potential (7.4.3), as follows:

$$\widetilde{V}_{g_3,i}(r) = \gamma_i \left(\frac{(r-a)^2}{2} + g_3 \frac{(r-a)^3}{3} + \frac{(r-a)^4}{4} \right) \,, \tag{7.6.2}$$

where the variability of $\gamma_i > 0$ with i embodies the dependence of these constants on the local temperatures T_i. Then we replace the canonical ensemble used above with one in which β is "absorbed" into the γ_i's and the original potential is replaced by $\widetilde{V}_{g_3,i}$. A similar approach is followed under various hypotheses in numerous works, see *e.g.* [38, 39].

The mean position of the $i-$th particle of the modified FPUT models, is:

$$\langle x_i \rangle = ia + C \int y_i \exp\left\{ -\sum_{j=0}^{N} \widetilde{W}_{g_3,i}(y_{j+1} - y_j) \right\} dy_1 \cdots dy_N \,, \tag{7.6.3}$$

where $\widetilde{W}_{g_3,i}(r) = \gamma_i(r^2/2 + g_3 r^3/3 + r^4/4)$ and $y_j = x_j - ja$. In the case of the $\beta-$FPUT model, obtained by setting $g_3 = 0$, the integrand in (7.6.3) is odd, implying that $\langle x_i \rangle = ia$, even in the presence of a temperature gradient along the chain. On the other hand, in the case the asymmetric $\alpha\beta$-FPUT potential, that is (7.6.2) with $g_3 \neq 0$, the reasoning based on the symmetry of the forces from both sides of a particle seems not to work because of the inhomogeneity introduced by the γ_i's. To see that, it suffices to consider a system with one particle linked to two fixed particles in the position 0 and $2a$, respectively. We obtain:

$$\langle x \rangle = a + C \int \mathrm{d}y\, y \exp\left\{ - \left[(\gamma_1 + \gamma_2) \left(\frac{y^2}{2} + \frac{y^4}{4} \right) + (\gamma_1 - \gamma_2) \frac{y^3}{3} \right] \right\}, \tag{7.6.4}$$

in which the integral vanishes only if $\gamma_1 = \gamma_2$. In the general case with N particles, one can verify numerically that the integral does not vanish if the γ_i's are different. This discussion suggests, in accordance with our simulations, that the mean position of a particle under symmetric potentials does not depend on the temperature. This holds whether there is or there is no temperature gradient. On the contrary, asymmetric potentials lead to temperature dependent position profiles.

Bibliography

References for Chapter 1

[1] Wei Yang and Walter Rocchia. "Biomolecular Electrostatic Phenomena: An Evergreen Field". *The Journal of Physical Chemistry B* 127 PMID: 37165646, pp. 3979–3981, 2023. DOI: `10.1021/acs.jpcb.3c02158`. eprint: `https://doi.org/10.1021/acs.jpcb.3c02158`.

[2] Elena Besley. "Recent Developments in the Methods and Applications of Electrostatic Theory". *Accounts of Chemical Research* 56 PMID: 37585560, pp. 2267–2277, 2023. DOI: `10.1021/acs.accounts.3c00068`. eprint: `https://doi.org/10.1021/acs.accounts.3c00068`.

[3] Luc Belloni. "Colloidal interactions". *Journal of Physics: Condensed Matter* 12, R549, 2000.

[4] Jean-Pierre Hansen and Hartmut Löwen. "Effective interactions between electric double layers". *Annual Review of Physical Chemistry* 51, pp. 209–242, 2000.

[5] Sergio Decherchi and Walter Rocchia. "A general and Robust Ray-Casting-Based Algorithm for Triangulating Surfaces at the Nanoscale". *PLOS ONE* 8, pp. 1–15, 2013. DOI: `10.1371/journal.pone.0059744`.

[6] Remo Rohs, Sean M. West, Alona Sosinsky, Peng Liu, Richard S. Mann, and Barry Honig. "The role of DNA shape in protein–DNA recognition". *Nature* 461, pp. 1248–1253, 2009. DOI: `10.1038/nature08473`. eprint: `https://doi.org/10.1038/nature08473`.

[7] Lin Li, Chuan Li, Subhra Sarkar, Jie Zhang, Shawn Witham, Zhe Zhang, Lin Wang, Nicholas Smith, Marharyta Petukh, and Emil Alexov. "DelPhi: a comprehensive suite for DelPhi software and associated resources". *BMC biophysics* 5, pp. 1–11, 2012.

[8] Nathan A Baker, David Sept, Simpson Joseph, Michael J Holst, and J Andrew McCammon. "Electrostatics of nanosystems: application to microtubules and the ribosome". *Proceedings of the National Academy of Sciences* 98, pp. 10037–10041, 2001.

[9] Jun Wang and Ray Luo. "Assessment of linear finite-difference Poisson–Boltzmann solvers". *Journal of computational chemistry* 31, pp. 1689–1698, 2010.

[10] Robert C Harris, Alexander H Boschitsch, and Marcia O Fenley. "Influence of grid spacing in Poisson-Boltzmann equation binding energy estimation". *Journal of chemical theory and computation* 9, pp. 3677–3685, 2013.

[11] Alexander H Boschitsch, Marcia O Fenley, and Huan-Xiang Zhou. "Fast boundary element method for the linear Poisson- Boltzmann equation". *The Journal of Physical Chemistry B* 106, pp. 2741–2754, 2002.

[12] Christopher D Cooper, Jaydeep P Bardhan, and Lorena A Barba. "A biomolecular electrostatics solver using Python, GPUs and boundary elements that can handle solvent-filled cavities and Stern layers". *Computer physics communications* 185, pp. 720–729, 2014.

[13] Stephen D Bond, Jehanzeb Hameed Chaudhry, Eric C Cyr, and Luke N Olson. "A first-order system least-squares finite element method for the Poisson-Boltzmann equation". *Journal of computational chemistry* 31, pp. 1625–1635, 2010.

[14] Michael Holst, James Andrew Mccammon, Zeyun Yu, YC Zhou, and Yunrong Zhu. "Adaptive finite element modeling techniques for the Poisson-Boltzmann equation". *Communications in computational physics* 11, pp. 179–214, 2012.

[15] Ilkay Sakalli, J Schoberl, and EW Knapp. "mFES: a robust molecular finite element solver for electrostatic energy computations". *Journal of chemical theory and computation* 10, pp. 5095–5112, 2014.

[16] Junji Iwahara, B Montgomery Pettitt, and Binhan Yu. "Direct measurements of biomolecular electrostatics through experiments". *Current Opinion in Structural Biology* 82, p. 102680, 2023.

[17] Binhan Yu, Xi Wang, and Junji Iwahara. "Measuring local electrostatic potentials around nucleic acids by paramagnetic NMR spectroscopy". *The journal of physical chemistry letters* 13, pp. 10025–10029, 2022.

References for Chapter 2

[1] Malcolm E Davis and J Andrew McCammon. "Electrostatics in biomolecular structure and dynamics". *Chemical Reviews* 90, pp. 509–521, 1990.

[2] G Andrés Cisneros, Mikko Karttunen, Pengyu Ren, and Celeste Sagui. "Classical electrostatics for biomolecular simulations". *Chemical reviews* 114, pp. 779–814, 2014.

[3] Curt M Breneman and Kenneth B Wiberg. "Determining atom-centered monopoles from molecular electrostatic potentials. The need for high sampling density in formamide conformational analysis". *Journal of computational chemistry* 11, pp. 361–373, 1990.

[4] Mark R Wilson. "Progress in computer simulations of liquid crystals". *International Reviews in Physical Chemistry* 24, pp. 421–455, 2005.

[5] Barry Honig and Anthony Nicholls. "Classical electrostatics in biology and chemistry". *Science* 268, pp. 1144–1149, 1995.

[6] Charles L Brooks III, Martin Karplus, B Montgomery Pettitt, and Robert H Austin. *Proteins: a theoretical perspective of dynamics, structure and thermodynamics*. 1990.

[7] Margaret Robson Wright. *An introduction to aqueous electrolyte solutions*. John Wiley & Sons, 2007.

[8] Benoıt Roux and Thomas Simonson. “Implicit solvent models”. *Biophysical chemistry* 78, pp. 1–20, 1999.

[9] John O’M Bockris and Amulya KN Reddy. “Ion-ion interactions”. *Modern Electrochemistry 1: Ionics*, pp. 225–360, 1998.

[10] John O’M Bockris and Amulya KN Reddy. “Ion-solvent interactions”. *Modern Electrochemistry 1: Ionics*, pp. 35–224, 1998.

[11] Spiros Kournopoulos, Mirella Simões Santos, Srikanth Ravipati, Andrew J Haslam, George Jackson, Ioannis G Economou, and Amparo Galindo. “The contribution of the ion–ion and ion–solvent interactions in a molecular thermodynamic treatment of electrolyte solutions”. *The Journal of Physical Chemistry B* 126, pp. 9821–9839, 2022.

[12] Johan Scheers, Leszek Niedzicki, Grażyna Z Żukowska, Patrik Johansson, Władysław Wieczorek, and Per Jacobsson. “Ion–ion and ion–solvent interactions in lithium imidazolide electrolytes studied by Raman spectroscopy and DFT models”. *Physical Chemistry Chemical Physics* 13, pp. 11136–11147, 2011.

[13] Yan-Zhen Wei, Ping Chiang, and S Sridhar. “Ion size effects on the dynamic and static dielectric properties of aqueous alkali solutions”. *The Journal of chemical physics* 96, pp. 4569–4573, 1992.

[14] Xiang Ji and Shenggao Zhou. “Variational approach to concentration dependent dielectrics with the Bruggeman model: Theory and numerics”. *Communications in Mathematical Sciences* 17, pp. 1949–1974, 2019.

[15] Max Born. “Volumen und hydratationswärme der ionen”. *Zeitschrift für physik* 1, pp. 45–48, 1920.

[16] Jacob N Israelachvili. *Intermolecular and surface forces*. Academic press, 2011.

[17] Kenno Vanommeslaeghe, E Prabhu Raman, and Alexander D MacKerell Jr. “Automation of the CHARMM General Force Field (CGenFF) II: assignment of bonded parameters and partial atomic charges”. *Journal of chemical information and modeling* 52, pp. 3155–3168, 2012.

[18] A van Bondi. “van der Waals Volumes and Radii”. *The Journal of physical chemistry* 68, pp. 441–451, 1964.

[19] Sergio Decherchi, Jose Colmenares, Chiara Eva Catalano, Michela Spagnuolo, Emil Alexov, and Walter Rocchia. “Between Algorithm and Model: Different Molecular Surface Definitions for the Poisson-Boltzmann Based Electrostatic Characterization of Biomolecules in Solution”. *Communications in Computational Physics* 13, pp. 61–89, 2013. DOI: `10.4208/cicp.050711.111111s`.

[20] Herbert Edelsbrunner. “Geometry for modeling biomolecules”. *Robotics: The Algorithmic Perspective (Proc. 3rd WAFR)*, pp. 265–277, 1998.

[21] Sergio Decherchi and Walter Rocchia. "A general and Robust Ray-Casting-Based Algorithm for Triangulating Surfaces at the Nanoscale". *PLOS ONE* 8, pp. 1–15, 2013. DOI: `10.1371/journal.pone.0059744`.

[22] Sergio Decherchi, Andrea Spitaleri, John Stone, and Walter Rocchia. "NanoShaper–VMD interface: computing and visualizing surfaces, pockets and channels in molecular systems". *Bioinformatics* 35, pp. 1241–1243, 2018. DOI: `10.1093/bioinformatics/bty761`.

[23] Byungkook Lee and Frederic M Richards. "The interpretation of protein structures: estimation of static accessibility". *Journal of molecular biology* 55, 379–IN4, 1971.

[24] Michael L Connolly. "Analytical molecular surface calculation". *Applied Crystallography* 16, pp. 548–558, 1983.

[25] Otto Stern. "Zur theorie der elektrolytischen doppelschicht". *Zeitschrift für Elektrochemie und angewandte physikalische Chemie* 30, pp. 508–516, 1924.

[26] H von Helmholtz. "Ueber einige Gesetze der Vertheilung elektrischer Ströme in körperlichen Leitern, mit Anwendung auf die thierisch-elektrischen Versuche (Schluss.)" *Annalen der Physik* 165, pp. 353–377, 1853.

[27] MJJPTA Gouy. "Sur la constitution de la charge électrique à la surface d'un électrolyte". *J. Phys. Theor. Appl.* 9, pp. 457–468, 1910.

[28] David Leonard Chapman. "LI. A contribution to the theory of electrocapillarity". *The London, Edinburgh, and Dublin philosophical magazine and journal of science* 25, pp. 475–481, 1913.

[29] Von P Debye. "Zur theorie der electrolyte". *Phyikalishce Zeitschrift.*, pp. 185–206, 1923.

[30] John G Kirkwood. "Theory of solutions of molecules containing widely separated charges with special application to zwitterions". *The Journal of Chemical Physics* 2, pp. 351–361, 1934.

[31] Peter William Atkins, Julio De Paula, and James Keeler. *Atkins' physical chemistry*. Oxford university press, 2023.

[32] Terrell L Hill. *An introduction to statistical thermodynamics*. Courier Corporation, 1986.

[33] Itamar Borukhov, David Andelman, and Henri Orland. "Steric effects in electrolytes: A modified Poisson-Boltzmann equation". *Physical review letters* 79, p. 435, 1997.

[34] AC Maggs and R Podgornik. "General theory of asymmetric steric interactions in electrostatic double layers". *Soft matter* 12, pp. 1219–1229, 2016.

[35] EG Flekkøy, G Wagner, and J Feder. "Hybrid model for combined particle and continuum dynamics". *Europhysics Letters* 52, p. 271, 2000.

[36] Khaled M Mohamed and AA Mohamad. "A review of the development of hybrid atomistic–continuum methods for dense fluids". *Microfluidics and Nanofluidics* 8, pp. 283–302, 2010.

[37] Yan Levin and Michael E Fisher. "Criticality in the hard-sphere ionic fluid". *Physica A: Statistical Mechanics and its Applications* 225, pp. 164–220, 1996.

[38] Ralf Blossey. In: "The Poisson-Boltzmann Equation". Pp. 1–25. Cham: Springer International Publishing, 2023. DOI: `10.1007/978-3-031-24782-8`.

[39] Kim A Sharp and Barry Honig. "Calculating total electrostatic energies with the nonlinear Poisson-Boltzmann equation". *Journal of Physical Chemistry* 94, pp. 7684–7692, 1990.

[40] Dan Ben-Yaakov, David Andelman, and Rudi Podgornik. "Dielectric decrement as a source of ion-specific effects". *The Journal of chemical physics* 134, 2011.

[41] Dan Ben-Yaakov, David Andelman, Daniel Harries, and Rudi Podgornik. "Beyond standard Poisson–Boltzmann theory: ion-specific interactions in aqueous-solutions". *Journal of Physics: Condensed Matter* 21, p. 424106, 2009.

[42] Itamar Borukhov, David Andelman, and Henri Orland. "Adsorption of large ions from an electrolyte solution: a modified Poisson–Boltzmann equation". *Electrochimica Acta* 46, pp. 221–229, 2000.

[43] Guillaume Tresset. "Generalized Poisson-Fermi formalism for investigating size correlation effects with multiple ions". *Physical Review E—Statistical, Nonlinear, and Soft Matter Physics* 78, p. 061506, 2008.

[44] Bo Li. "Minimization of electrostatic free energy and the Poisson–Boltzmann equation for molecular solvation with implicit solvent". *SIAM Journal on Mathematical Analysis* 40, pp. 2536–2566, 2009.

[45] Alan D McNaught, Andrew Wilkinson, et al. *Compendium of chemical terminology*. Vol. 1669. Blackwell Science Oxford, 1997.

[46] Dan Ben-Yaakov, David Andelman, Rudi Podgornik, and Daniel Harries. "Ion-specific hydration effects: Extending the Poisson-Boltzmann theory". *Current Opinion in Colloid & Interface Science* 16, pp. 542–550, 2011.

[47] Yan-Zhen Wei and S Sridhar. "Dielectric spectroscopy up to 20 GHz of LiCl/H2O solutions". *The Journal of chemical physics* 92, pp. 923–928, 1990.

[48] Richard Buchner, Glenn T Hefter, and Josef Barthel. "Dielectric relaxation of aqueous NaF and KF solutions". *Journal of the Chemical Society, Faraday Transactions* 90, pp. 2475–2479, 1994.

[49] Nir Gavish and Keith Promislow. "Dependence of the dielectric constant of electrolyte solutions on ionic concentration: A microfield approach". *Physical review E* 94, p. 012611, 2016.

References for Chapter 3

[1] John G Kirkwood. "Theory of solutions of molecules containing widely separated charges with special application to zwitterions". *The Journal of Chemical Physics* 2, pp. 351–361, 1934.

[2] Huan-Xiang Zhou and Xiaodong Pang. “Electrostatic interactions in protein structure, folding, binding, and condensation”. *Chemical reviews* 118, pp. 1691–1741, 2018.

[3] Michael E Fisher, Yan Levin, and Xiaojun Li. “The interaction of ions in an ionic medium”. *The Journal of chemical physics* 101, pp. 2273–2282, 1994.

[4] OI Obolensky, TP Doerr, and Yi-Kuo Yu. “Rigorous treatment of pairwise and many-body electrostatic interactions among dielectric spheres at the Debye–Hückel level”. *The European Physical Journal E* 44, pp. 1–18, 2021.

[5] S. V. Siryk, A. Bendandi, A. Diaspro, and W. Rocchia. “Charged dielectric spheres interacting in electrolytic solution: a linearized Poisson-Boltzmann equation model”. *J. Chem. Phys.* 155, p. 114114, 2021.

[6] S. Siryk and W. Rocchia. “Arbitrary-Shape Dielectric Particles Interacting in the Linearized Poisson-Boltzmann Framework: An Analytical Treatment”. *J. Phys. Chem. B* 126, pp. 10400–10426, 2022.

[7] Kim A Sharp and Barry Honig. “Calculating total electrostatic energies with the nonlinear Poisson-Boltzmann equation”. *Journal of Physical Chemistry* 94, pp. 7684–7692, 1990.

[8] Walter Rocchia, Emil Alexov, and Barry Honig. “Extending the applicability of the nonlinear Poisson-Boltzmann equation: multiple dielectric constants and multivalent ions”. *The Journal of Physical Chemistry B* 105, pp. 6507–6514, 2001.

[9] Mauricio Guerrero-Montero, Michał Bosy, and Christopher D Cooper. “Some Challenges of Diffused Interfaces in Implicit-Solvent Models”. *Journal of Computational Chemistry* 46, e70036, 2025.

[10] J. D. Jackson. *Classical electrodynamics*. 3rd ed. London, Sydney, Singapore, New York: John Wiley & Sons Ltd, 1999.

[11] Y.-K. Yu. “Electrostatics of charged dielectric spheres with application to biological systems. III. Rigorous ionic screening at the Debye-Hückel level”. *Physical Review E* 102, p. 052404, 2020.

[12] O. I. Obolensky, T. P. Doerr, and Yi-Kuo Yu. “Rigorous treatment of pairwise and many-body electrostatic interactions among dielectric spheres at the Debye-Hückel level”. *Eur. Phys. J. E* 44, p. 129, 2021.

[13] W. Rocchia. “Poisson-Boltzmann equation boundary conditions for biological applications”. *Mathematical and Computer Modelling* 41 Modelling Complex Systems in Molecular Biology and Tumor Dynamics and Control, pp. 1109–1118, 2005. DOI: `https://doi.org/10.1016/j.mcm.2005.05.006`.

References for Chapter 4

[1] David S Malkus and Thomas JR Hughes. “Mixed finite element methods – reduced and selective integration techniques: a unification of concepts”. *Computer Methods in Applied Mechanics and Engineering* 15, pp. 63–81, 1978.

[2] J.E. Roberts and J.-M. Thomas. "Mixed and hybrid methods". In: *Finite Element Methods (Part 1)*. Vol. 2. Handbook of Numerical Analysis. Elsevier, 1991. Pp. 523–639. DOI: `https://doi.org/10.1016/S1570-8659(05)80041-9`.

[3] Thomas H. Robey. "The primal mixed finite element method and the LBB condition". *Numerical Methods for Partial Differential Equations* 8, pp. 357–379, 1992. DOI: `https://doi.org/10.1002/num.1690080405`. eprint: `https://onlinelibrary.wiley.com/doi/pdf/10.1002/num.1690080405`.

[4] O. C. Zienkiewicz, R. L. Taylor, and J. Z. Zhu. *The finite element method*. Vol. 1. Butterworth-Heinemann Oxford, UK, 2013.

[5] Pasquale Claudio Africa, Carlo de Falco, and Simona Perotto. "Scalable recovery-based adaptation on Cartesian quadtree meshes for advection-diffusion-reaction problems". *Advances in Computational Science and Engineering* 1, pp. 443–473, 2023. DOI: `10.3934/acse.2023018`.

[6] Federico Gatti, Marco Fois, Carlo de Falco, Simona Perotto, and Luca Formaggia. "Parallel simulations for fast-moving landslides: Space-time mesh adaptation and sharp tracking of the wetting front". *International Journal for Numerical Methods in Fluids* 95, pp. 1286–1309, 2023. DOI: `https://doi.org/10.1002/fld.5186`. eprint: `https://onlinelibrary.wiley.com/doi/pdf/10.1002/fld.5186`.

[7] Daniele Boffi, Franco Brezzi, and Michel Fortin. In: "Algebraic Aspects of Saddle Point Problems". Pp. 123–195. Berlin, Heidelberg: Springer Berlin Heidelberg, 2013. DOI: `10.1007/978-3-642-36519-5\_3`.

[8] D. Boffi, F. Brezzi, and M. Fortin. *Mixed Finite Element Methods and Applications*. Vol. 44. Springer Series in Computational Mathematics. Berlin Heidelberg: Springer-Verlag, 2013.

[9] Jean-Claude Nédélec. "Mixed finite elements in $\mathbb{R}^3$". *Numerische Mathematik* 35, pp. 315–341, 1980.

[10] Jean-Claude Nédélec. "A new family of mixed finite elements in $\mathbb{R}^3$". *Numerische Mathematik* 50, pp. 57–81, 1986.

[11] Hassler Whitney. *Geometric Integration Theory*. Princeton, N. J.: Princeton University Press, 1957.

[12] Wei Cai. In: "Computational Methods for Electromagnetic Phenomena: electrostatics in solvation, scattering, and electron transport". Pp. 205–227. Cambridge University Press, 2013.

[13] Olgierd Cecil Zienkiewicz, Robert Leroy Taylor, Perumal Nithiarasu, and JZ Zhu. *The finite element method*. Vol. 3. McGraw-Hill, 1977.

[14] Jinchao Xu and Ludmil Zikatanov. "A monotone finite element scheme for convection-diffusion equations". *Mathematics of Computation* 68, pp. 1429–1446, 1999.

[15] Peter A Markowich and Miloš A Zlámal. "Inverse-average-type finite element discretizations of selfadjoint second-order elliptic problems". *Mathematics of computation* 51, pp. 431–449, 1988.

[16] Sergio Decherchi and Walter Rocchia. "A general and Robust Ray-Casting-Based Algorithm for Triangulating Surfaces at the Nanoscale". *PLOS ONE* 8, pp. 1–15, 2013. DOI: `10.1371/journal.pone.0059744`.

[17] Anna-Karin Tornberg and Björn Engquist. "Numerical approximations of singular source terms in differential equations". *Journal of Computational Physics* 200, pp. 462–488, 2004.

[18] Bamdad Hosseini, Nilima Nigam, and John M. Stockie. "On regularizations of the Dirac delta distribution". *Journal of Computational Physics* 305, pp. 423–447, 2016. DOI: `https://doi.org/10.1016/j.jcp.2015.10.054`.

[19] Arum Lee, Weihua Geng, and Shan Zhao. "Regularization methods for the Poisson-Boltzmann equation: comparison and accuracy recovery". *Journal of Computational Physics* 426, p. 109958, 2021.

[20] Carlo de Falco. *bimpp*. `https://www.github.com/bimpp`. Accessed: 2024-12-23.

[21] Sergio Decherchi, Andrea Spitaleri, John Stone, and Walter Rocchia. "NanoShaper–VMD interface: computing and visualizing surfaces, pockets and channels in molecular systems". *Bioinformatics* 35, pp. 1241–1243, 2018. DOI: `10.1093/bioinformatics/bty761`.

[22] Carsten Burstedde, Lucas C. Wilcox, and Omar Ghattas. "`p4est`: Scalable Algorithms for Parallel Adaptive Mesh Refinement on Forests of Octrees". *SIAM Journal on Scientific Computing* 33, pp. 1103–1133, 2011. DOI: `10.1137/100791634`.

[23] Carsten Burstedde and Lucas C. Wilcox amd Tobin Isaac. *p4est: Parallel AMR on Forests of Octrees*. `https://www.p4est.org`. Accessed: 2024-12-10.

[24] P.R. Amestoy, I.S. Duff, and J.-Y. L'Excellent. "Multifrontal parallel distributed symmetric and unsymmetric solvers". *Computer Methods in Applied Mechanics and Engineering* 184, pp. 501–520, 2000. DOI: `https://doi.org/10.1016/S0045-7825(99)00242-X`.

[25] Carsten Burstedde and Lucas C. Wilcox amd Tobin Isaac. *MUMPS:MUltifrontal Massively Parallel sparse direct Solver*. `https://www.p4est.org`. Accessed: 2024-12-10.

[26] Akira Nishida. "Experience in Developing an Open Source Scalable Software Infrastructure in Japan". In: *Computational Science and Its Applications – ICCSA 2010*. Ed. by David Taniar, Osvaldo Gervasi, Beniamino Murgante, Eric Pardede, and Bernady O. Apduhan. Berlin, Heidelberg: Springer Berlin Heidelberg, 2010. Pp. 448–462.

[27] A. Nishida. *Lis: Library of Iterative Solvers for Linear Systems*. `https://www.ssisc.org/lis`. Accessed: 2024-12-10.

[28] John W. Eaton, David Bateman, Søren Hauberg, and Rik Wehbring. *GNU Octave version 9.2.0 manual: a high-level interactive language for numerical computations*. 2024.

References for Chapter 5

[1] Lin Li, Chuan Li, Subhra Sarkar, Jie Zhang, Shawn Witham, Zhe Zhang, Lin Wang, Nicholas Smith, Marharyta Petukh, and Emil Alexov. "DelPhi: a comprehensive suite for DelPhi software and associated resources". *BMC biophysics* 5, pp. 1–11, 2012.

[2] Y. C. Zhou, Michael Feig, and G. W. Wei. "Highly accurate biomolecular electrostatics in continuum dielectric environments". *Journal of Computational Chemistry* 29, pp. 87–97, 2008. DOI: `https://doi.org/10.1002/jcc.20769`.

[3] Duan Chen, Zhan Chen, Changjun Chen, Weihua Geng, and Guo-Wei Wei. "MIBPB: A software package for electrostatic analysis". *Journal of Computational Chemistry* 32, pp. 756–770, 2011. DOI: `https://doi.org/10.1002/jcc.21646`.

[4] Y.-K. Yu. "Electrostatics of charged dielectric spheres with application to biological systems. III. Rigorous ionic screening at the Debye-Hückel level". *Physical Review E* 102, p. 052404, 2020.

[5] O. I. Obolensky, T. P. Doerr, and Yi-Kuo Yu. "Rigorous treatment of pairwise and many-body electrostatic interactions among dielectric spheres at the Debye-Hückel level". *Eur. Phys. J. E* 44, p. 129, 2021.

[6] S. V. Siryk, A. Bendandi, A. Diaspro, and W. Rocchia. "Charged dielectric spheres interacting in electrolytic solution: a linearized Poisson-Boltzmann equation model". *J. Chem. Phys.* 155, p. 114114, 2021.

[7] S. Siryk and W. Rocchia. "Arbitrary-Shape Dielectric Particles Interacting in the Linearized Poisson-Boltzmann Framework: An Analytical Treatment". *J. Phys. Chem. B* 126, pp. 10400–10426, 2022.

[8] Y.-K. Yu. "Electrostatics of charged dielectric spheres with application to biological systems. II. A formalism bypassing Wigner rotation matrices". *Physical Review E* 100, p. 012401, 2019.

[9] José A Ferreira and Rolf D Grigorieff. "On the supraconvergence of elliptic finite difference schemes". *Applied numerical mathematics* 28, pp. 275–292, 1998.

[10] Pasquale Claudio Africa, Carlo de Falco, and Simona Perotto. "Scalable recovery-based adaptation on Cartesian quadtree meshes for advection-diffusion-reaction problems". *Advances in Computational Science and Engineering* 1, pp. 443–473, 2023. DOI: `10.3934/acse.2023018`.

[11] Yifan Song, Junjun Mao, and M. R. Gunner. "MCCE2: Improving protein pKa calculations with extensive side chain rotamer sampling". *Journal of Computational Chemistry* 30, pp. 2231–2247, 2009. DOI: `https://doi.org/10.1002/jcc.21222`.

[12] Robert C Harris, Alexander H Boschitsch, and Marcia O Fenley. “Influence of grid spacing in Poisson-Boltzmann equation binding energy estimation”. *Journal of chemical theory and computation* 9, pp. 3677–3685, 2013.

[13] Alexander H Boschitsch and Marcia O Fenley. “A fast and robust Poisson-Boltzmann solver based on adaptive Cartesian grids”. *Journal of chemical theory and computation* 7, pp. 1524–1540, 2011.

[14] Jun Wang, Chunhu Tan, Yu-Hong Tan, Qiang Lu, and Ray Luo. “Poisson-Boltzmann solvents in molecular dynamics simulations”. *Commun Comput Phys* 3, pp. 1010–1031, 2008.

[15] Nathan A Baker, David Sept, Simpson Joseph, Michael J Holst, and J Andrew McCammon. “Electrostatics of nanosystems: application to microtubules and the ribosome”. *Proceedings of the National Academy of Sciences* 98, pp. 10037–10041, 2001.

[16] Michał Bosy, Matthew W Scroggs, Timo Betcke, Erik Burman, and Christopher D Cooper. “Coupling finite and boundary element methods to solve the Poisson-Boltzmann equation for electrostatics in molecular solvation”. *Journal of Computational Chemistry* 45, pp. 787–797, 2024.

[17] Duc D Nguyen, Bao Wang, and Guo-Wei Wei. “Accurate, robust, and reliable calculations of Poisson-Boltzmann binding energies”. *Journal of computational chemistry* 38, pp. 941–948, 2017.

References for Chapter 7

[1] Enrico Fermi, P Pasta, Stanislaw Ulam, and Mary Tsingou. *Studies of the nonlinear problems*. Tech. rep. Los Alamos National Lab.(LANL), Los Alamos, NM (United States), 1955.

[2] Giovanni Gallavotti. *The Fermi-Pasta-Ulam problem: a status report*. Vol. 728. Springer, 2007.

[3] Stefano Lepri, ed. *Thermal Transport in Low Dimensions: From Statistical Physics to Nanoscale Heat Transfer (Lecture Notes in Physics)*. 1st ed. 2016. Springer, Apr. 2016.

[4] G Benettin and A Ponno. “Time-scales to equipartition in the Fermi–Pasta–Ulam problem: finite-size effects and thermodynamic limit”. *Journal of Statistical Physics* 144, pp. 793–812, 2011.

[5] Miguel Onorato, Lara Vozella, Davide Proment, and Yuri V Lvov. “Route to thermalization in the α-Fermi–Pasta–Ulam system”. *Proceedings of the National Academy of Sciences* 112, pp. 4208–4213, 2015.

[6] Yuri V Lvov and Miguel Onorato. “Double scaling in the relaxation time in the β-Fermi-Pasta-Ulam-Tsingou model”. *Physical review letters* 120, p. 144301, 2018.

[7] Zhen Wang, Weicheng Fu, Yong Zhang, and Hong Zhao. "Wave-turbulence Origin of the Instability of anderson Localization against many-body Interactions". *Physical Review Letters* 124, p. 186401, 2020.

[8] Chih-Wei Chang. "Non-diffusive Thermal Conduction in One-dimensional Materials." *AAPPS Bulletin* 28, 2018.

[9] I-Ling Chang, Chia-Shing Li, Guan-Shiung Wang, Chi-Lin Wu, and Chih-Wei Chang. "Does equilibrium or nonequilibrium molecular dynamics correctly simulate thermal transport properties of carbon nanotubes?" *Physical Review Materials* 4, p. 036001, 2020.

[10] Yi Zhong, Yong Zhang, Jiao Wang, and Hong Zhao. "Normal heat conduction in one-dimensional momentum conserving lattices with asymmetric interactions". *Physical Review E* 85, p. 060102, 2012.

[11] Shunda Chen, Yong Zhang, Jiao Wang, and Hong Zhao. "Key role of asymmetric interactions in low-dimensional heat transport". *Journal of Statistical Mechanics: Theory and Experiment* 2016, p. 033205, 2016.

[12] Stefano Lepri, Roberto Livi, and Antonio Politi. "Too close to integrable: Crossover from normal to anomalous heat diffusion". *Physical Review Letters* 125, p. 040604, 2020.

[13] S R De Groot and P Mazur. *Non-Equilibrium Thermodynamics*. Dover Publications, New York, 1984.

[14] Pablo I Hurtado. "Breakdown of hydrodynamics in a simple one-dimensional fluid". *Physical review letters* 96, p. 010601, 2006.

[15] C Giberti and L Rondoni. "Anomalies and absence of local equilibrium, and universality, in one-dimensional particles systems". *Physical Review E* 83, p. 041115, 2011.

[16] Claudio Giberti, Lamberto Rondoni, and Cecilia Vernia. "Temperature and correlations in 1-dimensional systems". *The European Physical Journal Special Topics* 228, pp. 129–142, 2019.

[17] Claudio Giberti, Lamberto Rondoni, and Cecilia Vernia. "O (N) fluctuations and lattice distortions in 1-dimensional systems". *Frontiers in Physics* 7, p. 180, 2019.

[18] L.D. Landau and E.M. Lifshitz. *Statistical Physics, part 1*. Pergamon, New York, 1980.

[19] S Chibbaro, L Rondoni, and A Vulpiani. *Reductionism, Emergence and Levels of Reality, The Importance of Being Borderline*. Springer-Verlag, 2014.

[20] Dilip Kondepudi and Ilya Prigogine. *Modern thermodynamics: from heat engines to dissipative structures*. John Wiley & Sons, 2014.

[21] H Spohn. *Large Scale Dynamics of Interacting Particles*. Springer-Verlag, 1991.

[22] J. Bellissard. "Coherent and dissipative transport in aperiodic solids: An overview". *Dynamics of Dissipation*, pp. 413–485, 2002.

[23] H J Kreuzer. *Nonequilibrium Thermodynamics and Its Statistical Foundations*. Claredon Press, 1981.

[24] M Falcioni, L Palatella, S Pigolotti, L Rondoni, and A Vulpiani. "Initial growth of Boltzmann entropy and chaos in a large assembly of weakly interacting systems". *Physica a-Statistical Mechanics and Its Applications* 385, pp. 170–184, 2007.

[25] L Rondoni and S Pigolotti. "On Γ-and μ-space descriptions: Gibbs and Boltzmann entropies of symplectic coupled maps". *Physica Scripta* 86, p. 058513, 2012.

[26] Giovanni Dematteis, Lamberto Rondoni, Davide Proment, Francesco De Vita, and Miguel Onorato. "Coexistence of Ballistic and Fourier Regimes in the β Fermi-Pasta-Ulam-Tsingou Lattice". *Physical Review Letters* 125, p. 024101, 2020.

[27] Bambi Hu, Baowen Li, and Hong Zhao. "Heat conduction in one-dimensional chains". *Physical Review E* 57, p. 2992, 1998.

[28] Stefano Lepri, Roberto Livi, and Antonio Politi. "Thermal conduction in classical low-dimensional lattices". *Physics reports* 377, pp. 1–80, 2003.

[29] Paolo De Gregorio, Lamberto Rondoni, Michele Bonaldi, and Livia Conti. "One-dimensional models and thermomechanical properties of solids". *Physical Review B* 84, p. 224103, 2011.

[30] Jianjun Jiang and Hong Zhao. "Modulating thermal conduction by the axial strain". *Journal of Statistical Mechanics: Theory and Experiment* 2016, p. 093208, 2016.

[31] Gianmaria Falasco, Fulvio Baldovin, Klaus Kroy, and Marco Baiesi. "Mesoscopic virial equation for nonequilibrium statistical mechanics". *New Journal of Physics* 18, p. 093043, 2016.

[32] Carlos Mejía-Monasterio, Antonio Politi, and Lamberto Rondoni. "Heat flux in one-dimensional systems". *Physical Review E* 100, p. 032139, 2019.

[33] Rudolf Clausius. "XVI. On a mechanical theorem applicable to heat". *The London, Edinburgh, and Dublin Philosophical Magazine and Journal of Science* 40, pp. 122–127, 1870.

[34] Suman G Das, Abhishek Dhar, and Onuttom Narayan. "Heat conduction in the α- β Fermi–Pasta–Ulam chain". *Journal of Statistical Physics* 154, pp. 204–213, 2014.

[35] Asaf Miron, Julien Cividini, Anupam Kundu, and David Mukamel. "Derivation of fluctuating hydrodynamics and crossover from diffusive to anomalous transport in a hard-particle gas". *Physical Review E* 99, p. 012124, 2019.

[36] Z Rieder, JL Lebowitz, and E Lieb. "Properties of a harmonic crystal in a stationary nonequilibrium state". *Journal of Mathematical Physics* 8, pp. 1073–1078, 1967.

[37] Jürgen Vollmer, Lamberto Rondoni, Muhammad Tayyab, Claudio Giberti, and Carlos Mejía-Monasterio. "Displacement autocorrelation functions for strong anomalous diffusion: a scaling form, universal behavior, and corrections to scaling". *Physical Review Research* 3, p. 013067, 2021.

[38] Bruce N Miller and Peter M Larson. "Heat flow in a linear harmonic chain: An information-theoretic approach to the nonequilibrium stationary state". *Physical Review A* 20, p. 1717, 1979.

[39] L Conti, P De Gregorio, G Karapetyan, C Lazzaro, M Pegoraro, M Bonaldi, and L Rondoni. "Effects of breaking vibrational energy equipartition on measurements of temperature in macroscopic oscillators subject to heat flux". *J. Stat. Mech.*, 2013.